Prediction of Deep Bright Spots via Gassmann Fluid Substitution and Seismic Amplitude Interpretation in the Vermilion Area, Northern Gulf of Mexico

---

A Thesis

Presented to the

Faculty of the Department of Earth and Atmospheric Sciences

University of Houston

In Partial Fulfillment

of the Requirements for the Degree

Master of Science

By

Halil Emre Celep

May 2012

Prediction of Deep Bright Spots via Gassmann Fluid Substitution and Seismic Amplitude Interpretation in the Vermilion Area, Northern Gulf of Mexico

---

Halil Emre Celep

APPROVED:

Dr. Christopher Liner (Chairman)

Dr. Robert Stewart (Member)

Dr. Cengiz Esmersoy (Member)

Dean, College of Natural Sciences and Mathematics

Acknowledgements

I would like to thank many special and kind people who patiently supported me during the writing of this thesis. In particular, I heartily thank my advisor Dr. Chris Liner, for his invaluable guidance, patience, and encouragement since the initiation of my graduate studies at the University of Houston. Without his precious efforts, the writing of this thesis would not have been accomplished.

I would like to express my sincere gratitude to the rest of my committee members, Dr. Robert Stewart and Dr. Cengiz Esmersoy, whose illuminating comments enabled me to develop a better understanding of the subject during my studies.

I deeply thank my dear beloved parents and sister for their endless love and forbearence throughout the course of this study. Without their generous support, I could not have managed to complete this project.

Last but not least, I offer my special thanks to my dear friends and other valuable people who contributed to the completion of this project.

Prediction of Deep Bright Spots via Gassmann Fluid Substitution and Seismic Amplitude Interpretation in the Vermilion Area, Northern Gulf of Mexico

---

An Abstract of a Thesis
Presented to the
Faculty of the Department of Earth and Atmospheric Sciences
University of Houston

In Partial Fulfillment
of the Requirements for the Degree
Master of Science

By

Halil Emre Celep

May 2012

Abstract

The objective of this study is to investigate the deep bright spots observed in the Vermilion area, northern Gulf of Mexico, and assess whether they represent gas sand reservoirs. The study was carried out by Gassmann fluid substitution, seismic amplitude interpretation, and Reuss bound examinations of five study areas in the region. The Davy Jones gas discovery of the McMoRan Company at about 8700 m in South Marsh Island Block 230 (close to the Vermilion area) provided both the motivation and initial reservoir parameters for this study. Tertiary Wilcox sands are the primary reservoir targets of the study. The reservoir conditions of Davy Jones were simulated by coding Gassmann's equations and Batzle's relations in Matlab to study fluid effects and bright spot signatures. Based on reservoir response, the study areas were compared by fluid substitution analysis and seismic amplitude interpretation. Examination included reservoir response for brine and gas saturated velocities, reflection coefficients, and elastic parameters. Furthermore, Reuss bound studies of the areas were originated from brine-and gas-saturated P-wave moduli bounds of Davy Jones, and they increased the confidence of the reservoir response associated with each study area. Adjusted pore pressures, formation temperatures, and stiffness parameters were found to play a key role in characterizations of the areas. The study showed that three of the study areas (N1, N2, and N3) have probable gas bright spot responses, whereas two regions (N4 and N5) show amplitude anomalies inconsistent with gas bright spots.

Table of Contents

List of Figures

List of Tables

Chapter 1. Introduction

Rock physics represents a robust connection between seismic data, hydrocarbons, and reservoir conditions. In particular, Gassmann fluid substitution is considered to be an effective tool to estimate direct hydrocarbon indicators (DHI), since the nature of Gassmann's equations establish relationships between properties of the reservoir frame and pore fluid by predicting changes in seismic velocity and the bulk modulus of reservoir rocks (Han and Batzle, 2004).

Gassmann fluid substitution has thus been commonly used in estimating reservoir properties of rocks as well as in observing the varying characteristics of saturating fluids under specific physical conditions. These physical factors mainly involve the environmental and compositional properties of a reservoir in terms of fluid substitution considerations. Specifically, environmental conditions might be attributed to effects of pore pressures and formation temperatures, whereas compositional factors are related to reservoir frame properties primarily through porosity and stiffness parameters. Once these parameters are properly approximated, any reservoir can be studied for possible fluid substitution effects within the applicability limits of Gassmann's method. Gassmann's approach has been widely utilized in a broad range of environments and purposes including 4D reservoir monitoring, laboratory estimations of rock and fluid properties, and bright spot analysis of reservoir rocks.

Davy Jones is a major hydrocarbon gas discovery at 8,696 meters (below the shelf floor) in the South Marsh Island area, northern Gulf of Mexico. In this study, we investigate whether reported conditions and rock properties at Davy Jones are consistent

with bright spot characteristics indicated by Gassmann fluid substitution analysis. Once adequately characterized by simulating reservoir condition and fluid substitution, many regions demonstrating similar bright spot indications can be examined with this method. Thus, the intention of this study has been to investigate the feasibility of amplitude bright spots in the deep Vermilion area, northern Gulf of Mexico (Figure 1).

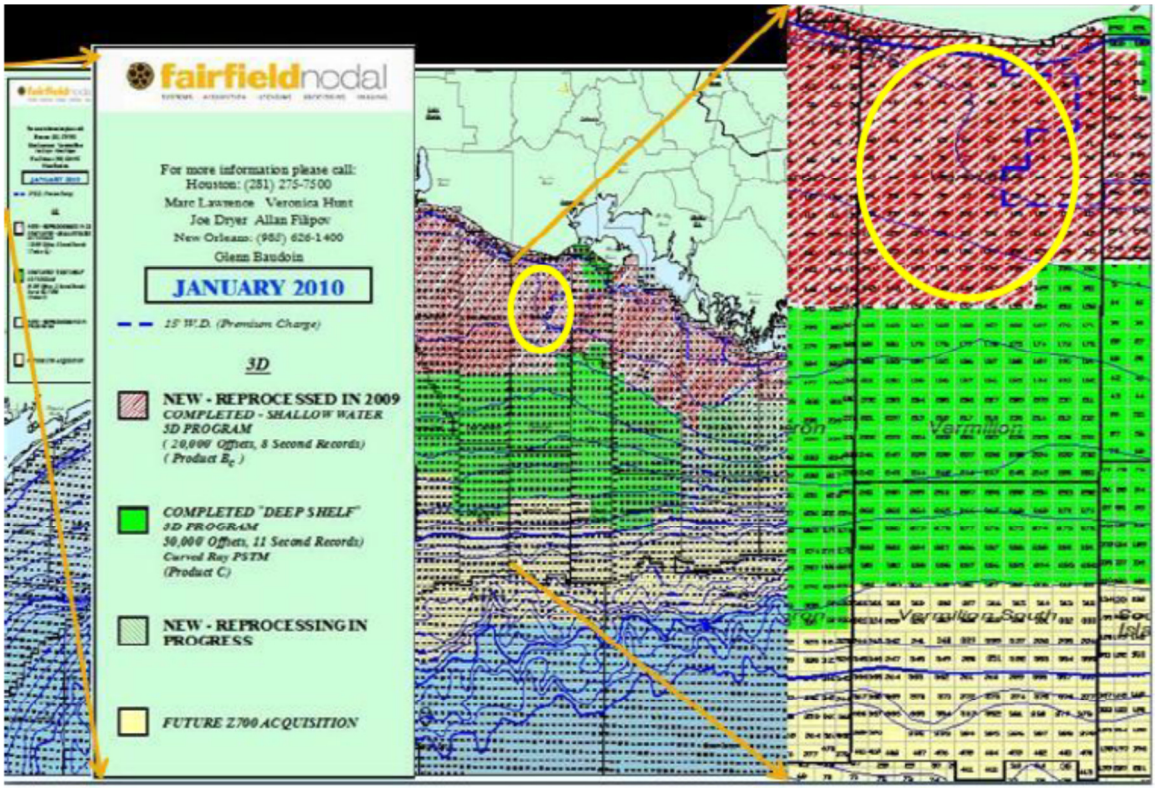

Figure 1. Northern Gulf of Mexico seismic coverage and bathymetry map. Yellow circle indicates approximate position of 3-D seismic data used in this study. (Fairfield Nodal, 2011)

Other Vermilion deep targets adjacent to Davy Jones may exhibit similar bright spot responses based on their corresponding geological histories. Five study areas with distinct negative amplitude anomalies were identified through seismic amplitude interpretation. Then, fluid substitution signatures of the areas were compared with their seismic responses, based on Davy Jones reservoir parameters to decide whether those amplitude anomalies were consistent with gas bright spot characteristics.

1.1 Geological Setting

1.1.1 Regional Tectonics

The Paleocene-Eocene Wilcox fault system is a distinctive growth fault system within the northern Gulf of Mexico (Diegel et al., 1995). This fault system shows extensive changes depending on its position in the shelf-slope locations of southeastern Texas and southern Louisiana. Landward sections of the fault system can easily be differentiated from its slope extension, since it steeply dips and reaches great depths in the slope region as a result of the confined depositional geometry of the slope. In contrast, the Wilcox fault system is recognized with its shallower position and steady progression along more landward regions.

The shallower coastal section of the fault system displays more elaborate features compared with its basinward counterpart which is underlain by the Jurassic Louann salts (Peel et al., 1995). Cretaceous deposition is nearly absent throughout landward positions causing the fault system to intersect with Eocene depositional features (Upper Wilcox

stage) while the basinward section travels downward along a thicker Cretaceous depositional column toward the Jurassic Louann salts. Furthermore, thick salt walls accompany the massive Cretaceous deposition and exhibit downward movements along slope regions by generating a space for related Cretaceous deposition (Rowan et al., 1999; Radovich et al., 2007).

On the other hand, thick salt walls are replaced by salt withdrawals which evacuate landward sections. All these salt movements contributed to the formation and extension of the Wilcox growth fault system. In general, the Wilcox growth fault system of southern Texas shows characteristics similar to its southern Louisiana intersect in terms of fault orientations from onshore to offshore. One of the well-known differences is that the landward regions in the vicinity of southern Texas demonstrates more intensive salt evacuation compared with those in southern Louisiana. In addition, fault shapes are recognized as being varied on regional perspectives between the southern Texas and southern Louisiana regions.

A general structural map of the northern Gulf of Mexico is given in Figure 2. The Wilcox fault system of the southern Texas (Figure 3) has linear growth faults, whereas the Wilcox fault system of southern Louisiana demonstrates arch-shaped growth faults. This major discrepancy in the fault shapes is considered to have been formed by varying depositional processes and environments of southern Texas and southern Louisiana. Particularly, strandplain and barrier island depositional processes dominate the Texas coastal area, while the Louisiana shelf is controlled by delta progradation and alluvial deposition processes.

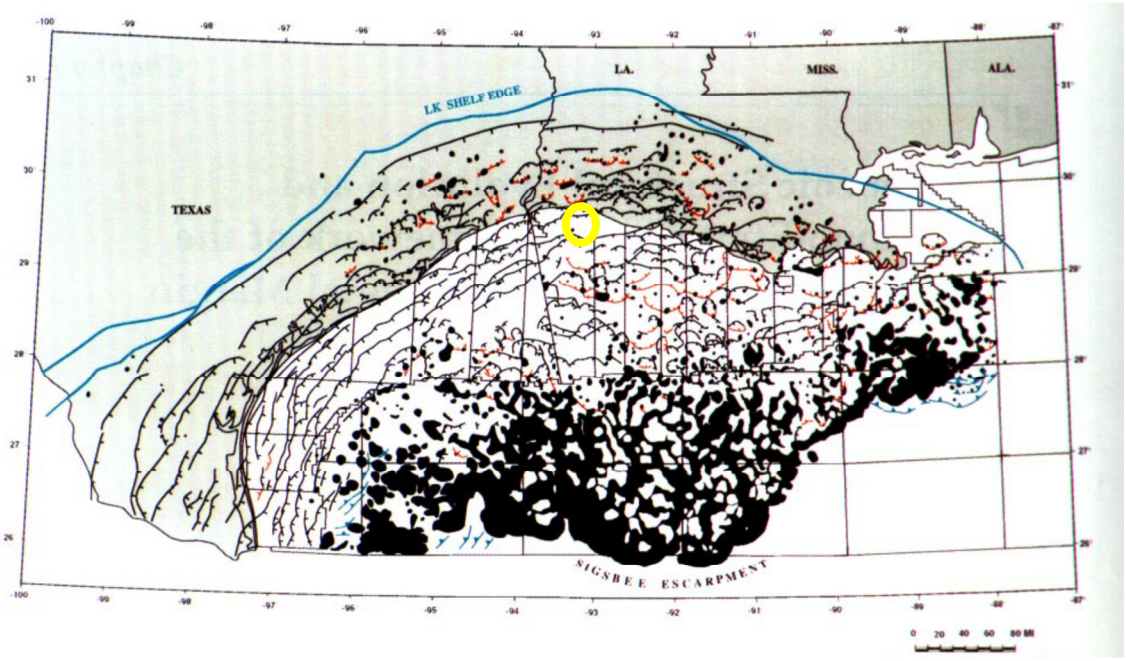

Figure 2. Structural summary map of the northern Gulf of Mexico Basin. Black areas are shallow salt bodies. Tick marks are on the downthrown side of major growth faults: black = seaward dipping; red = landward dipping (counter-regional); blue = thrust faults, yellow circle shows the position of 3-D seismic data used in the study (Diegel et al., 1995).

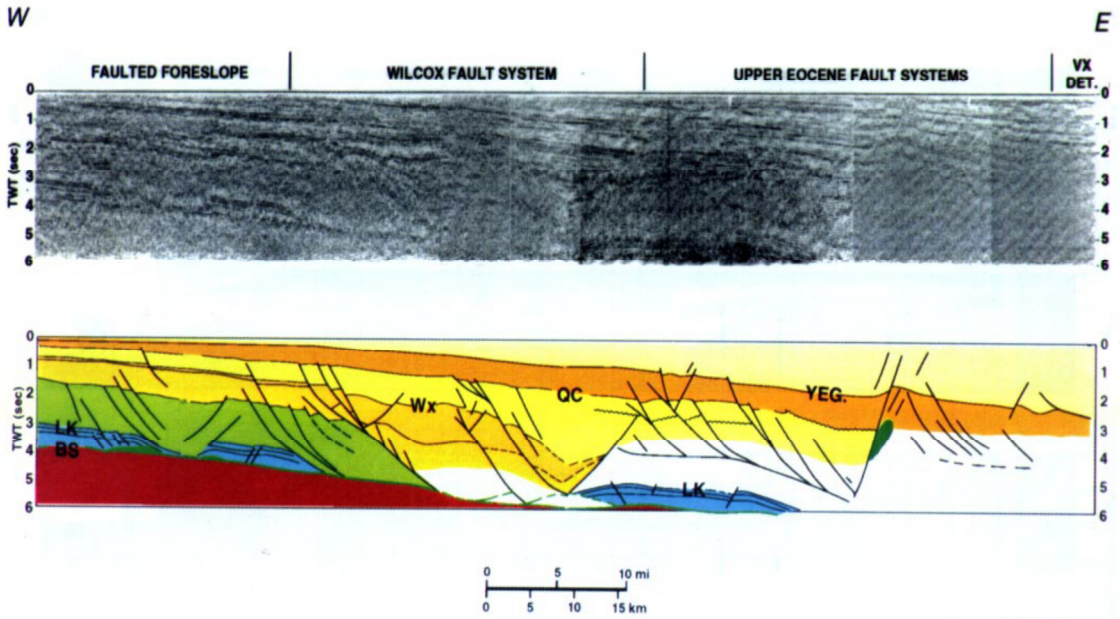

Figure 3. Uninterpreted regional seismic profile (top) and interpreted drawing (bottom) across the Wilcox and upper Eocene fault systems, onshore southern Texas. YEG = Eocene Yegua, QC = Eocene Queen City, Wx = Eocene Wilcox, LK = Lower Cretaceous, BS = base of Jurassic Louann salt (Diegel et al., 1995).

1.1.2 Depositional Environment and Stratigraphy

The Cenozoic sediment fill of the northern Gulf of Mexico includes two major periods, starting in the Paleogene and continuing throughout the Neogene. The objective of this study is mostly to delineate Paleocene and Eocene depositional characteristics. The Wilcox sediment fill is the focus of depositional aspects for the study area. From the northwest to northeastern Gulf of Mexico, eight distinct depocenters are responsible for Cenozoic sediment deposition. These are the Norma, Rio Grande, Carrizo, Corsair, Houston, Red River, Central Mississippi, and East Mississippi depocenters (Galloway et

al., 2000). The Houston, Red River, Central Mississippi, and East Mississippi sources primarily fed and formed the Cenozoic sediment fill of the study area. The main control mechanism which triggers sediment supply via these sources is tectonic uplift. For instance, the Laramide uplift provided the bulk of sediments from the Paleocene to middle Eocene by pushing sediments from the northwest to eastward, while the Houston delta was the source for the north-central Gulf of Mexico sediments during the Eocene.

Lower Wilcox deposition (Figures 4, 6, and 7) occurred in the northwestern and north-central Gulf of Mexico during the late Paleocene. The lower Wilcox sediment fill of the Gulf marks the relative positions of the shelf and the slope at the time of deposition. Massive sediment input enlarged the shelf in the onshore direction while offshore sediments formed reefs on the steepened slope region as a result of immediate sea-level rises. Progradation of the lower Wilcox sediments further basinward can be characterized with offlaping sediments on the steep slope. The fluvial-dominated Houston delta and three small wave-dominated deltas combined together and created a wave-dominated shore zone system from the Burgos Basin to south Texas. This system effectively fed the area during the late Paleocene, lower Wilcox deposition.

On the other hand, the middle Wilcox deposition shows remarkably little deposition through the latest Paleocene to the earliest Eocene in comparison to the lower and upper Wilcox deposition. A transgressive sequence confines the middle Wilcox deposition. The older transgression lag which underlies the Wilcox deposits, and consists of the central Gulf of Mexico's big shale known as the Yoakum shale; it is the younger transgressive lag bounding the upper section of middle Wilcox deposition. The fluvial-

dominated Calvert and LaSalle deltas supplied most of the sediments and shaped the middle Wilcox deposition throughout the north-central Gulf of Mexico. Both transgression surfaces bounding the middle Wilcox sediments were incised. The Yoakum shale and upper Wilcox sediments filled the younger incised valleys, while the older incised valleys of the bottom transgressive surface were mainly deposited by middle Wilcox sediments.

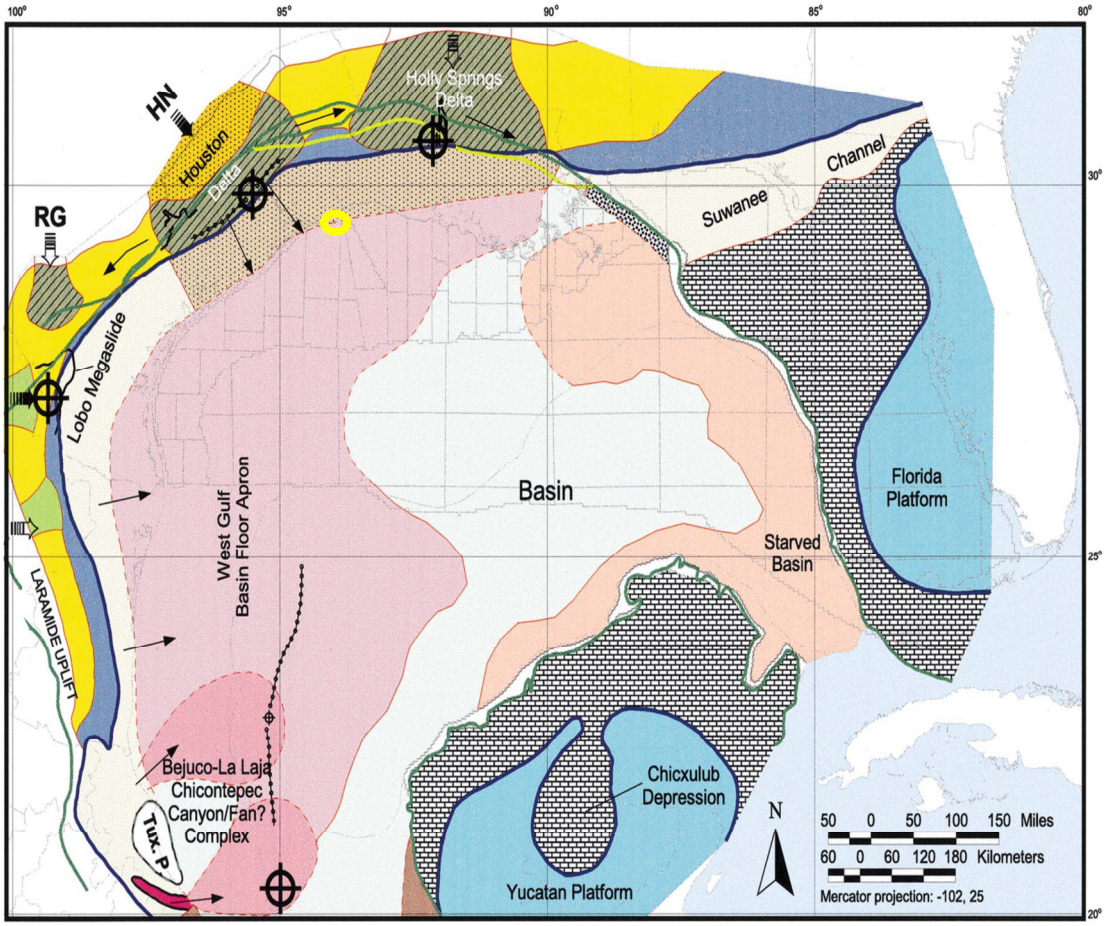

Figure 4. Paleogeography of the Lower Wilcox (LW-B, 61–56.4 Ma). See Figures 6 and 7 for explanations of symbols and abbreviations. Tux. P._ Tuxpan plateau, yellow circle shows the position of 3-D seismic data used in the study (Galloway et al., 2000).

Lastly, the upper Wilcox deposition (Figures 5, 6, and 7) dominated the north-central Gulf of Mexico during the early Eocene. The Rio Grande and Houston deltas formed the shelf deposition by spreading fluvial-Carrizo sandstone. Along the shelf margin, this fluvial deposition combined with the wave-dominated Rosita delta and they together input more sediment and expanded the upper Wilcox deposition. Later, the wave-dominated Mississippi delta contributed to the sediment supply of the other deltas by further spreading upper Wilcox deposition in the north-central Gulf of Mexico. However, this expansion of the upper Wilcox sediment fill was interrupted by the Eocene growth fault system which is also known as "the Wilcox growth fault system." Therefore, the early Eocene upper Wilcox deposition was confined within the shelf margin system of the middle Wilcox deposition as an inevitable result of the growth fault orientation from shelf-to-slope across the north-central Gulf of Mexico (Galloway et al., 2000).

The composition of the Wilcox sandstones is primarily lithic arkoses and feldspathic litharenites (Dutton and Loucks, 2010). Even though sorting and packing of sand grains may vary significantly, the composition of these sands does not change explicitly throughout Wilcox depositions. However, their composition is greatly affected by their locations in a stratigraphic hierarchy. For instance, lowstand Wilcox sands filling submarine canyons are found to have more rock fragments than the Wilcox sands deposited during highstands in the northern Gulf of Mexico.

The porosity and permeability relations of the Wilcox sands are mostly controlled by several pore types, which change with temperature, burial depth, chemical activities and different compaction factors. It is observed by Dutton that primary pores are mainly

preserved in shallower burial depths at relatively lower temperatures while primary pores are replaced by secondary pores and micropores at larger burial depths and temperatures.

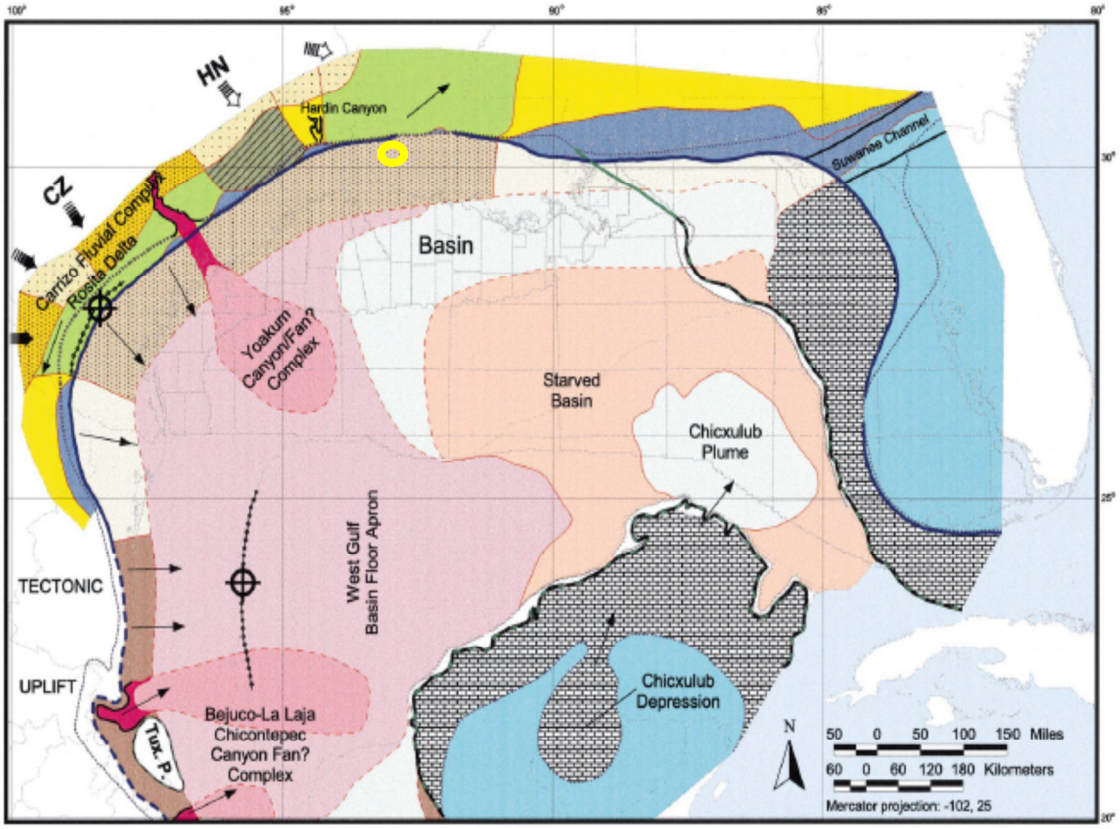

Figure 5. Paleogeography of the Upper Wilcox (UW-C, 48.5–54.5 Ma). See Figures 6 and 7 for explanations of symbols and abbreviations (Galloway et al., 2000).

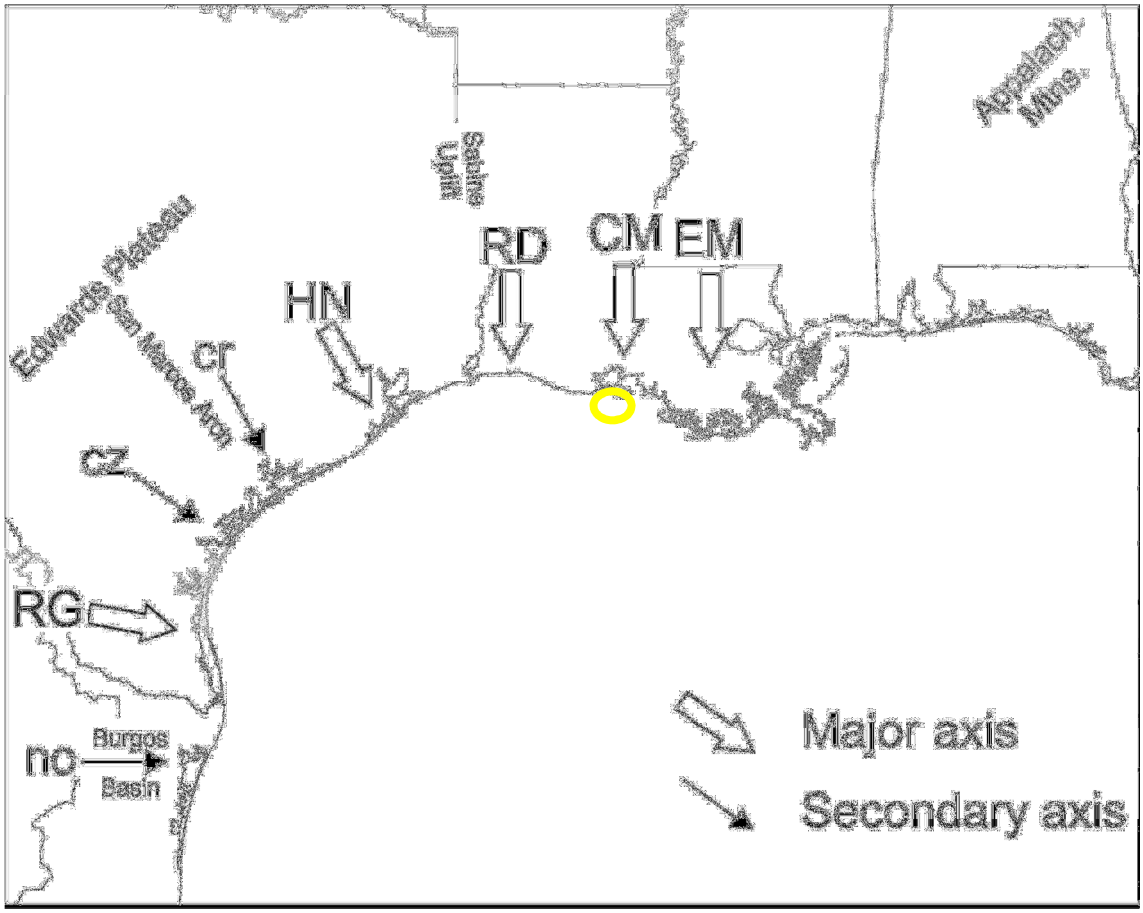

Figure 6. Basin-margin structural features and principal (upper case) and secondary (lower case) Cenozoic sediment dispersal axes of the Gulf of Mexico basin: no_ Norias; RG_ Rio Grande; cz _ Carrizo; cr_Corsair; HN_Houston; RD_Red River; CM_Central Mississippi; EM _ East Mississippi (Galloway et al., 2000).

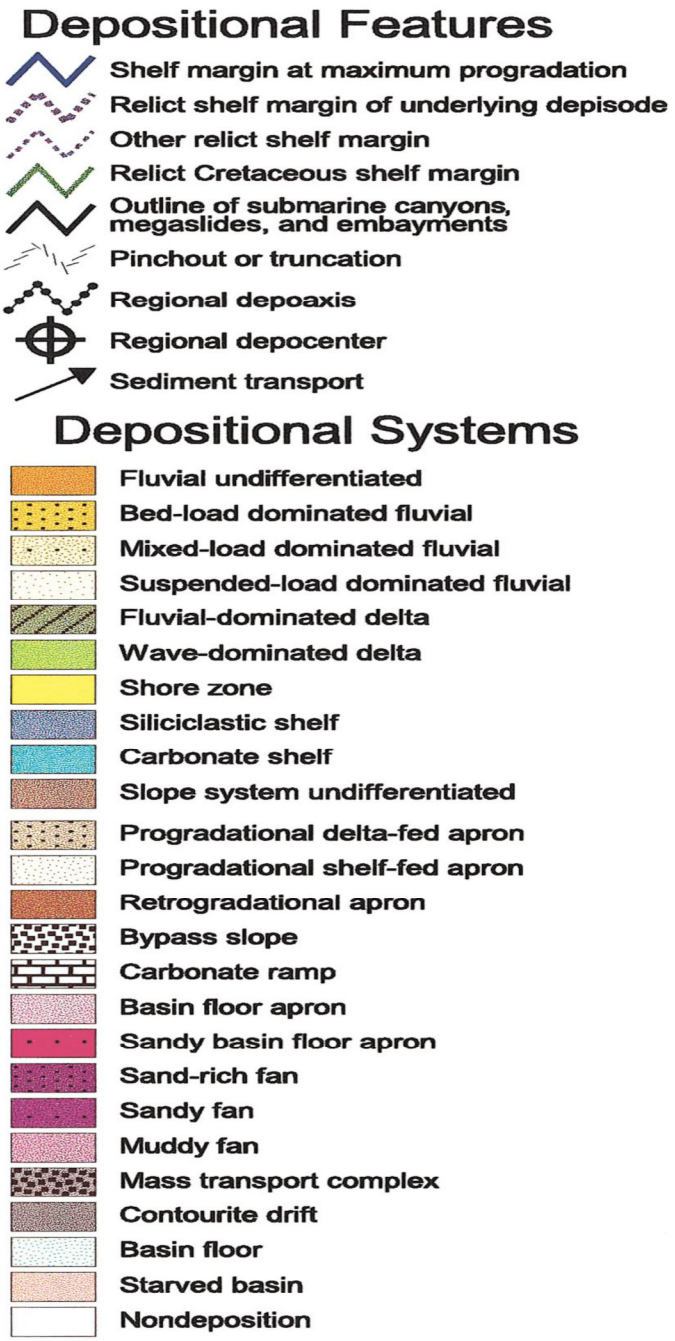

Figure 7. Explanation of symbols for paleogeographic maps (Figures 4, 5). Maps show depositional systems, sediment dispersalaxes, generalized depocenters, and selected depositional and erosional features (Galloway et al., 2000).

The primary pores of the Wilcox sands which are responsible for most of the porosity and permeability are those observed to be maintained up to around 132 ^{o}C. Beyond this temperature and with increasing depth, primary pores are lost and secondary pores and micropores constitute the bulk of their porosity. The effect of porosity reduction seems to be lowered at around 230 ^{o}C and at greater burial depths beyond 6000 meters. Therefore, Wilcox sands deposited deeper than 6000 m may also represent some porosity rates above 10 % which are suitable for hydrocarbon accumulation in the northern Gulf of Mexico.

Since the 1930's, the Wilcox group of sands has been a productive petroleum depositional system. The Wilcox sands consist of fluvial, shallow marine, and deltaic sandstone and are mainly gas-productive in Louisiana and south-eastern Texas. Furthermore, they trap oil offshore mainly by deep-water turbidites representing leave channel systems, amalgamated, and sheet-like sands. The upper Wilcox group can be characterized by mud-dominated channel leave and amalgamated channels from slope to basin floor. On the other hand, the lower Wilcox section is formed by sheet-like sands and amalgamated sands covering a large basin floor like a submarine fan system (Meyer, et al., 2005).

In terms of reservoir quality, sorting, lateral continuity, and porosity, offshore Wilcox sands tend to be higher quality sands compared with the onshore Wilcox group. Since the onshore Wilcox group contains a significant amount of silt, it leads to the degradation of reservoir properties of onshore Wilcox sands.

1.2 Purpose of Study

The purpose of this study is to investigate the occurrence of bright spots as possible deep reservoir targets in the shallow-water Vermilion area, in the northern Gulf of Mexico, utilizing both Gassmann fluid substitution and seismic amplitude interpretation. Seismic data provided by Fairfield Nodal is pre-stack time migrated (PSTM) and covers the shallow water Vermilion area. Only one well is available over the area with a total depth of 5,014 m. Wilcox sands below 8,321 m are potential reservoir candidates that may exhibit gas bright spots. The primary motivation for this study comes from a giant gas discovery by McMoRan's "Davy Jones Prospect"; it is a four-way anticline closure in the Wilcox sands at about 8,573 to 8,614 m and in 6 m of water, within the South Marsh Island Block 230 and located at 16 km offshore Louisiana (Figure 8a).

According to preliminary reports, at this location there is 41 m of net gas pay with 20% porosity and 10-20 ohm resistivity in extreme temperature and pressure conditions. Bottom-hole temperatures and pressures reach 440 degrees Fahrenheit and 27,000 pounds per square inch (psi) respectively (The American Oil and Gas Reporter, 2010). What makes this discovery so crucial is that it proves the deep gas productivity of the shelf section in the northern Gulf of Mexico by illuminating an undefined Wilcox shelf trend (Figure 8b). Therefore, it establishes a bridge between the onshore and deep water Wilcox oil and gas reservoir systems. Furthermore, the presence of such a large gas accumulation within the shallow shelf region brings attention to undiscovered reserves in the northern Gulf of Mexico.

The Vermilion shelf area adjacent to South Marsh Island is thought to have a similar geological history and properties similar to those of South Marsh Island in terms of both depositional and tectonic evolution. One of the primary intentions of this study is to observe similar Wilcox shelf trends in the study areas and to anticipate the presence of any bright spot anomalies based on distinctive seismic amplitude changes. For these purposes, five different study areas were examined in the Vermilion, 3-D seismic data set via seismic time and horizon amplitude interpretations. Each study area represented a strong negative amplitude anomaly, starting with moderate negative seismic amplitudes at the bottom and growing into robust negative amplitudes at the top of the reservoir.

The main consideration for choosing these particular amplitude signatures was to discriminate between brine-saturated and gas-saturated sand reservoirs in each study area. It was assumed that brine-saturated sands are represented with moderate negative amplitudes and that gas-saturated sands are related to stronger negative amplitudes in each reservoir feature. So, distinctive seismic amplitude signatures made it possible to quantify the reflection coefficient ratios of these reservoir features. Therefore, each study area was able to be seismically modeled by determining reflection coefficients for two distinct saturation conditions. Furthermore, Gassmann's fluid substitution was able to be used to simulate reflection coefficients. Combinations of seismically observed and Gassmann synthetic reflection coefficients could then be compared, and those results were used to determine whether bright spots associated with each study area were consistent with Gassmann predictions.

a)

b)

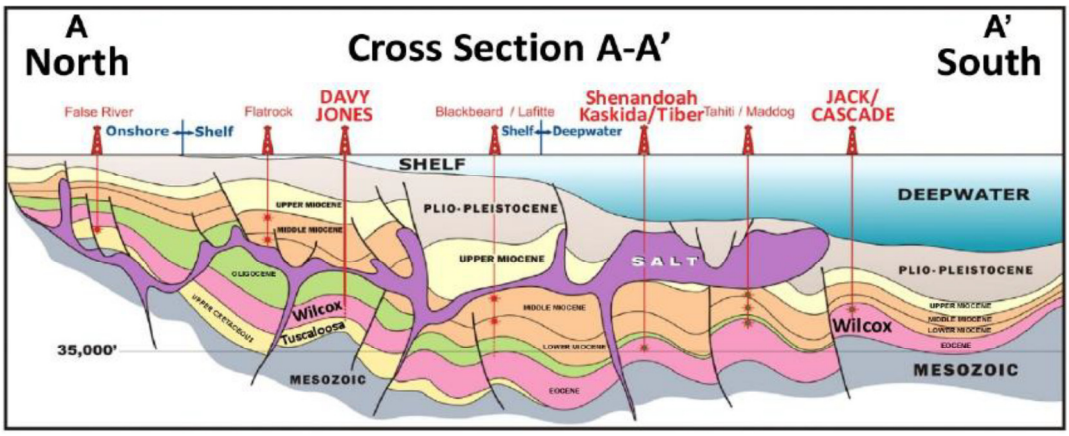

Figure 8. (a) Location of Davy Jones Discovery (Fairfield Nodal, 2011). (b) A geologic model section from north to south GoM (The American Oil and Gas Reporter, 2010).

Chapter 2. Methodology

2.1 Bright Spots and Gassmann Fluid Substitution

Rock physics-related interpretation of seismic data gives rise to a fluid substitution issue which needs to be analyzed closely in order to predict reservoir conditions and to evaluate direct hydrocarbon indicators (DHI), such as amplitude variation with offset (AVO), 4-D reservoir monitoring, and amplitude-related bright spots (Mavko et. al, 1995, Han and Batzle, 2004).

Gassmann's equations are used as a tool to estimate seismic reservoir properties and study fluid substitution phenomena, depending upon different fluid effects on rock frames. These equations establish a physical basis between the properties of porous rock frames and pore fluids to estimate changes in the seismic velocity, density, and bulk modulus of saturated rocks (Mavko et. al, 1995, Han and Batzle, 2004).

Amplitude bright spots are clearly noticed when brine below and gas or dissolved oil above are in conjunction with each other in a reservoir-seal formation. In other words, they are visible if the impedance of brine sand is smaller than the encasing lithology (generally a shale-based seal or a condensed section for GoM) and gas sand above the brine has further low impedance. Hence, brine sand has larger amplitude causing a noticeable seismic signature between the top and bottom of gas sand represented by a peak-over-through reflection called a zero polarity bright spot (Figure 9).

Once the gas sand has sufficient thickness to resolve top and base as separate reflectors, a flat-spot fluid contact occurs. This is generally represented by a peak

indicating impedance increase. A flat spot occurring in such conditions may be considered a direct hydrocarbon indicator (Brown, 1999). These types of amplitude and impedance changes in a reservoir can be characterized and determined seismically in terms of brine and gas fluid effects on the seismic velocity, density, and particularly on the bulk modulus of rocks.

Gassmann fluid substitution has many applications in determining various fluid, rock and seismic properties of reservoirs and laboratory samples. This study aims to model feasibility of deep reservoir gas bright spots by scrutinizing brine and gas effects on bulk modulus, density, and velocity. The procedure behind this type of analysis requires some assumptions to be made. First, we assume that the reservoir rock is homogenous, isotropic, monomineralic, and elastic throughout the reservoir. Second we assume the reservoir is a closed system and there is neither pore fluid movement nor chemical reaction between rock frame and fluids. The third assumption is that pore fluid only causes change on bulk modulus; shear modulus is not changed by fluid substitution. Pore spaces are thought to be sufficiently connected and show pressure equilibrium throughout the medium. This emphasizes the fact that Gassmann is a low-frequency theory (Han and Batzle, 2004).

Gassmann fluid substitution requires accurate estimation of pore pressure, temperature, and frame composition. The empirical relationships of Batzle and Wang (1992) give pore fluid properties as a function of pressure, temperature, and composition for use in Gassmann fluid substitution.

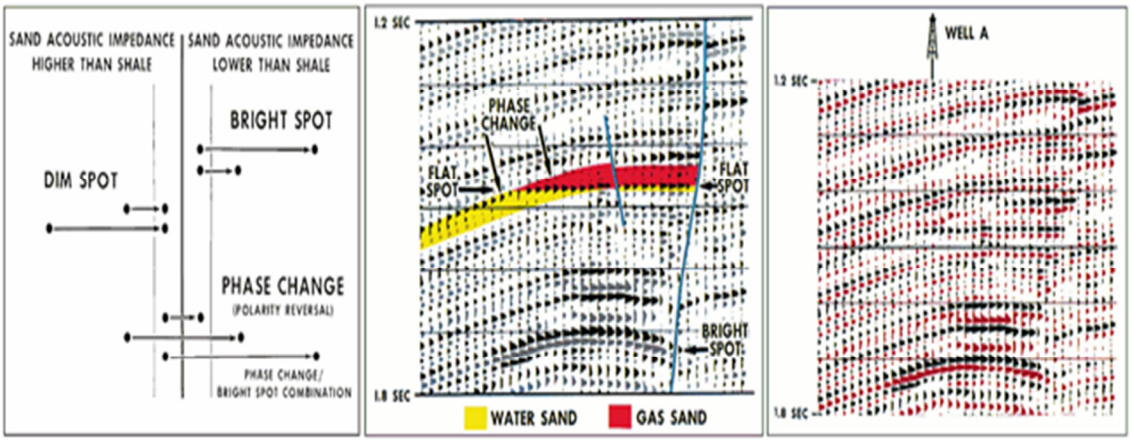

Figure 9. Bright and Flat Spots (Brown, 1999).

These calculations involve estimation of the densities, velocities, and bulk modulus of various types of fluids. Computing oil properties under reservoir conditions is not one of the objectives of this study due to the fact that bright spots occur between brine and gas.

The application of Gassmann fluid substitution and the empirical relationships of Batzle and Wang together follow a systematic procedure. The brine and gas fluid density, velocity, and bulk modulus are calculated first, using formation pore pressure, temperature, mineral density, porosity, salinity, formation depth, and gas molar constant values. Then, saturated P-wave modulus, densities, and velocities for brine and gas are computed using Gassmann's relation. Since this study lacks well data, computing S-wave velocities adequately is not possible. Therefore, P-wave modulus is used to compute saturated P-wave velocities in the absence of S-wave velocity information. However, P-

wave velocities are converted to S-wave velocities by using the following relation of Castagna (1985):

$$V_p = 1.16V_s + 1.36, \quad (1)$$

where Vp and Vs are P and S seismic velocities for brine-saturated clastic silicate rocks in km/s.

The aim of this conversion is to be able to compute AVO responses of each study area after fluid substitution. Gassmann's relation estimates the effective bulk modulus change caused by a bulk volume deformation of pores in a rock frame. This bulk volume change occurs when a seismic wave passes through pores of a rock frame. The passing seismic wave results in a pressure increment on the pore fluid and this stiffens the rock frame by causing bulk volume changes and more resistant bulk modulus of the rock frame. Dry (K_{dry}) and saturated (K_{sat}) effective bulk modulus of rock frames are related to each other through the following:

$$\frac{K_{sat}}{K_0 - K_{sat}} = \frac{K_{dry}}{K_0 - K_{dry}} + \frac{K_f}{\varphi(K_0 - K_f)}, \quad (2)$$

where K_0 is the mineral bulk modulus and K_f is the fluid bulk modulus in Mpa, while φ represents the fractional porosity. Since S-wave velocity is unknown, the bulk modulus K is replaced with the P-wave modulus M . This form of the fluid substitution equation allows an interpreter to determine elastic properties of saturated rocks based on P-wave modulus instead of bulk modulus. This relation can be expressed as

$$\frac{M_{sat}}{M_0 - M_{sat}} = \frac{M_{dry}}{M_0 - M_{dry}} + \frac{M_f}{\varphi(M_0 - M_f)}. \quad (3)$$

We characterized the fluid substitution effects of the Davy Jones reservoir and five study areas from Vermilion using this relation. However, the computation of P-wave moduli for each study area relied upon two different approaches. One method was to directly estimate dry rock modulus from the known mineral bulk and the shear modulus of quartz. Stiffness parameters which were used in this calculation are porosity dependent and given by Wang (2001). Dry P-wave modulus was then computed for each study area from previously estimated dry bulk moduli. If the porosity is less than 0.35, the following relations can be utilized to obtain dry frame bulk modulus (Wang, 2001),

$$K_{dry} = K_o\left(1 - 3.39\varphi + 1.95\varphi^2\right), \quad \text{and} \quad (4)$$

$$G_{dry} = G_o\left(1 - 3.48\varphi + 2.19\varphi^2\right), \quad (5)$$

where φ is the fractional porosity. Coefficients shown next to the porosity in the equations are stiffness parameters determined by Wang (2001). K_{dry} and G_{dry} are the dry frame bulk and shear modulus respectively in Mpa. K_o is the mineral bulk modulus and G_o is the mineral shear modulus. Then mineral (M_o) and dry frame (M_{dry}) P-wave modulus can be obtained from

$$M_o = K_o + 4/3\, G_o \quad \text{and} \quad (6)$$

$$M_{dry} = K_{dry} + \frac{4}{3} G. \quad (7)$$

A second approach was also adopted to verify the results. The procedure behind this method is to create Reuss bounds to observe the effects of each fluid (gas and brine) on P-wave moduli. The Reuss bound lower-limit threshold is that beneath which rock frames do not have any elastic stiffness and form a suspension. Therefore, the P-wave modulus of a saturated porous rock frame should have values above the Reuss bound. In this study, the P-wave modulus was used to describe the Reuss bound and fluid substitution effects via the equations:

$$\Delta M_{Gass} = \Delta\left(K + \frac{4}{3}\mu \right)_{Gass} \quad \text{and} \quad (8)$$

$$\Delta M_{Gass} = \Delta K_{Gass}. \quad (9)$$

In Gassmann fluid substitution, the change in the shear bulk modulus is negligible: $\Delta\mu_{Gass} = 0$. From Equations (7) and (8) a Gassmann change of P-wave modulus (ΔM_{Gass}) corresponds to the change in bulk modulus (ΔK_{Gass}) caused by varying fluid substitution effects. The Reuss bound can be approximated for the P-wave modulus as

$$\left[\frac{1}{K_R} = \frac{\varphi}{K_f} + \frac{1-\varphi}{K_o} \right] \approx \left[\frac{1}{M_R} = \frac{\varphi}{M_f} + \frac{1-\varphi}{M_o} \right], \quad (10)$$

where K_R and M_R are the Reuss average bulk modulus and the P-wave modulus obtained by substituting $K_{dry} = 0$ and $M_{dry} = 0$ into Equations (1) and (2):

$$\left[\Delta K_{Gass}(\varphi) = \frac{\varphi}{\varphi_R}\Delta K_R(\varphi_R)\right] \approx \left[\Delta M_{Gass}(\varphi) \approx \frac{\varphi}{\varphi_R}\Delta M_R(\varphi_R)\right], \tag{11}$$

where φ_R is the intercept porosity, and $\Delta K_R(\varphi_R)$ and $\Delta M_R(\varphi_R)$ represent the Reuss average differences in bulk modulus and P-wave modulus, respectively. These discrepancies in Reuss averages are caused by two different saturating fluids at intercept porosity. First, the fluid substitution effect of the initial fluid on the P-wave modulus is marked on a porosity-modulus plot. A straight line is then drawn from the $M = M_o$ axis to the effective P-wave modulus of the initial fluid until the line intersects with its Reuss average at intercept porosity.

The Reuss average of the replacement fluid is determined by moving vertically up or down from the Reuss average of the initial fluid at intercept porosity. Another straight line is drawn from the estimated Reuss average of the replacement fluid toward the $M = M_o$ axis. The difference between the P-wave moduli of the initial and replacement fluids on the straight lines are marked at the previously known rock frame porosity. In this way, the effect of fluid substitution on elastic parameters, velocity changes, and reflection coefficients can be estimated (Figure 10).

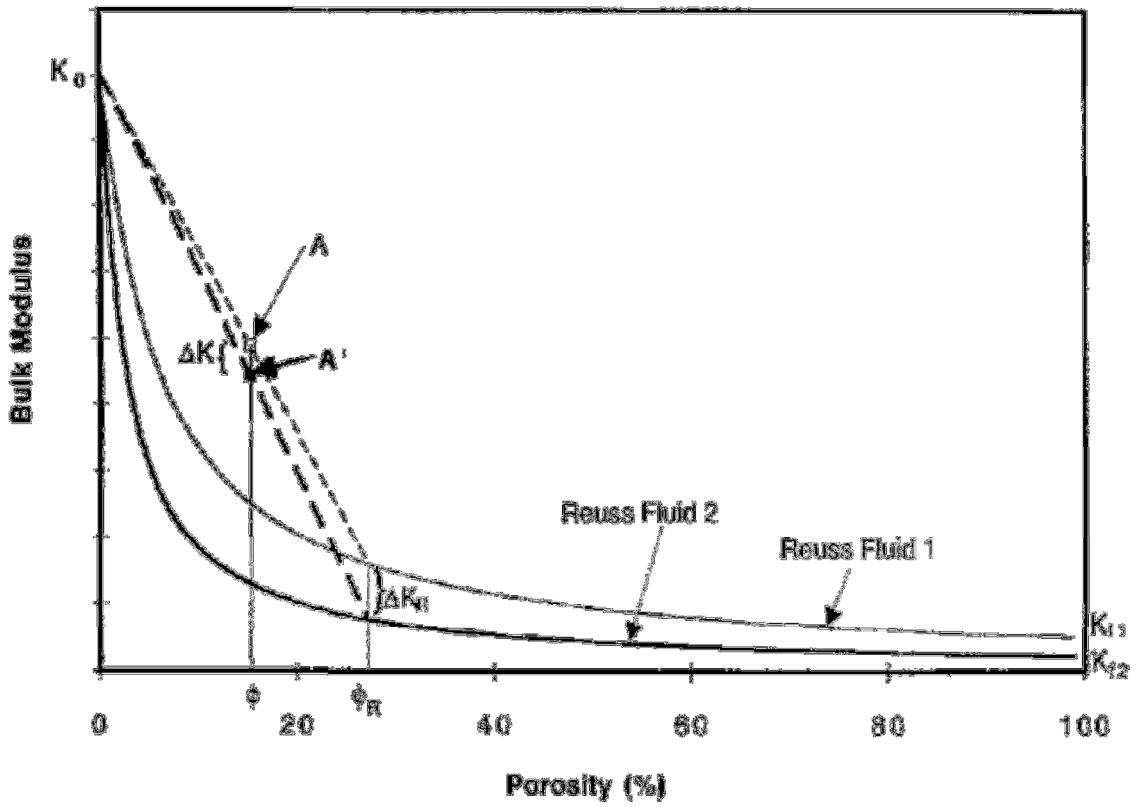

Figure 10. Graphical construction method for Reuss bounds.The change in the P-wave modulus M is estimated from the change in the Reuss curves at φ_R (Mavko, Chan and Mukerji, 1995).

2.2 Estimation of Gas Properties

Natural gas is principally composed of light alkanes such as methane, propane, and ethane. In a reservoir environment, hydrocarbon gasses are greatly affected by in situ conditions, including pressure and temperature. Gas-specific gravity (G) is used to describe hydrocarbon gasses. For instance, the lightest gas methane has a specific gravity of 0.56 at 15.6 ^{o}C and one atmosphere pressure. G can be defined as the ratio of gas density to air density at specific pressure and temperature values (see Equation 11). G is dimensionless and can range from the lightest methane at 0.56 to 1.8 for heavier gasses which include longer-chain hydrocarbons:

$$G = \frac{\rho_{gas}}{\rho_{air}}. \qquad (12)$$

In the characterization of gas properties, thermodynamic factors, and compositional effects should be taken into account. In nature, gasses are not completely pure. They generally exist in the form of gas mixtures. Pure gasses have a particular phase (solid, liquid, gas) depending on temperature and pressure. Phase change occurs beyond a critical point which is determined experimentally. Gas mixtures have a pseudo-critical point (temperature T_{pc} and pressure P_{pc}) that determines phase changes. Pseudo-reduced temperature T_{pr} and pressure P_{pr} are used to normalize compositional effects of a gas mixture, using

$$P_{pr} = P / P_{pc} = P / (4.892 - 0.4048G) \qquad \text{and} \qquad (13)$$

$$T_{pr} = T_a / T_{pc} = T_a / (94.72 + 170.75G). \quad (14)$$

In the above relations, G is the gas-specific gravity and T_a is absolute temperature, which is defined by

$$T_a = T\left({}^{o}C\right) + 273.15. \quad (15)$$

Gas density can be approximated by

$$\rho_{gas} \cong \frac{28.8GP}{ZRT_a}, \quad (16)$$

where P is the pore pressure in mega pascal (Mpa), Z is the compressibility factor and R is the molar gas constant (8.3144 joule), and ρ_{gas} is the gas density in g/cc. The parameter Z can be computed from

$$Z = \left[0.03 + 0.00527(3.5 - T_{pr})^3\right] P_{pr} + (0.642T_{pr} - 0.007T_{pr}^4 - 0.52) + E, \quad (17)$$

where E is given by

$$E = 0.109(3.85 - T_{pr})^2 \exp\left\{-\left[0.45 + 8(0.56 - 1/T_{pr})^2\right] P_{pr}^{1.2} / T_{pr}\right\}. \quad (18)$$

These equations allows calculations of gas bulk modulus k_{gas} :

$$k_{gas} \cong \frac{P}{(1 - \frac{P_{pr}}{Z}\frac{\partial Z}{\partial P_{pr}})_T}\gamma_0, \quad (19)$$

where γ_0 is the heat capacity ratio at a constant pressure and volume (Batzle and Wang, 1992), as in

$$\gamma_0 = 0.85 + \frac{5.6}{(P_{pr}+2)} + \frac{27.1}{(P_{pr}+3.5)^2} - 8.7\exp\left[-0.65(P_{pr}+1)\right]. \tag{20}$$

When gas bulk modulus and density are known, gas sound speed V_{gas} (m/s) can be calculated by the following (Liner, 2004):

$$V_{gas} = \sqrt{1000\frac{k_{gas}}{\rho_{gas}}} \approx V_{gas} = \sqrt{1000\frac{M_{gas}}{\rho_{gas}}}. \tag{21}$$

Gas and mineral density determine saturated rock density. Since this study assumes the reservoir rock is pure sandstone in every stage of seismic and Gassmann fluid substitution analysis, I used a quartz mineral density of 2.65 g/cc in calculations. Saturated rock density for each fluid (gas and brine) was estimated by the following (Liner, 2004):

$$\rho_{sat} = \rho_m(1-\varphi) + \varphi\rho_f, \tag{22}$$

where, ρ_{sat} is the saturated rock density, ρ_m is mineral density and ρ_f is the saturating fluid density.

Gas viscosity may substantially change at high temperatures, and at low pressures. Therefore, its effect needs to be considered. Gas viscosity is also primarily

controlled by thermodynamic factors and gas composition effects similar to gas density. Gas viscosity at one atmospheric pressure with the unit of centipoise is as follows (Batzle and Wang, 1992):

$$\eta_1 = 0.0001\left[T_{pr}\left(28+48G-5G^2\right)-6.47G^{-2}+35G^{-1}+1.14G-15.55\right], \tag{23}$$

where η indicates the viscosity at low pressure conditions, and.

$$\frac{\eta}{\eta_1} = 0.0001P_{pr}\left[\frac{1057-8.08T_{pr}}{P_{pr}}+\frac{796P_{pr}^{1/2}-704}{\left(T_{pr}-1\right)^{0.7}\left(P_{pr}+1\right)}-3.24T_{pr}-38\right]. \tag{24}$$

2.3 Characterizations of Brine Properties

One of the most abundant pore fluids in hydrocarbon exploration is brine. Pore-filling water may change from almost pure water to more saline water, termed brine. The northern Gulf of Mexico shelf depositions under the salt canopies display a high concentration of pore water salinity due to water flow and salt dissolution activities. Salinity values of the northern Gulf of Mexico range from 10000 ppm to 250000 ppm (Figure 11).

Once pore pressure, temperature and salinity are known, pure water and brine densities of pore water can be estimated through following expressions:

$$\rho_w = 1+1\times10^{-6}(-80T+3.3T^2+0.00175T^3+489P-2TP+0.016T^2P-1.3\times10^{-5}T^3P \\ -0.333P^2-0.002TP^2) \tag{25}$$

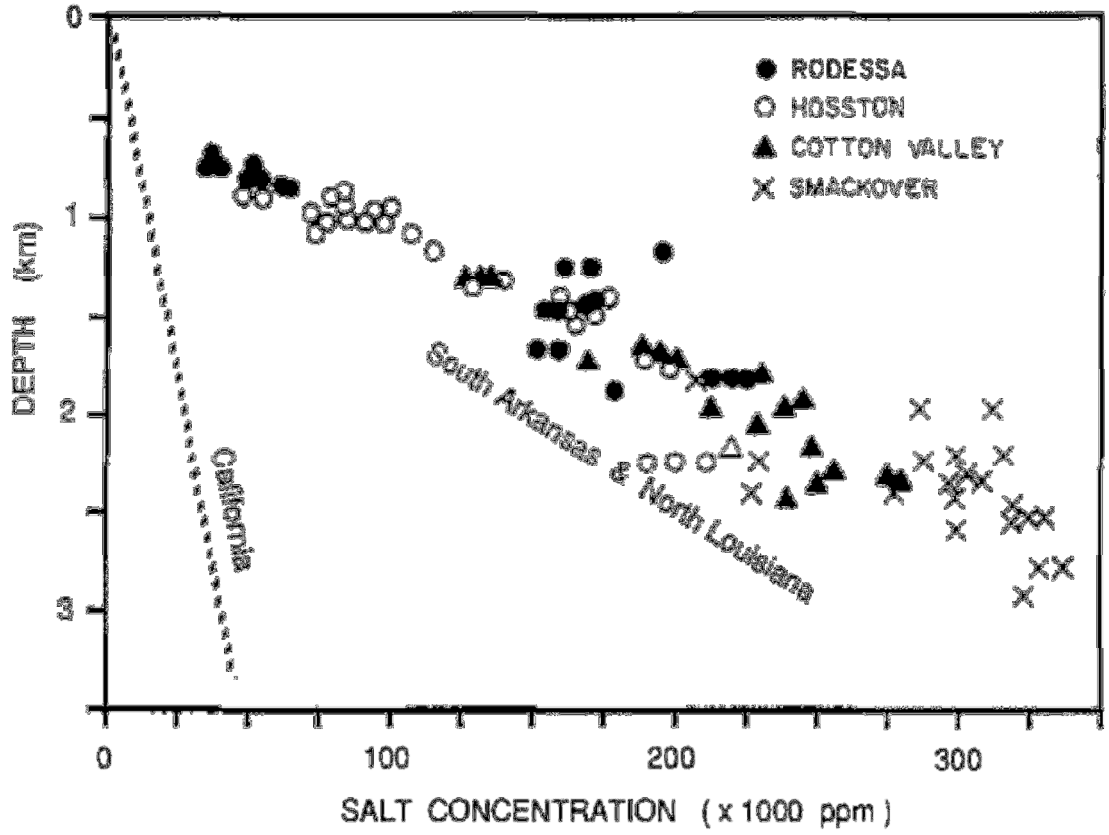

Figure 11. Salt concentration in sand water versus depth in southern Arkansas and northern Louisiana (after Price, 1977; and Dickey, 1966). These Gulf Coast data are for basins in which bedded salts are present. The relationship of increasing formation water salinity with increasing depth within the normally pressured zone generally holds for petroleum basins. However, in basins with only clastic sediments and no bedded salts, the maximum salinities will be much less. The California petroleum basins (Ventura, Los Angeles, Sacramento Valley, San Joaquin, etc.) rarely exceed 35000 ppm salt and the bulk are well below 30000 ppm (Batzle and Wang, 1992).

and

$$\rho_b = \rho_w + S\left\{0.668 + 0.44S + 1\times10^{-6}\left[300P - 2400PS + T(80 + 3T - 3300S - 13P + 47PS)\right]\right\}, \tag{26}$$

where ρ_w and ρ_b are the densities of water and brine respectively in g/cc; S stands for salinity of sodium chloride solution in ppm/1000000, P is pore pressure in Mpa, and T is formation temperature in ^oC. Pure water velocity (V_w) is determined at formation temperature and pore pressure conditions (Mavko, Mukerji, and Dvorkin, 2009), from

$$V_w = \sum_{i=0}^{4}\sum_{j=0}^{3} w_{ij} T^i P^j, \tag{27}$$

where w_{ij} are coefficients given in Table 1. After estimating pure water velocity, brine velocity of a sodium chloride solution can be computed by considering the effects of salinity, pore pressure, and temperature using the following (Batzle and Wang, 1992):

$$V_b = V_w + S\left(1170 - 9.6T + 0.055T^2 - 8.5\times10^{-5}T^3 + 2.6P - 0.0029TP - 0.0476P^2\right)$$
$$+S^{1.5}\left(780 - 10P + 0.16P^2\right) - 820S^2. \tag{28}$$

Brine may contain some amount of gas in solution. The volume of dissolved gas in brine is augmented by increasing pressure and diminishes with salinity. However, the amount of dissolved gas particularly for methane can be calculated under 250 ^{o}C by

$$Log_{10}\left(R_g\right) = Log_{10}\left\{0.712P\left|T - 76.71\right|^{1.5} + 3676P^{0.64}\right\} - 4 - 7.786S\left(T + 17.78\right)^{-0.306}. \tag{29}$$

At room temperature and pressure, R_g is the gas-water ratio. Gas bulk modulus (K_b) is given by

$$K_g = \frac{K_b}{1+0.0494R_g}, \tag{30}$$

where K_g is the gas bulk modulus in Mpa. Brine viscosity is a function of temperature, pressure, and salinity. Increasing temperature causes brine viscosity to diminish more effectively compared with pressure change. Furthermore, salinity is controlled by temperature and can also augment brine viscosity. A drop in brine viscosity can be created by dissolved gas. However, this effect can be neglected. The following equation was used to characterize brine viscosity under 250 ^{o}C and related pressure, and salinity conditions:

$$\eta = 0.1+0.333S+\left(1.65+91.9S^3\right)\exp\left\{-\left[0.42\left(S^{0.8}-0.17\right)^2+0.045\right]T^{0.8}\right\}. \tag{31}$$

Table 1. Coefficients for computation of water properties (Batzle and Wang, 1992).

$w_{00} = 1402.85$	$w_{02} = 3.437 \times 10^{-3}$
$w_{10} = 4.871$	$w_{12} = 1.739 \times 10^{-4}$
$w_{20} = -0.04783$	$w_{22} = -2.135 \times 10^{-6}$
$w_{30} = 1.487 \times 10^{-4}$	$w_{32} = -1.455 \times 10^{-8}$
$w_{40} = -2.197 \times 10^{-7}$	$w_{42} = 5.230 \times 10^{-11}$
$w_{01} = 1.524$	$w_{03} = -1.197 \times 10^{-5}$
$w_{11} = -0.0111$	$w_{13} = -1.628 \times 10^{-6}$
$w_{21} = 2.747 \times 10^{-4}$	$w_{23} = 1.237 \times 10^{-8}$
$w_{31} = -6.503 \times 10^{-7}$	$w_{33} = 1.327 \times 10^{-10}$
$w_{41} = 7.987 \times 10^{-10}$	$w_{43} = -4.614 \times 10^{-13}$

2.4 Fluid Substitution Analysis of Davy Jones

Characterization of the Davy Jones reservoir in terms of fluid substitution effects can guide the examination of the study areas in the Vermilion area, northern Gulf of Mexico. The Davy Jones is a proved gas discovery in South Marsh Island, its reservoir conditions provide some useful constraints in determining the reservoir properties of the study areas in the Vermilion. One such restriction can be related to geology of the study areas. Therefore, it can be suggested that the Wilcox shelf trend beneath South Marsh Island is preserved or at least not altered within the adjacent Vermilion targets.

The physical reservoir qualifications of the Davy Jones reservoir, such as pore pressure, formation temperature, porosity, and reservoir depth rates also establish fundamental control factors over the study areas. We assumed that our study areas demonstrate similar pressure, temperature, and compositional regimes as those of Davy Jones. In addition, estimation of the elastic parameters of the Davy Jones reservoir through fluid substitution made it possible to evaluate whether the study areas could result in coherent results based on their bright spot anomalies.

For these purposes, we modeled the Davy Jones reservoir with gas- and brine-filled features which were capped by a shale-based seal. Based on this model, brine-filled reservoir section underlain the gas saturated reservoir feature which is encased by a shale formation. Then we combined the equations for Gassmann fluid substitution and the relevant relations of Batzle and Wang in a Matlab program to analyze the effects of the gas and brine saturations of the Davy Jones reservoir based on our imaginary model.

Many input parameters reflecting the actual reservoir conditions of the Davy Jones reservoir were applied as can be seen in Table 4.

The gas substitution effect on the reservoir was estimated by assuming the gas was methane; so, gas density of methane was calculated. Then gas saturated density of the reservoir was estimated with the help of porosity and gas density. The next step was to compute the dry frame P-wave modulus and gas-saturated P-wave modulus of the reservoir through related equations. After gas-saturated density and P-wave modulus calculations, gas-saturated reservoir velocity was obtained leading to the computations of gas-saturated impedance and the reflection coefficient for the gas-filled reservoir section.

We followed a similar procedure in our brine saturation analysis of the reservoir. Initially, pure water density and the brine density were estimated by applying formation temperature, pore pressure, and salinity input parameters previously given in equations of Batzle. These parameters are shown in Table 4. Then, the calculation of pure water velocity via water property coefficients which were given in Table 1 leaded to the estimation of brine velocity. Gas-free brine bulk modulus of the reservoir was then deciphered with the aid of previously determined brine bulk modulus and gas-water ratio (R_g). Dry fame bulk modulus, which was already estimated during the calculations for gas substitution, was also able to be used for the brine-saturated case.

The brine P-wave fluid modulus is the only parameter that undergoes most of the changes during brine substitution, and its effect on the reservoir is reflected by the brine saturated P-wave modulus. It was simply obtained through Equation 2. Lastly, brine-

saturated impedances and reflection coefficients of the reservoir were computed based on the previously defined model. The combined representation of brine- and gas-saturated reflection coefficients versus changing shale impedances were plotted to show whether the brine and gas effects on the reservoir could be distinguished or not. As shown in Figure 12, brine- and gas-saturated reflection coefficients can clearly be separated from each other.

In terms of reservoir and seal features in the model, we anticipated that the seal formation would demonstrate a broad range of seismic velocity and density values due to its complex composition. Therefore, a wide scale of shale velocity and density values starting from 2500 m/s to 6000 m/s and from 1.8 g/cc to 2.6 g/cc was used to compute reflection coefficients of gas- and brine-filled reservoir sections. However, the reservoir section is composed of Wilcox sandstones which are primarily made of quartz minerals. So the quartz mineral bulk and shear modulus were utilized in the fluid substitution of the Davy Jones reservoir.

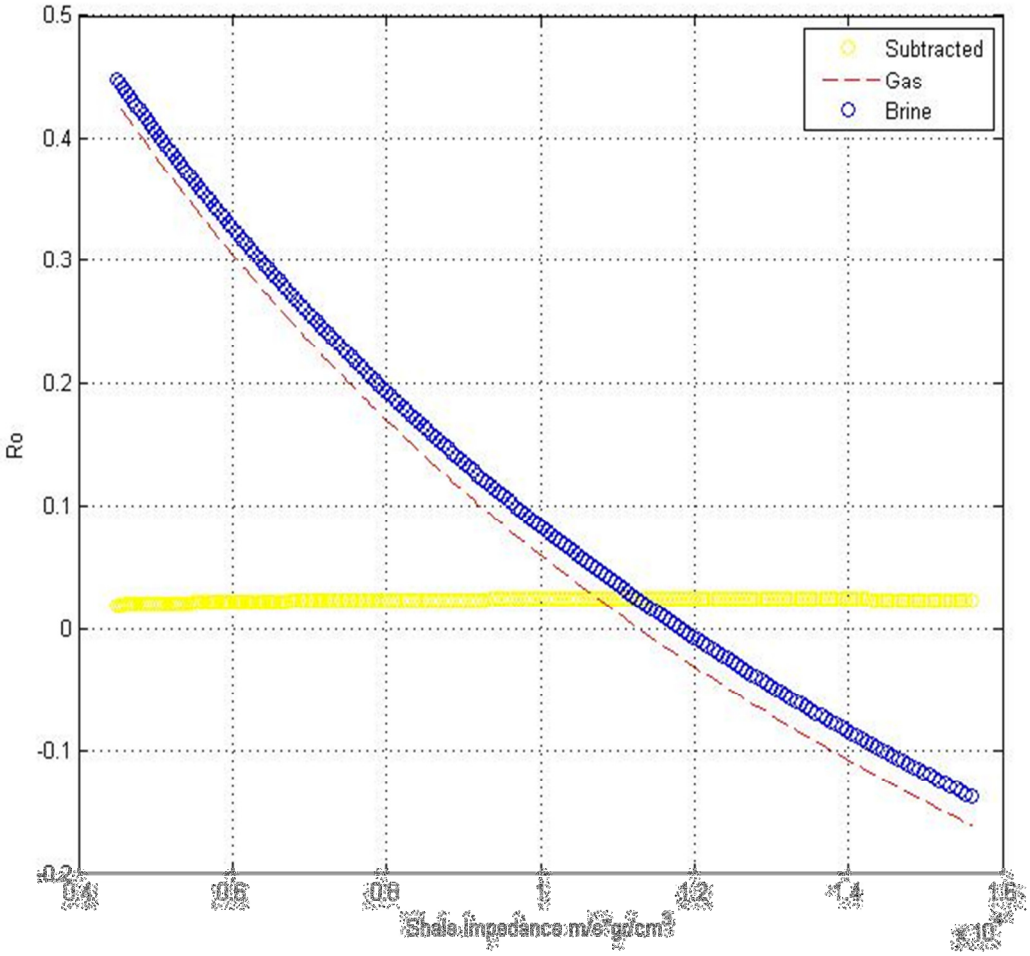

Figure 12. Brine (blue curve) and gas (red dashed curve) saturated sand reflection coefficients versus seal impedances.

2.5 Seismic Amplitude Interpretation

We are primarily interested in the successful identification and analysis of five study areas which are considered to demonstrate amenable amplitude bright anomalies in the Vermilion area, northern Gulf of Mexico. Characterization of the study areas based on distinctive amplitude bright spot signatures proved valid using two physically different approaches: Seismic interpretation and fluid substitution analysis.

Seismic interpretation directly pinpoints the positions of these particular bright spot signatures in the seismic data and provides some useful tools to quantify their responses. Fluid substitution analysis of the study areas helps to articulate whether the seismically anticipated bright spots are truly responsive or not. These tasks were accomplished in several steps, as shown in Figure 13. The first task was to assign the study areas for the characterization of bright spot anomalies. However, the depth information of seismic data set was limited since the data set has only one well that penetrates to 5,000 m. Therefore, deciphering trustworthy velocity information beyond this depth was a significant task in order to ensure that the geological events would sit in the correct places in terms of actual depth. Precise depth information of interested reservoir candidates was critical to implement the rest of the steps of the seismic amplitude interpretation and fluid substitution.

A simple depth conversion of the seismic data up to 9,150 m was obtained (Figure 14b) by using the current well information up to 5,000 m and a depth-velocity model of a seismic section of the northern GoM (Figure 14a, Snyder, et. al, 2010). This depth-

velocity model was constructed based on several check shots on wide azimuthal seismic data within the south Louisiana shelf section. Specifically, velocity trends of South Marsh Island, Eugene Island, and Ship Shoal Island in the Louisiana shelf were examined. Since South Marsh Island is adjacent to the Vermilion area, this model can be used to understand the velocity trends of the Vermilion.

The procedure behind the computation of velocities for the Vermilion was to compare the velocity trends of the depth-velocity model with the calculated velocity information of the existing well up to 5,000 m. Computation of velocity on the seismic section was made based on the sonic transit time velocity conversions from the well. Then a velocity region was determined on the velocity-depth model consistent with the well calculations up to 5,000 m. This velocity region from the model was then utilized vertically to extend velocity information up to 9,150 m.

Our calculated depth-velocity information for the Vermilion is in a well agreement with the general velocity trends from the Gulf of Mexico (GoM) which were studied by Hilterman (1999 and 2011). Hilterman (1999 and 2011) claims that overall velocity and density trends of shale and sand sequences as a function of depth should be considered depending on the depth location of observed geopressure in the GoM (Figures 15 and 16). Below and above the geopressure zones, velocity and density trends of shales and sands show different characteristics.

Hilterman (1999 and 2011) observed that general velocity and density trends of sands remain unchanged above and below the geopressure zones which occur at about 3,000 m below the mud-line. In contrast, shale density and velocity values increased

more slowly below the geopressure zone. This effect of a geopressure zone had to be taken into account while studying the amplitude responses of lithologies at these depths. In this manner, our computed depth-velocity values of the Vermilion do not show significant deviations from the average sand and shale velocity trends of Hilterman (1999 and 2011). Furthermore, a regional seismic line in the vicinity of the Vermilion area interpreted by Radovich (2003), suggests that the Tertiary-Wilcox deposition is located within the two-way travel time window of 5.5 - 7.5 seconds on the same seismic line, depending on the position of the shelf section from south to north (Figure 17). Based on a simple velocity-depth conversion for the Vermilion area and the interpreted regional seismic line of Radovich (2003), we assigned a time range between 6 and 7 seconds on the seismic data to include reservoir candidates after having general depth information of the data set.

Mainly, some candidate study areas on the seismic data were chosen by using time slices starting from 6 to 7 seconds with the time sample rate of 0.1 ms. Since time slices of a seismic section provide horizontal views of amplitude changes at an assigned time window, high negative (through) amplitude regions were marked as candidate study areas. Then, those candidate regions were projected on to the vertical seismic sections from the intersections of time slices and vertical seismic sections at designated time ranges. Mostly, those candidate areas overlapped with strong negative reflectors on the seismic sections.

However, each reflector with intensive negative amplitudes could not be assigned as a bright spot indicator since a reflector needed to additionally display closure features

and amplitude changes between their crests and the descending part of the reflector. That is, it was presumed that brine saturation on a reflector is marked by moderate negative amplitudes in comparison to the gas-saturated part of a reflector which is represented by high negative amplitudes toward its crest. A desired reflector may also expose bent features emphasizing a closure of the reservoir structure. This may be related to fault interference or might simply be an indication of an anticline feature.

In this way, five study areas were established from the seismic data based on their coherencies with the desired forms of reflectors. Locations and time ranges of each study area are given in Table 2. Each study area was simply named with a letter N and an order number starting from 1 to 5 as shown in Table 2. The first of the five study regions is denoted as N1 and its time slice and related arbitrary vertical seismic section was presented in Figures18 a and b. It is evident on the each display of Figure 18 that an intensive negative amplitude region marked on the time slice corresponds to a reflector which shows amplitude changes from its descending part (moderate negative amplitude) to the crest of the reflector (high negative amplitude).The descending moderate amplitude region was assumed to be the brine-saturated feature of the reflector changing into a gas-saturated section with a higher negative amplitude at the crest.

Each reflector of interest was searched for fault interferences before horizon tracking of the reflector. Some faults were discovered in the vicinity of the study areas and they were interpreted by creating fault surfaces to determine their dips and strikes as well as their potential to disturb study regions. Then, each reflector was picked laterally by using the automatic 2D-hunt horizon tracking tool of the SMT seismic interpretation

software. All seismic interpretation tasks were conducted with the aid of this software. The subsequent process of the seismic tasks included the generations of time-horizon and amplitude maps of the area N1; this is shown in Figure 19.

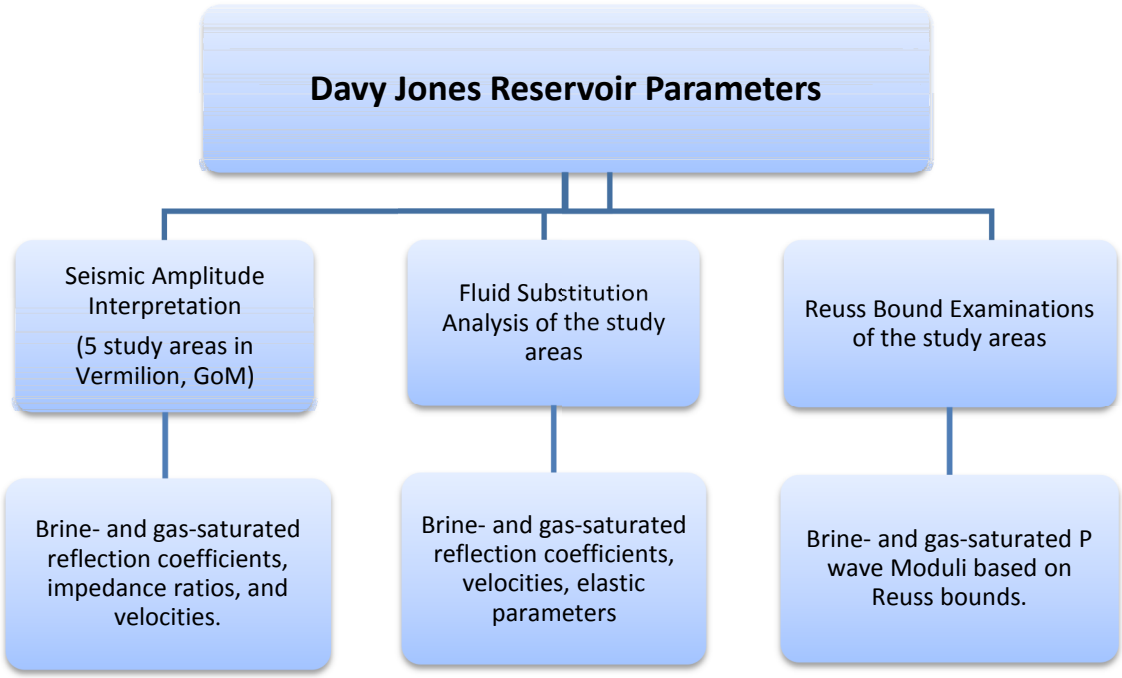

Figure 13. A workflow diagram of the effective processes in characterizations of the areas.

a)

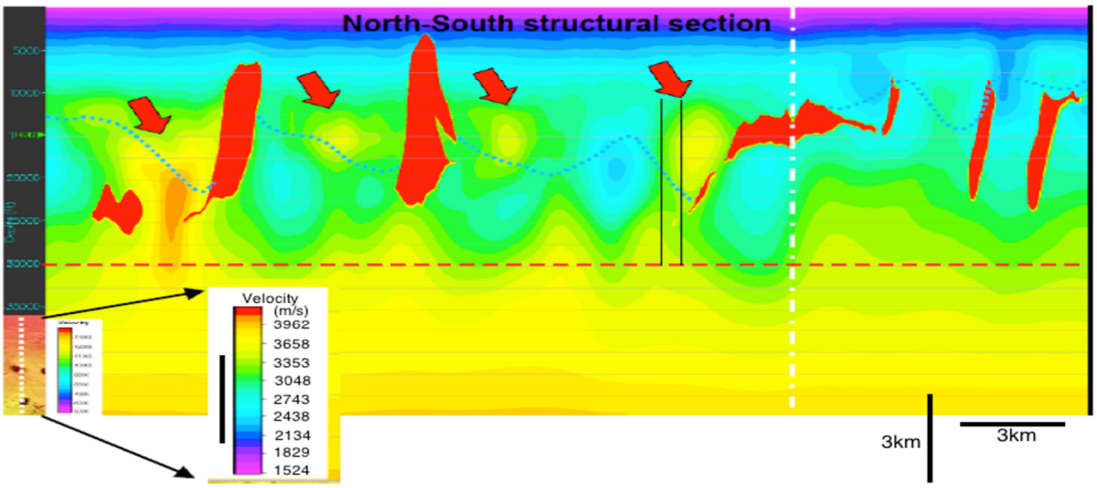

b)

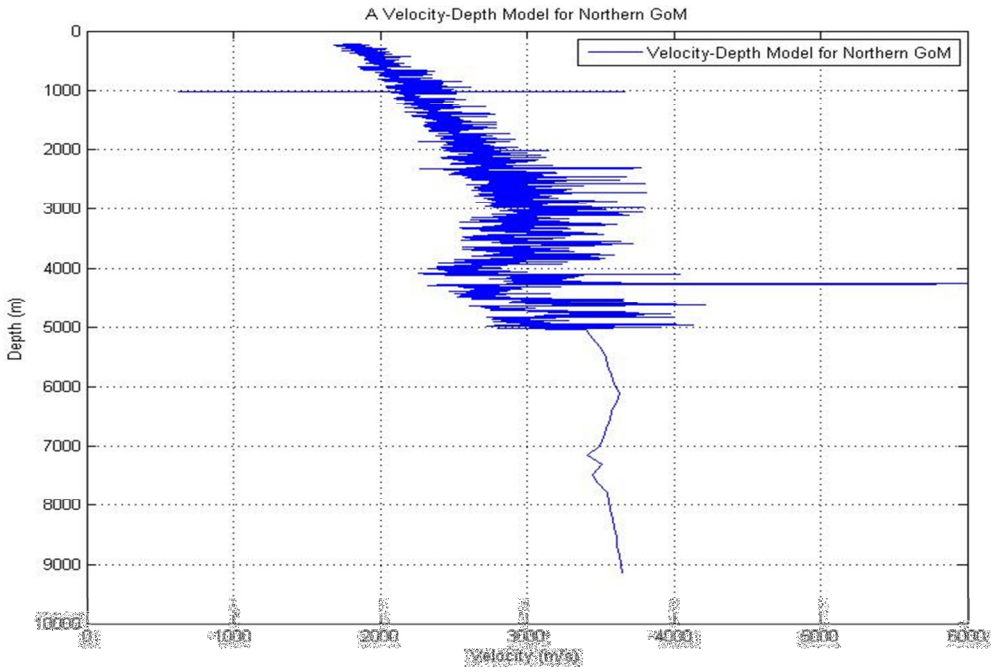

Figure 14. Velocity- Depth models for northern GoM (a) A Velocity-Depth model from Eugene Island, northern GoM. Black lines indicate a region of velocity values corresponding to the sonic log information. Red dashed lines mark the depth boundary of interested prospects based on Davy Jones Discovery (Snyder et. al, 2010). (b) A computed velocity-depth model for Vermilion area, northern GoM using both Figure 14 (a) and sonic log information from the data set (up to 5,000 m).

a) b)

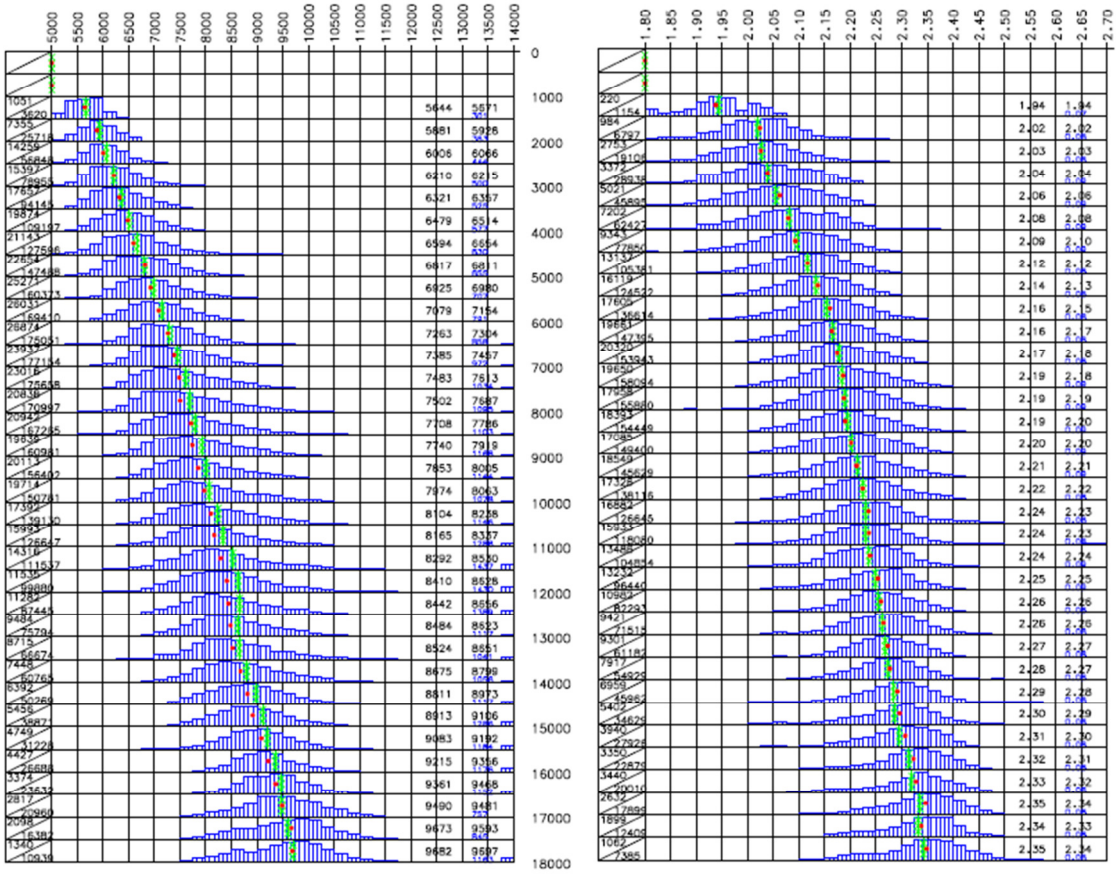

Figure 15. Sand P-wave velocity-depth and density-depth trends. (a) The black number at the right is the average velocity in the 150-m interval. The blue number is one standard deviation. The number in black at the left side of blue number represents recalculated average sand velocity after removing values larger than a standard deviation. The depth is below mud line. (b) Density log statistics with a fitting curve (green curve). Red point represents average density in each 150-m interval (Hilterman,1999).

a)

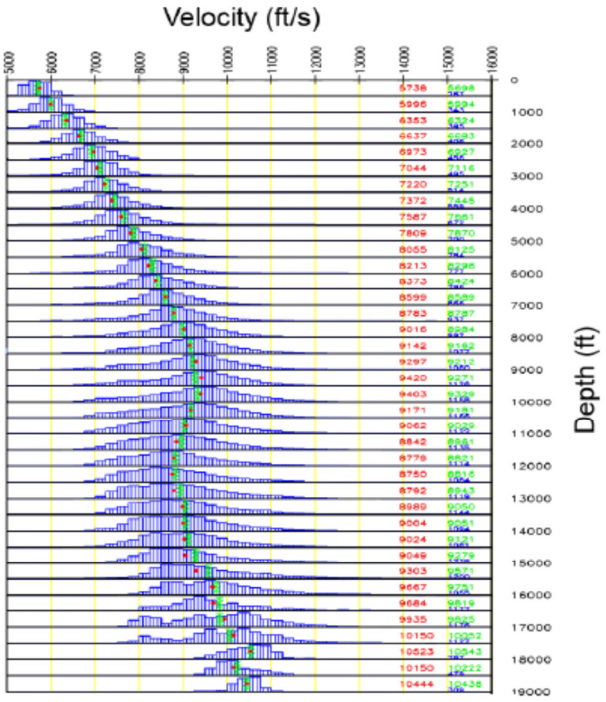

b)

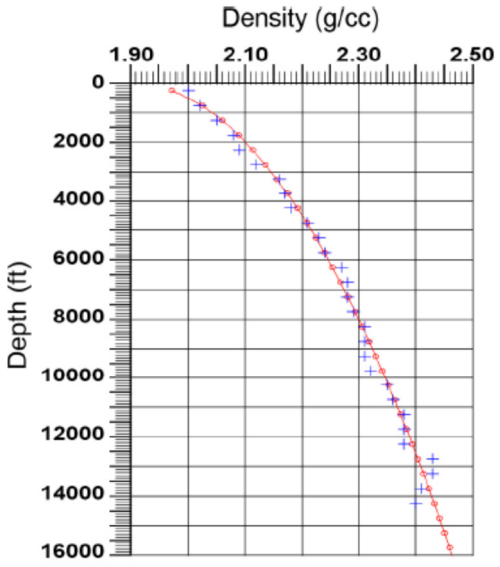

Figure 16. Shale P-wave velocity-depth and density-depth trends. (a) The green number at the right is the average velocity in the 150-m interval. The blue number is one standard deviation. The number in red represents recalculated average shale velocity after removing values larger than a standard deviation. The depth is below mud line. (b) Density log statistics with a fitting curve (red curve). Blue cross represents average density in each 150-m interval (Hilterman, 2011).

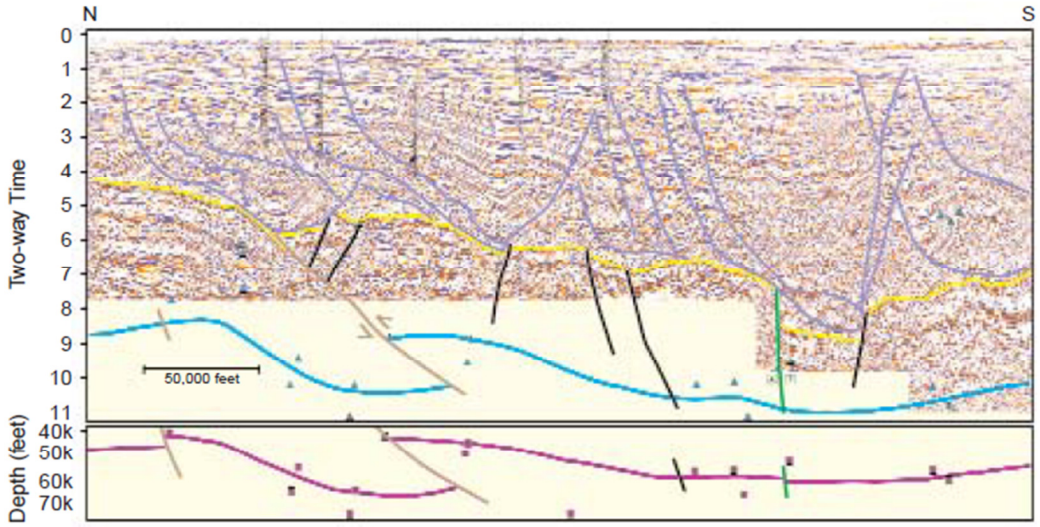

Figure 17. A regional 3-D seismic line from shelf south Louisiana. The correlation of the seismic-structural interpretation of the Tertiary and Mesozoic section to the high-resolution aeromagnetic-derived basement structure is shown on this regional 3-D seismic line from the Gulf of Mexico Shelf. The top of the Cretaceous is interpreted as the yellow horizon. The extension faults are colored black, thrust faults are colored brown, and the transfer fault is green. The time basement horizon is in blue, and the depth (subsea) basement horizon is purple. Discrete magnetic depth estimates, both basement and intrasedimentary, are displayed as blue and purple symbols (Radovich, 2003).

Table 2. Positions and time ranges of the five study areas (N1-N5) on seismic sections and relative profile lengths used in computations of brine- and gas-saturated amplitude ratios.

Areas of Interest	Inline	X line	Time (s)	Profile Length (m)
N1	**273**	**713**	**6.474**	**434**
N2	**312**	**683**	**6.38**	**424**
N3	**215**	**1143**	**7.044**	**431**
N4	**475**	**537**	**6.471**	**245**
N5	**526**	**490**	**6.702**	**400**

a) b)

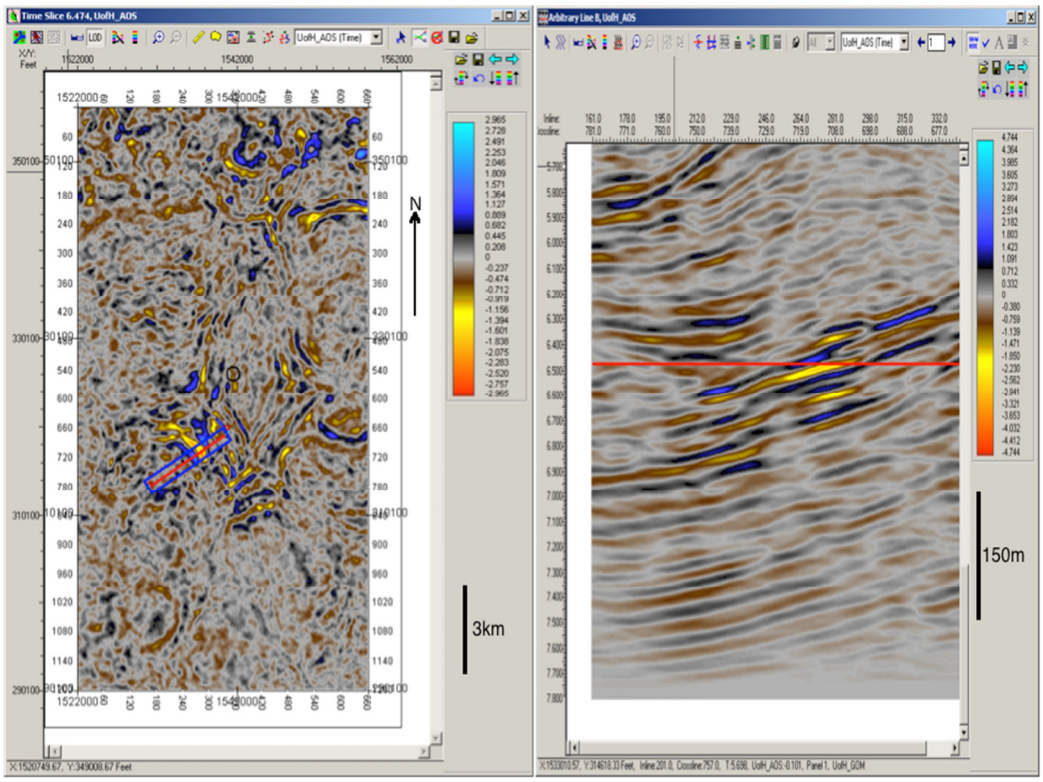

Figure 18. The study area N1. (a) Time slice of the area N1. (b) An arbitrary seismic view of the reflector N1

a) b)

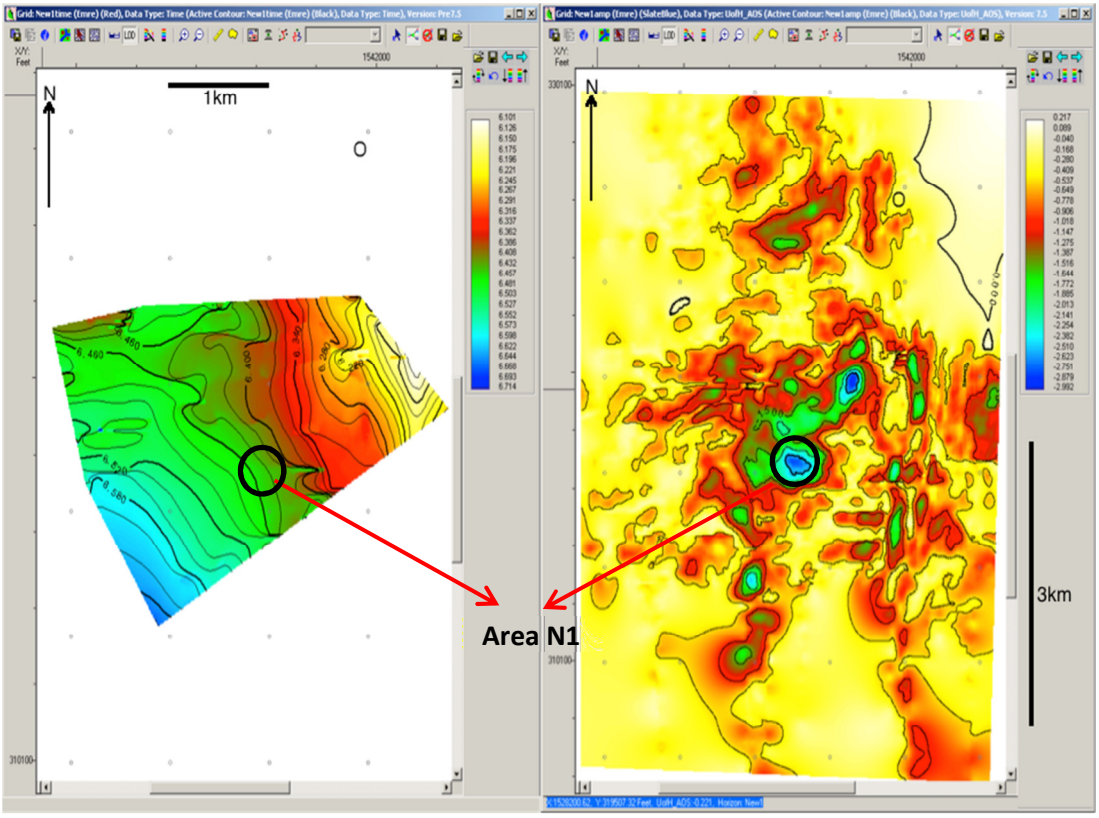

Figure 19. Seismic interpretation of N1 (a) Time structure and (b) amplitude maps of N1.

The area N1 which is marked on the time (horizon) structure map (Figure 19 a) can be located at about 6.5 seconds, roughly in the middle of the map. However, its position on the time amplitude map is distinguished by its high negative amplitude anomaly that ranges between -2.2 and -2.8. It is clearly seen on the time amplitude map that there are two nested concentric contour systems close together. The smaller inner contour was presumed to be the gas-saturated reservoir section while the outer contour system was thought to mark the brine-saturated reservoir feature for area N1. Figure 20 shows the time slice and regarding vertical seismic section of the area N2.

a) b)

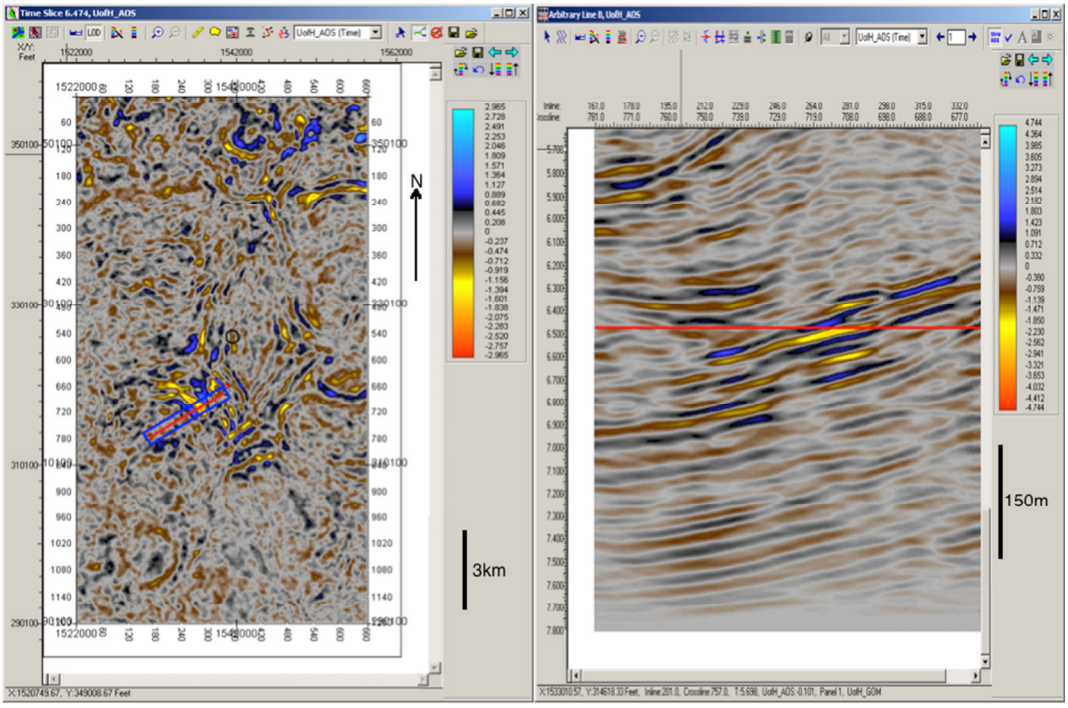

Figure 20. The study area N2. (a) Time slice of the area N2. (b) An arbitrary seismic view of the reflector N2.

Area N2 is located close to area N1 and this can clearly be seen on the time-structure and amplitude maps of N2 in Figure 21.

a) b)

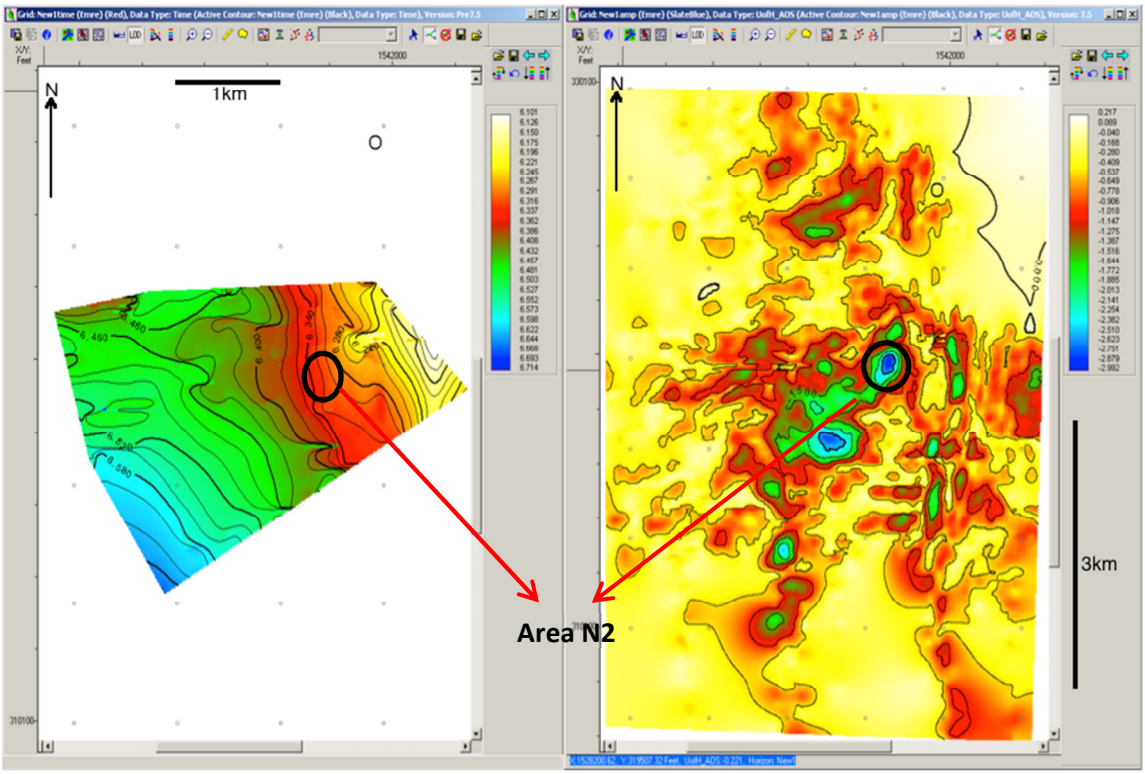

Figure 21. Seismic interpretation of N2 (a) Time structure and (b) amplitude maps of N2.

An exaggerated form of the time amplitude maps was used to compute relative amplitude ratios of brine-saturated and gas-saturated features on the study areas. The purpose of this process was to be able to estimate reflection coefficient ratios of brine- and gas-saturated sections for each study area. In order to achieve this, arbitrary profiles which represent longitudinal extensions of brine and gas saturated features were drawn on the amplitude maps. Figure 22a displays these sketches for the areas N1 and N2. Average amplitudes of brine- and gas-saturated features were counted in each region.

a) b)

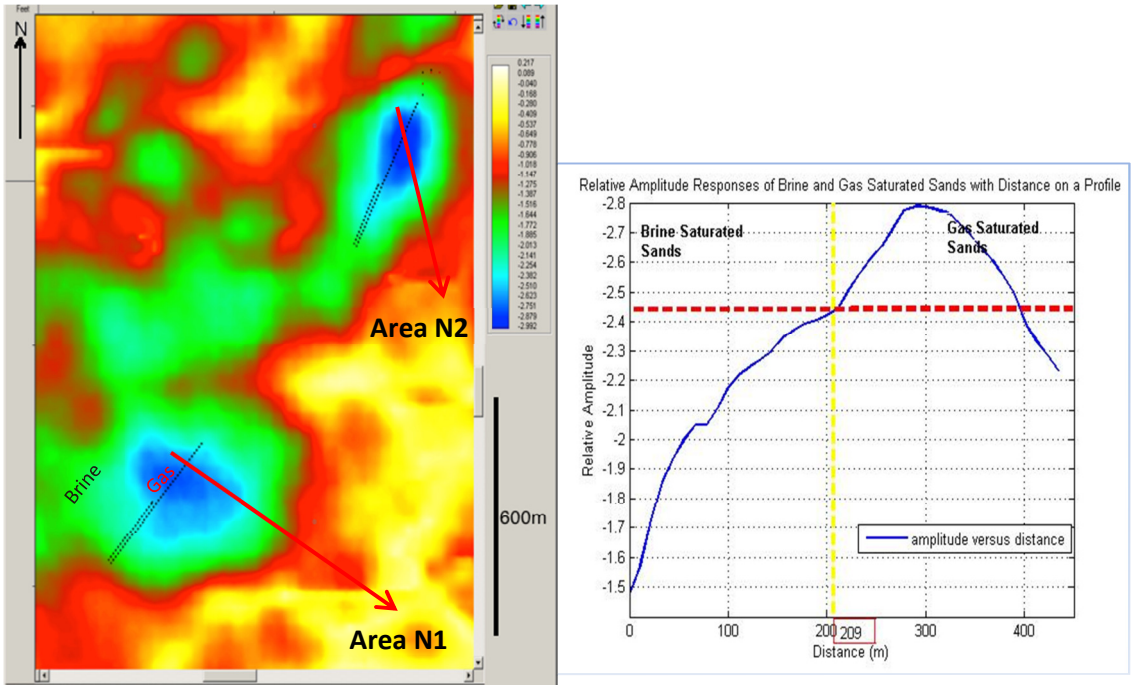

Figure 22. Estimation of relative reflection coefficients for N1. (a) Amplitude map of N1 and (b) computation of relative amplitude ratios for N1.

Then, their relative amplitude ratios were calculated. This led to the estimation of reflection coefficients by assuming the relative amplitude ratios of brine- and gas-saturated areas to be approximately equal and able to be replaced with reflection coefficients for the same features. Figure 22b demonstrates a procedure to compute the ratio of reflection coefficients by the following relations:

$$\frac{A_{gas}}{A_{brine}} \cong \frac{R_{gas}}{R_{brine}}. \qquad (31)$$

For the study area N1 the relation can be adjusted by

$$\frac{A_{gas1}}{A_{brine1}} \cong \frac{R_{gas1}}{R_{brine1}}, \tag{32}$$

$$\frac{R_{gas1}}{R_{brine1}} \cong \frac{-2.5889}{-2.1012} = 1.2321. \tag{33}$$

a) b)

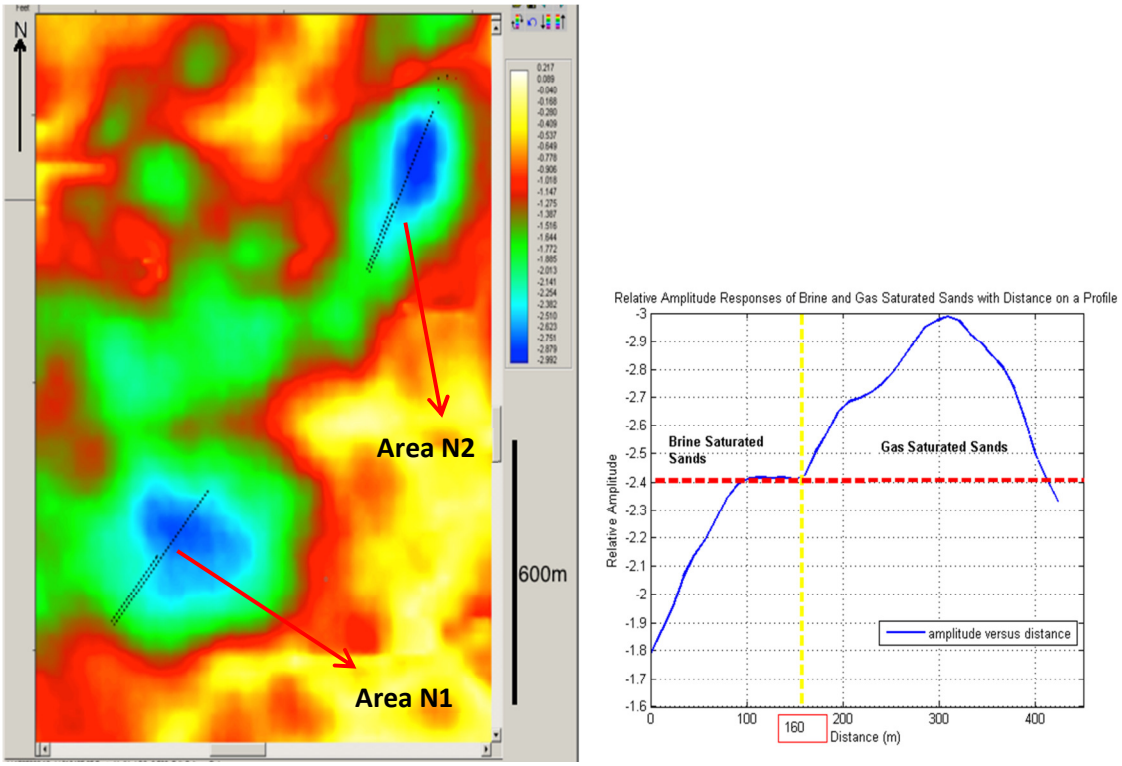

Figure 23. Estimation of relative reflection coefficients for N2. (a) Amplitude map of N2 and (b) computation of relative amplitude ratios for N2.

The ratios of reflection coefficients for the rest of the study areas (N3-N5) were computed with the same process. Obtained results can be found in Table 11. The study area N3 is located at around 7 seconds on the vertical seismic section. Figure 24 shows the time slice of N3 and its corresponding arbitrary vertical view of the seismic. Again

the brighter yellowish feature of the reflector is assumed to be the gas-saturated reservoir section, whereas the brownish part of the reflector indicates brine saturation in respect to amplitude threshold. Fault interferences clearly appear in two different directions on the time structure map of N3. One fault is close to the study area and passes through northwest of N3 while the other fault is located west of N3 at around 7 seconds and can be seen in Figure 25a. N3 is fairly distinguishable with its high negative amplitude on the amplitude map seen in Figure 25b.

a) b)

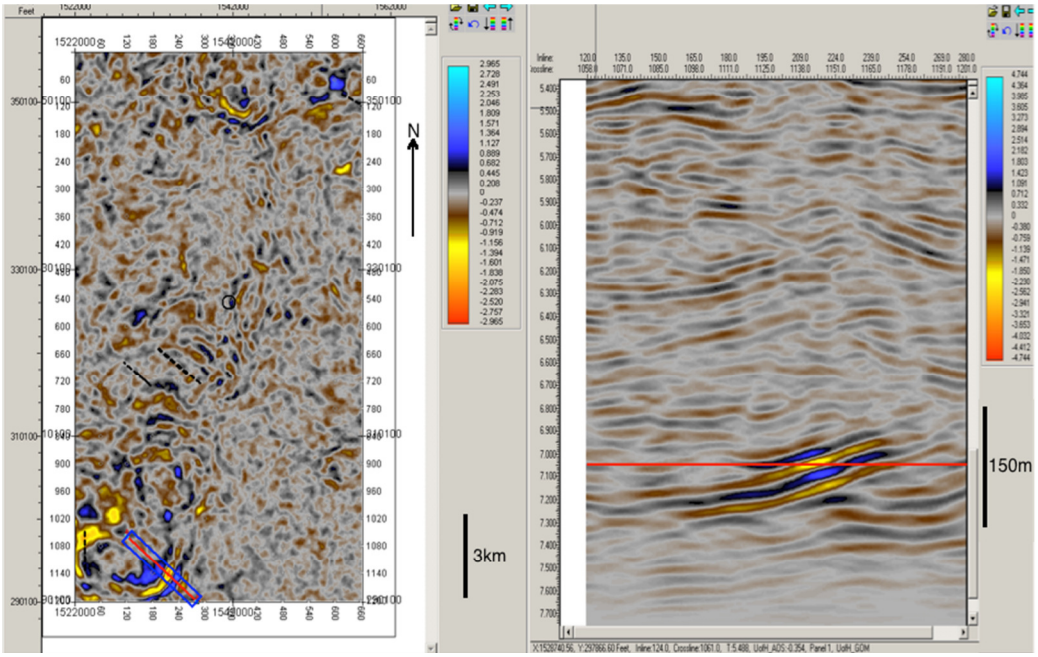

Figure 24. The study area N3. (a) Time slice of the area N3. (b) An arbitrary seismic view of the reflector N3.

a) b)

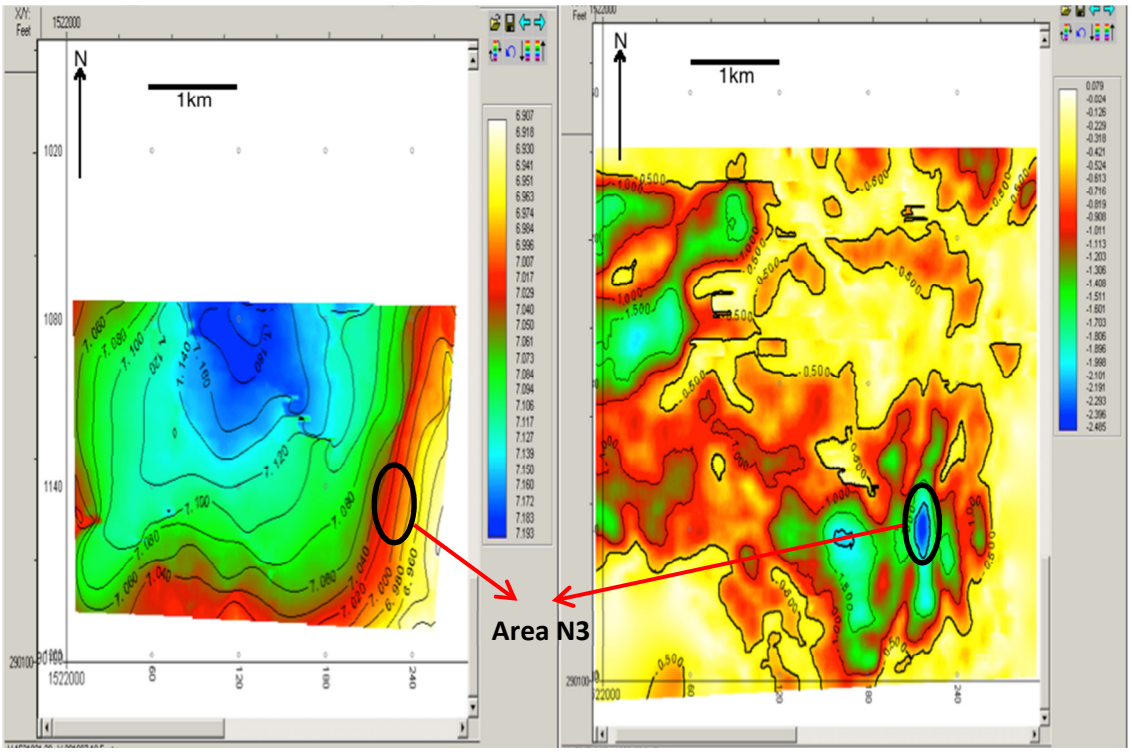

Figure 25. Seismic interpretation of N3 (a) Time structure and (b) amplitude maps of N3.

Two parallel profiles were then drawn on the amplitude map of N3 to represent the average diameters of the brine- and gas-saturated sections. This led to the estimation of the average amplitudes of brine- and gas-saturated sections demonstrated in Figure 26a. Calculated amplitude ratios made possible the computation of reflection coefficients for N3.

a) b)

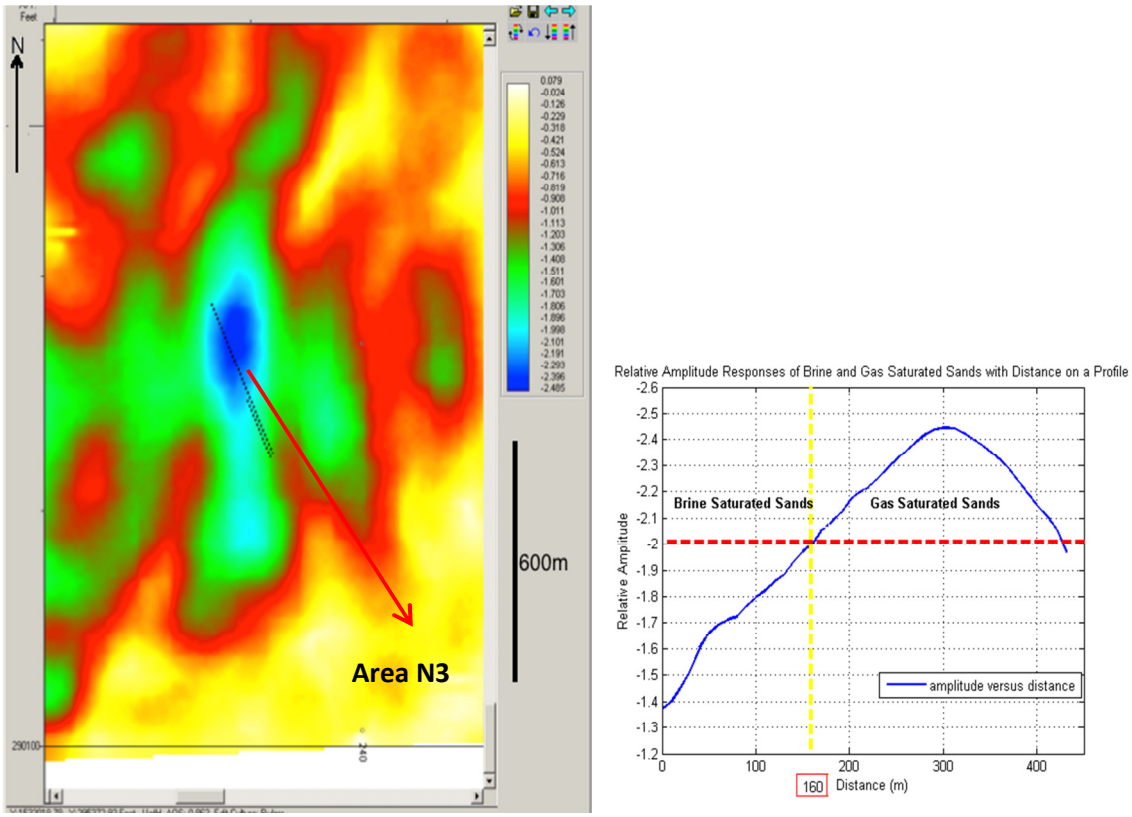

Figure 26. Estimation of relative reflection coefficients for N3. (a) Amplitude map of N3 and (b) computation of relative amplitude ratios for N3.

The study areas N4 and N5 are also located close to each other in terms of time and distance, like study areas N1 and N2. Because of this, they can be identified in time slices, time structure maps, and amplitude maps together. Figures 27a and b show their time slices and arbitrary vertical seismic views respectively. Study area N5 is narrower than area N4; this is clearly shown in Figure 28b. The calculations of amplitude ratios and reflection coefficients for N4 and N5were made based on their plots shown in Figure 32 and related outcomes for N4 and N5 are given in Tables 7 and 8.

a) b)

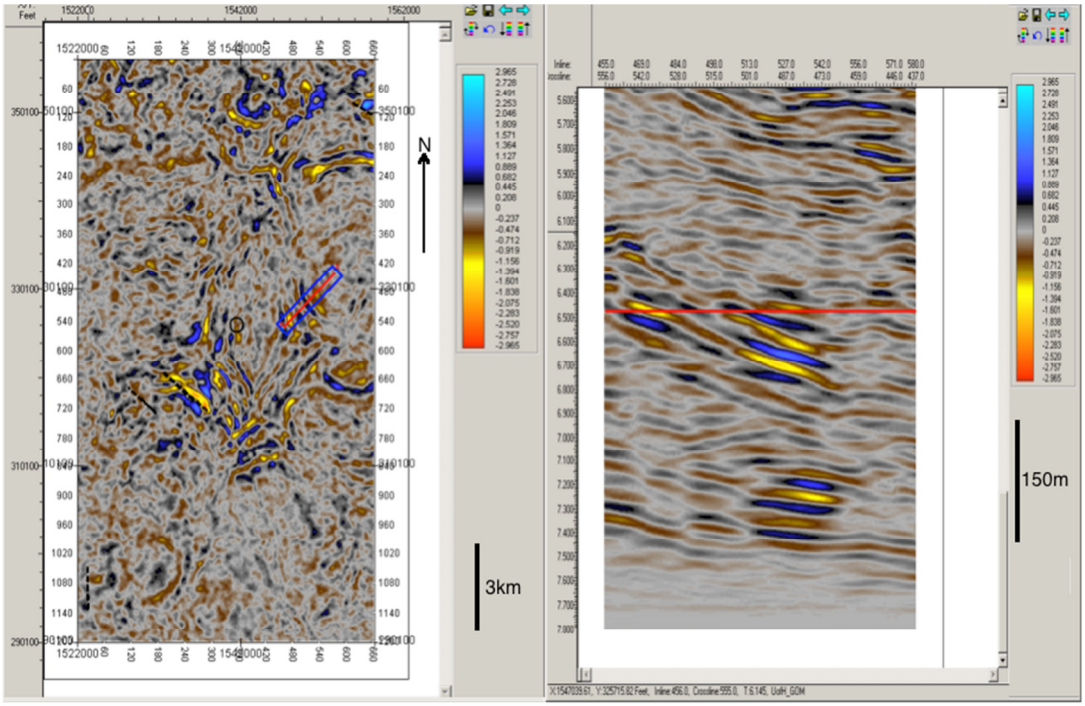

Figure 27. The study area N4. (a) Time slice of the area N4. (b) An arbitrary seismic view of the reflector N4.

a) b)

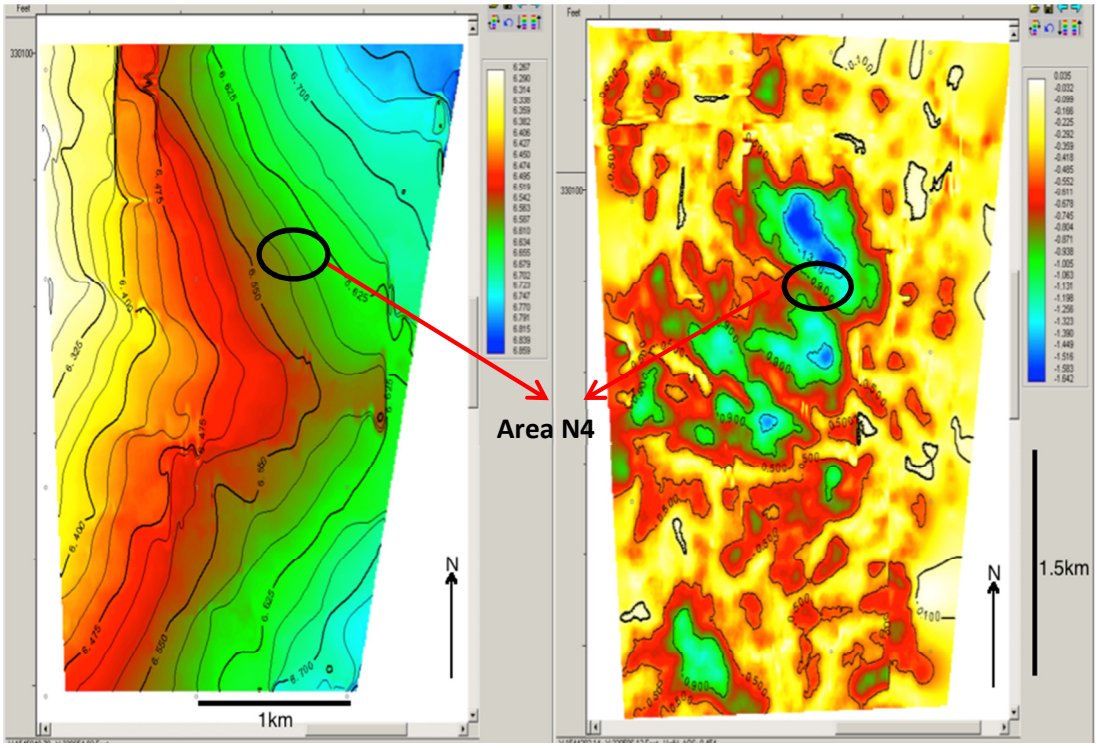

Figure 28. Seismic interpretation of N4 (a) Time structure and (b) amplitude maps of N4.

a) b)

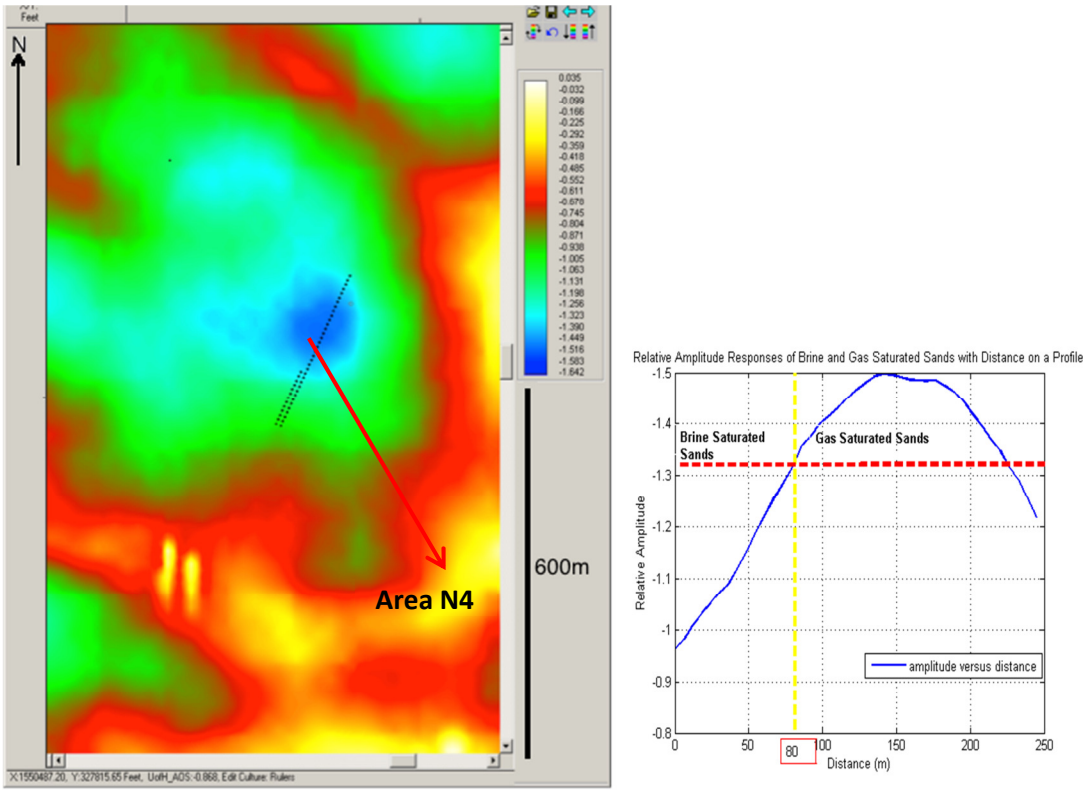

Figure 29. Estimation of relative reflection coefficients for N4. (a) Amplitude map of N4 and (b) computation of relative amplitude ratios for N4.

a) b)

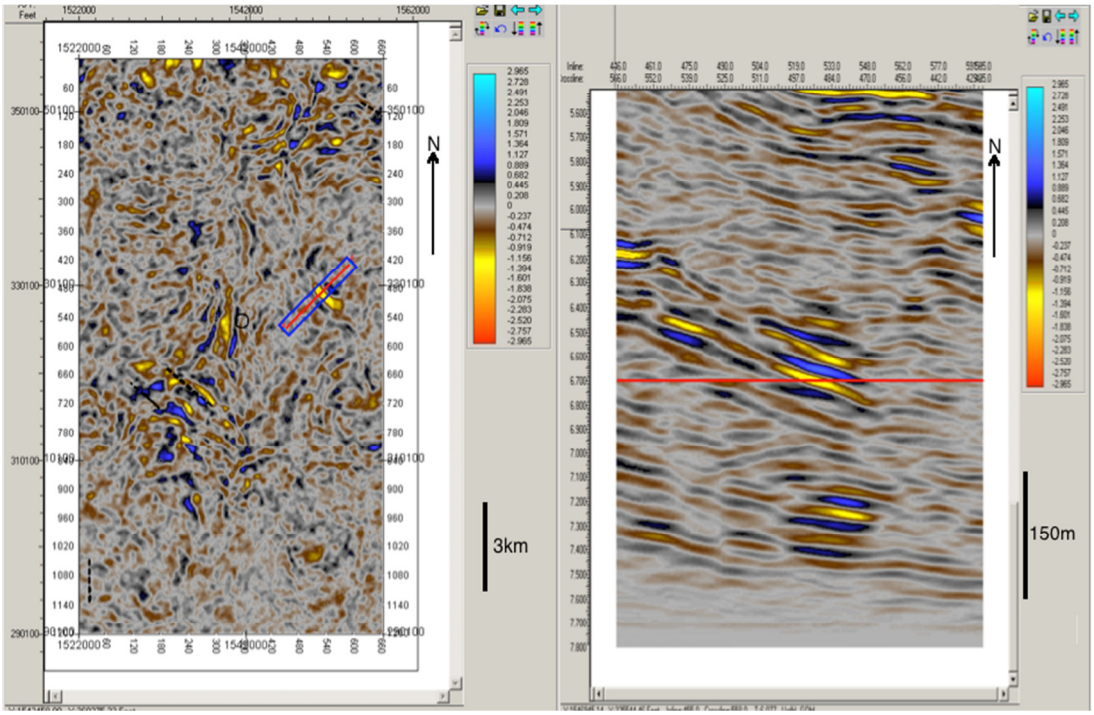

Figure 30. The study area N5. (a) Time slice of the area N5. (b) An arbitrary seismic view of the reflector N5.

a) b)

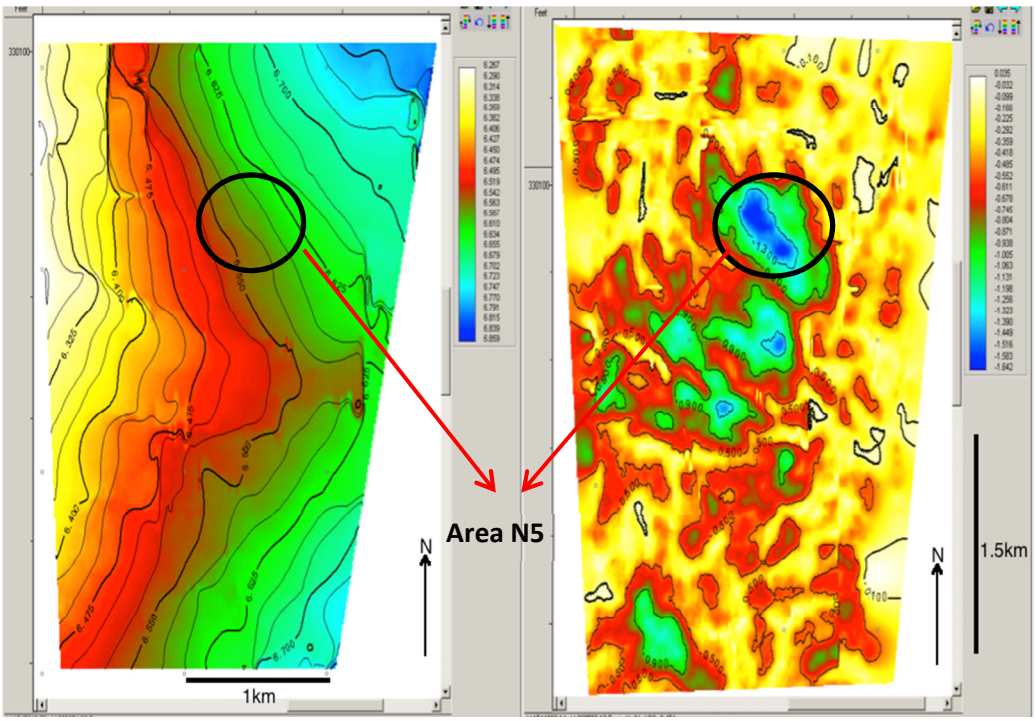

Figure 31. Seismic interpretation of N5 (a) Time structure and (b) amplitude maps of N5.

a) b)

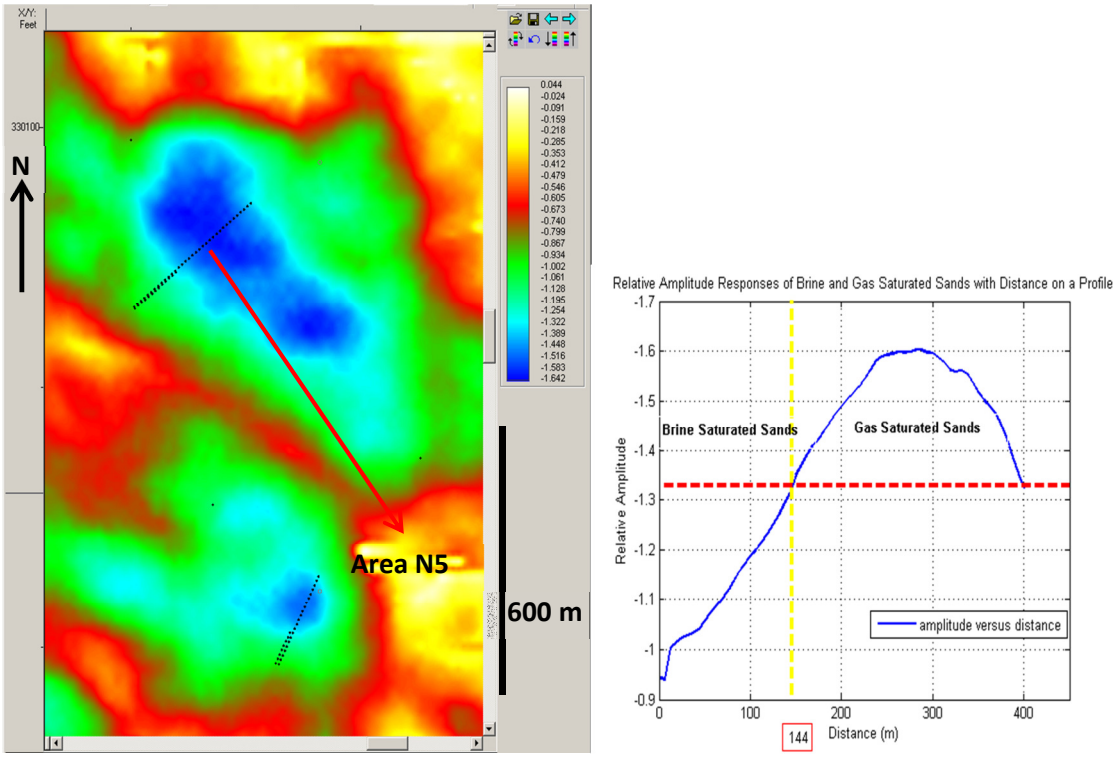

Figure 32. Estimation of relative reflection coefficients for N5. (a) Amplitude map of N5 and (b) computation of relative amplitude ratios for N5.

2.6 Fault Interpretation

General profiles of the faults encountered in the vicinity of the study areas are nearly similar to each other in terms of their shape and characteristics. They are generally in the form of normal fault segments. In some places they are archaic and they have shorter legs, whereas in some regions they consist of more linear-shaped, prominent, and substantial fracture zones. This clearly implies the existence of Wilcox growth fault system within the study regions and the related Wilcox deposition. Virtually some of the

faults can be tracked on time structure maps of the study regions by their disturbances on the time contours and abrupt time differences among adjacent structures.

However, interpretations of the faults were mostly focused on their interferences with the study areas and their potential effect on the predictions of our Gassmann fluid substitution analysis. Fault interpretation of the study areas did not involve detailed quantitative interpretations; rather it was only considered to be based on their qualitative interpretations. This is because the purpose of fault interpretation was to infer if present faults interrupt the study areas or not. In addition, dip azimuth information was not available. Therefore, using only apparent dip directions was not sufficient to determine true dip directions (Liner, 2004).

The study areas N1 and N2 were first scrutinized with their related seismic reflectors to capture such fault interruptions. Six different normal faults were interpreted after picking them out in both inline and cross-line directions. Then fault surfaces were created for two of the distinct normal faults above and below N1 and N2 in order to determine their dips and strikes. These two parallel faults were found to be consistent with each other in terms of their strikes. However, their dip directions were completely reverse as inferred from their fault surfaces. The fault surface N1a dips from 5.7 to nearly 7 seconds, while the fault surface N1b is the opposite of N1a, dipping from 7 seconds to lower time scales. Being two major faults around the study areas, they do not really affect study regions based on their far away passes and orientations. This statement can also be confirmed by the consistency of the comparisons between the amplitude interpretations and Gassmann fluid substitution analysis of N1 and N2. Figure 33 illustrates the fault

interpreted time structure map of N1 and N2 with two major fault surfaces (N1a and N1b). On the other hand, there are two converging, arc-shaped, main normal faults which were detected around N3. The irregular time contour shapes in Figure 34 pinpoint the conjunction of these faults on the time structure map of N3.

Apparent dip directions of the faults were interpreted to be nearly in the same direction by their strike orientations and related fault surfaces. Since each fault surface indicates that faults start dipping from 6 to 7.5 seconds similarly, this implies a downward stepping normal fault system. However, these faults are located far away from N3, which means any fault interference within the area of N3 was not observed. Figure 34 shows corresponding fault surfaces and the time structure map of N3.

Lastly, three major normal faults were picked close to areas N4 and N5. They are clearly illustrated on the time structure map in Figure 35. Specifically, two of three faults directly interact with the study regions N4 and N5 by partially or substantially deforming the interested structures. Their fault surfaces shown in Figure 35 suggest that N4a and N4b are oriented parallel to each other, implying close strike directions for the faults. Nevertheless, their apparent dip directions are headed towards each other. N5a displays a dipping beginning from 5.7 to around 7 seconds, whereas the dip direction of the N4b is the reverse of N4a from 7 to 5.7 seconds. They seem to be semi-linear-shaped fracture zones; they are approximately oriented in the same direction as the closing time contours without interrupting them.

a)

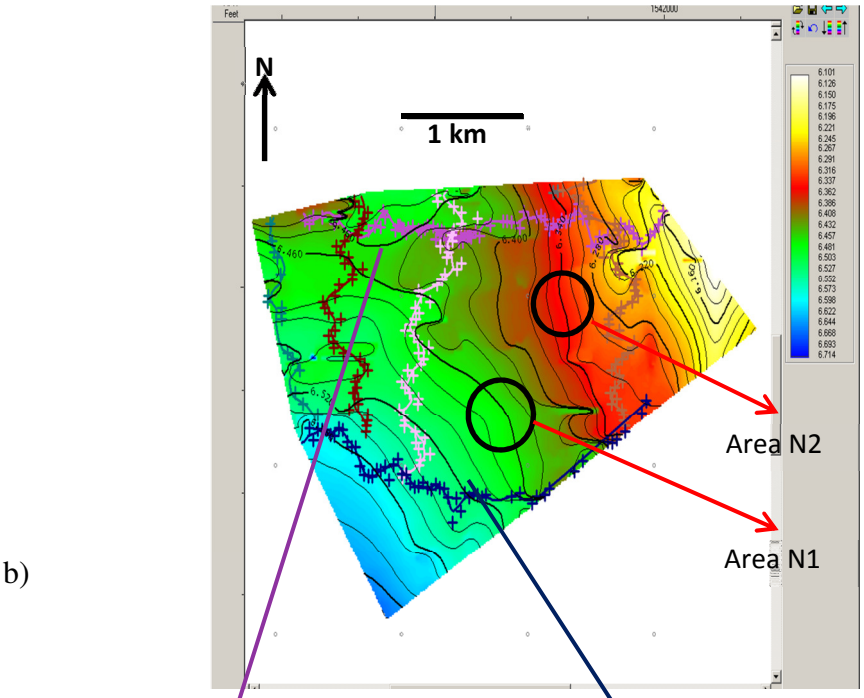

b)

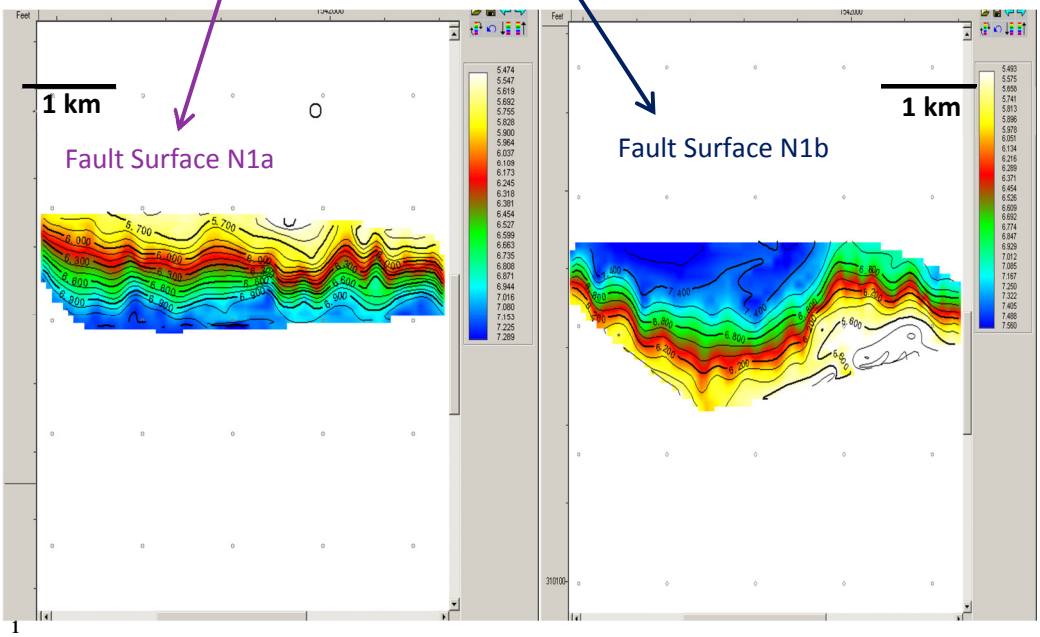

c)

Figure 33. Fault interpretation of N1 and N2. (a) Relative orientations of the faults on the amplitude map of N1 and N2. (b) Corresponding fault surfaces of N1a and (c) N1b

a)

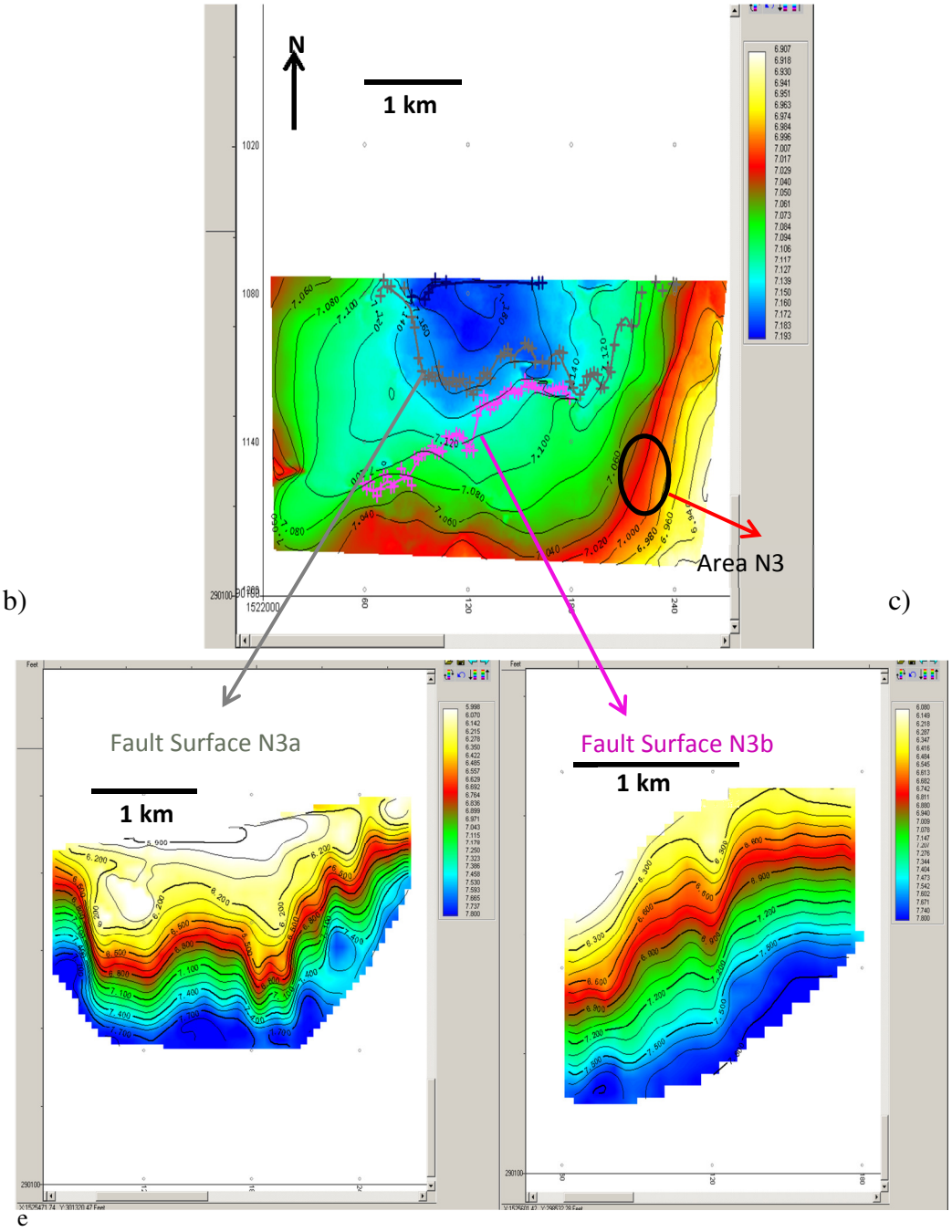

Figure 34. Fault interpretation of N3. (a) Relative orientations of the faults on the amplitude map of N3. (b) Corresponding fault surfaces of N3a and (c) N3b.

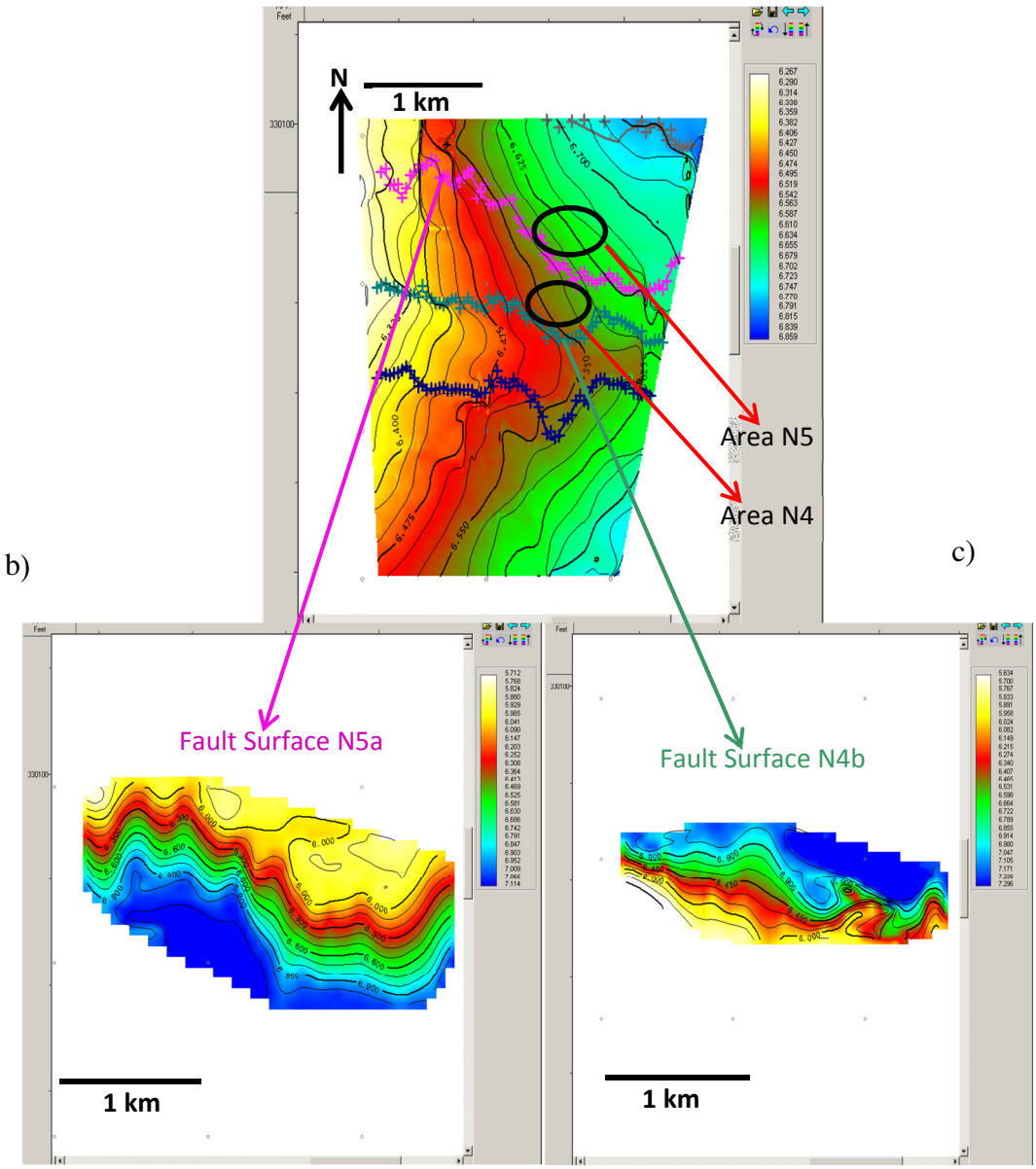

Figure 35. Fault interpretation of N4 and N5. (a) Relative orientations of the faults on the amplitude map of N$ and N5. (b) Corresponding fault surfaces of N5a and (c) N4b.

2.7 Fluid Substitution Analysis of the Study Areas

The fluid substitution characterization of the study areas followed a procedure which was previously applied in the fluid substitution analysis of the Davy Jones reservoir. Each study area is presumed to represent a reservoir-seal formation through their high-negative bright spot anomalies. Reflecting the configuration of the Davy Jones reservoir, a simple imaginary reservoir-seal model was created for each study area. This model consisted of a shale-based seal formation which capped a sandstone reservoir section which was consistently implemented for each study area. Inside the reservoir formation, the gas-filled section was underlain by a brine-saturated feature in the form of contacting separate fluids.

After establishing this imaginary model, the process was to make estimations of gas and brine properties on Matlab software beginning with gas density calculations by assuming the gas was methane for all reservoirs. Initially, the input parameters of the Davy Jones reservoir were utilized in these calculations, as well as those in characterizations of brine properties. Mainly, these parameters include pore pressure, formation temperature, salinity, gas specific gravity of methane, porosity, quartz sandstone mineral bulk, P-wave modulus, and also shale and quartz mineral densities.

Apparently, using all those parameters of the Davy Jones reservoir naturally resulted in the same fluid substitution effects as the Davy Jones. However, calculated brine and gas reflection coefficients of the study areas by means of seismic amplitude interpretations rendered some useful control factors over these input parameters.

Comparison of the reflection coefficients which was obtained through two different methods led to the adjustments of many input parameters, including pore pressures, formation temperatures, stiffness parameters, and dry frame P-wave modulus for the areas. Therefore, specific reservoir responses of each study area were able to be distinguished based on these alterations of input parameters, as long as they were physically meaningful to reflect their own reservoir conditions. This is because varying input parameters eventually result in different fluid substitution responses of the reservoirs.

The implementation of the Reuss bound method for all reservoir conditions helped to validate if the fluid substitution effect of the reservoirs wass probable or not. In particular, the Reuss bound represents the possibly weakest reservoir pore frame and shows the maximum fluid substitution effect of the reservoir fluid by establishing a physical boundary. As discussed in Chapter 2 (Page 22), any reservoir of interest will be in the form of a suspension, and effective pressure implemented on the reservoir could not be compensated under the Reuss bound due to its low or unphysical intrinsic stiffness. For these reasons, fluid substitution effects of the interested areas directly rely upon the estimated reflection coefficient and their balancing power over changing input parameters. Hence, reasonable approximations of reflection coefficients by implementing seismic amplitude interpretations were critical for better characterization of fluid substitution impacts of the reservoirs.

Seismic amplitude interpretation of the study areas also utilized the previously created imaginary reservoir model to compute the reflection coefficient ratio of brine-

and gas-saturated features. However, it was not feasible to calculate individual reflection coefficients of the areas using seismic sections due to unreliable velocity and the lack of the density information of the reservoirs. The only possible approximation was by obtaining their relative ratios instead. This drawback of the seismic amplitude interpretation required estimation of the brine- and gas-saturated impedance ratios of the areas for the comparisons of the fluid substitution effects. In this way, gas-and brine-saturated densities of the reservoirs were able to be used to represent the fluid saturation effects for both seismic amplitude and fluid substitution analysis. For these purposes, the imaginary model of the reservoir seal formation was revisited and we considered that the effects of shale-based seal formation on brine- and gas-saturated reservoir features could be the same. Therefore, shale impedances were able to be normalized and were easily be removed in the calculation of reflection coefficient ratios by eventually leading to the estimations of brine and gas impedance ratios. The following relations illustrate this approach:

$$R_b = \frac{I_b - I_s}{I_b + I_s}, \quad \text{and} \tag{34}$$

$$R_g = \frac{I_g - I_s}{I_g + I_s}. \tag{35}$$

If the shale impedance I_s is isolated in one side of the equation for brine:

$$R_b \times (I_b + I_s) = I_b - I_s, \tag{36 a}$$

$$R_b \times I_b + R_b \times I_s = I_b - I_s, \tag{36 b}$$

$$R_b \times I_s + I_s = I_b - R_b \times I_b, \quad \text{and} \tag{36 c}$$

$$I_s \times (R_b + 1) = I_b \times (1 - R_b). \tag{36 d}$$

And the same process works for the gas case:

$$R_g \times (I_g + I_s) = I_g - I_s, \tag{37 a}$$

$$R_g \times I_g + R_g \times I_s = I_g - I_s, \tag{37 b}$$

$$R_g \times I_s + I_s = I_g - R_g \times I_g, \tag{37 c}$$

$$I_s \times (R_g + 1) = I_g \times (1 - R_g), \quad \text{and} \tag{37 d}$$

$$I_s = \frac{I_b \times (1 - R_b)}{(R_b + 1)}, I_s = \frac{I_g \times (1 - R_g)}{(R_g + 1)}. \tag{38 a}$$

From the equity of relations in regards to the shale impedance, relations take the following form:

$$\frac{I_b \times (1 - R_b)}{(R_b + 1)} = \frac{I_g \times (1 - R_g)}{(R_g + 1)}, \quad \text{and} \tag{38 b}$$

$$\frac{I_b}{I_g} = \frac{(R_b + 1) \times (1 - R_g)}{(1 - R_b) \times (R_g + 1)}, \tag{38 c}$$

where I_s is the shale impedance, I_b and I_g are the brine- and gas-saturated impedances, and R_b and R_g are brine- and gas-saturated reflection coefficients for the study areas, respectively. After determining each impedance ratio of the brine- and gas-saturated regions, saturated velocities were able to be computed by the following equation:

$$\frac{V_b}{V_g} = \frac{I_b}{I_g} \times \frac{\rho_g}{\rho_b}, \tag{39}$$

where V_b and V_g are the brine- and gas-saturated velocities, and ρ_b and ρ_g are the saturated densities of the areas of interest.

Calculations of saturated densities had been achieved through previously implemented input parameters and they were also adjusted during the alterations of the thermodynamic and compositional parameters which relied upon the comparison of seismically obtained reflection coefficients. In this sense, saturated reservoir densities reflect the actual saturated density responses of the study areas under the effects of changing pressure, temperature, and stiffness parameters, etc.

Gas-and brine-saturated impedances, reflection coefficients, velocities, P-wave moduli, and other elastic parameters of the study regions were specified based on the mutual interactions of seismic interpretation, fluid substitution analysis and modified input parameters. However, Reuss bounds of brine- and gas-saturated P-wave moduli provided the lowest physical limits for the stiffness of the saturated reservoir features by defining the boundaries of feasible lowest saturated P-wave moduli. In this sense, the creation of related Reuss bounds involved applications of Davy Jones input parameters

and the modified parameters of the study areas. Firstly, the brine fluid effect was represented by substituting the dry frame P-wave modulus $M_{dry} = 0$ into the related Gassmann-oriented, saturated P-wave moduli equations with varying porosity. Under this assumption, the brine saturation effect was plotted with changing fractional porosity from 0 to 100 percent, leading to a curve to be formed. This curve essentially defined the Reuss bound of brine-saturated P-wave moduli of the Davy Jones reservoir. That is, any brine-saturation effect on the study regions cannot be theoretically represented under this curve.

Correspondingly, gas saturation effects were characterized with changing porosity values by following the same procedure as in the brine case. This simply results in another curve defining the Reuss bound of gas-saturated P-wave moduli for the reservoir. Similarly, gas saturation effects on the study areas could not be lower than this boundary. Afterwards, the brine-saturated P-wave modulus of the Davy Jones at 20 % porosity was marked as a point on the plot. Then a straight line was drawn from the axis of $M = M_o$ to this point and it intersected with the previously plotted Reuss bound of the brine-saturated P-wave moduli at the porosity of 35%, which is termed intercept (φ_R) porosity.

Subsequently, the coherent gas-saturated P-wave modulus was estimated by moving vertically down on the intercept porosity. The following step was to draw another straight line back from this gas-saturated P wave modulus at 35 % porosity toward the axis of $M = M_o$ pinpointing the gas-saturated P-wave modulus of the reservoir at 20 % porosity. Figure 36 demonstrates this plot of the Reuss bounds and changes in P-wave

modulus at both the intercept and the original reservoir porosities. Then, saturated P-wave moduli of the study regions were represented on the Reuss bound plot of the Davy Jones reservoir in order to observe and to evaluate their consistencies. Figure 39 illustrates the P-wave modulus response of the study areas at 20% original porosity in conjunction with those of Davy Jones.

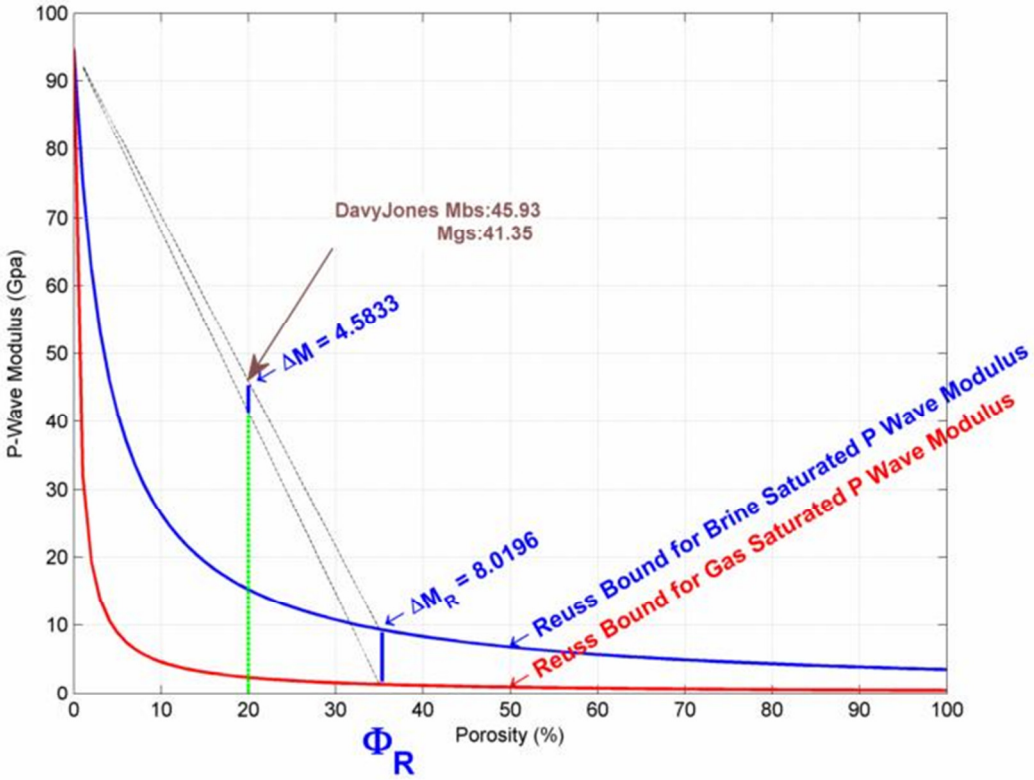

Figure 36. Brine- and gas-saturated P-wave moduli changes of Davy Jones relied on its brine- and gas-saturated Reuss bounds. Mbs is brine-saturated bulk modulus, Mgs is gas saturated bulk modulus, ΔM is the difference between brine- and gas-saturated bulk modulus at original porosity, while ΔM_R is the difference for Reuss average brine- and gas-saturated bulk moduli at critical porosity.

2.8 AVO Analysis of the Study Areas

All study areas, including the Davy Jones reservoir were examined based on their AVO responses. Even though, AVO analysis of the areas is not the primary objective of this study, it might be indicative of gas effect. Due to this perspective, three different conceptional models were created for all study regions. One of the models assumed that gas-saturated sands overlay brine-saturated sands in a reservoir feature. In the second model, gas sands were encased by a shale-based seal; the third model simply replaced the gas sands in the second model with brine sands. The intention of preparing three different models was to observe related changes from all possible perspectives that could occur in general reservoir-seal conditions.

Specifically, first model was designed to show feasible amplitude deviations from the brine-filled background section and it sought the decay of amplitudes trending toward a negative normal-incident reflection coefficient region through gas effect. The other two models were planned to demonstrate the type of AVO response based on general AVO classifications; they search for consistency of the bright spot gas effect to validate the findings of previously implemented methods. In order to obtain AVO responses from each study area, brine- and gas-saturated P- and S- wave velocities and densities were utilized. Brine- and gas-saturated P-wave velocities and densities of the regions had been previously computed via Gassmann fluid substitution analysis. Then, brine- and gas-saturated S-wave velocities were approximated by using Castagna's 1993 relation, shown in Equation 1. The use of second and third conceptional models made it necessary to obtain shale P- and S-wave velocities as well as shale densities for each study area. This

was accomplished by utilizing the shale P-wave velocity and density trends of the northern Gulf of Mexico which are proposed by Hilterman (2011) and were shown in Figure 16. Based on the time and depth ranges of each study area, these shale density and velocity trends of the Gulf of Mexico were extrapolated to depths of interest. After determining P-wave shale velocities for each region, S-wave velocities were calculated from Equation 1. All these P- and S-wave shale velocities and densities were shown in Table 8. Computation of AVO responses directly rely on the approach of the exact solution of the Knott-Zoeppritz equations. The Crewes -Zoeppritz Explorer software using the exact solution method was employed to evaluate amplitude changes with offset depending on incident P-wave reflection. Being angle stack seismic data, near offset angles range between 0 to 18 degrees and far offset is between 18 and 30 degrees. Therefore, changes in angular reflection coefficients and amplitudes are limited to these near and far offset angles of the seismic data set. Table 3 and Figure 37 showed the criteria to distinguish AVO responses.

Table 3. Top gas sand impedance, reflection coefficient and offset dependent characteristics of four different AVO classes (Castagna, 1998).

Class	Relative impedance	Quadrant	*A*	*B*	Remarks
I	Higher than overlying unit	IV	+	−	Reflection coefficient (and magnitude) decrease with increasing offset
II	About the same as the overlying unit	III or IV	±	−	Reflection magnitude may increase or decrease with offset, and may reverse polarity
III	Lower than overlying unit	III	−	−	Reflection magnitude increases with offset
IV	Lower than overlying unit	II	−	+	Reflection magnitude decreases with offset

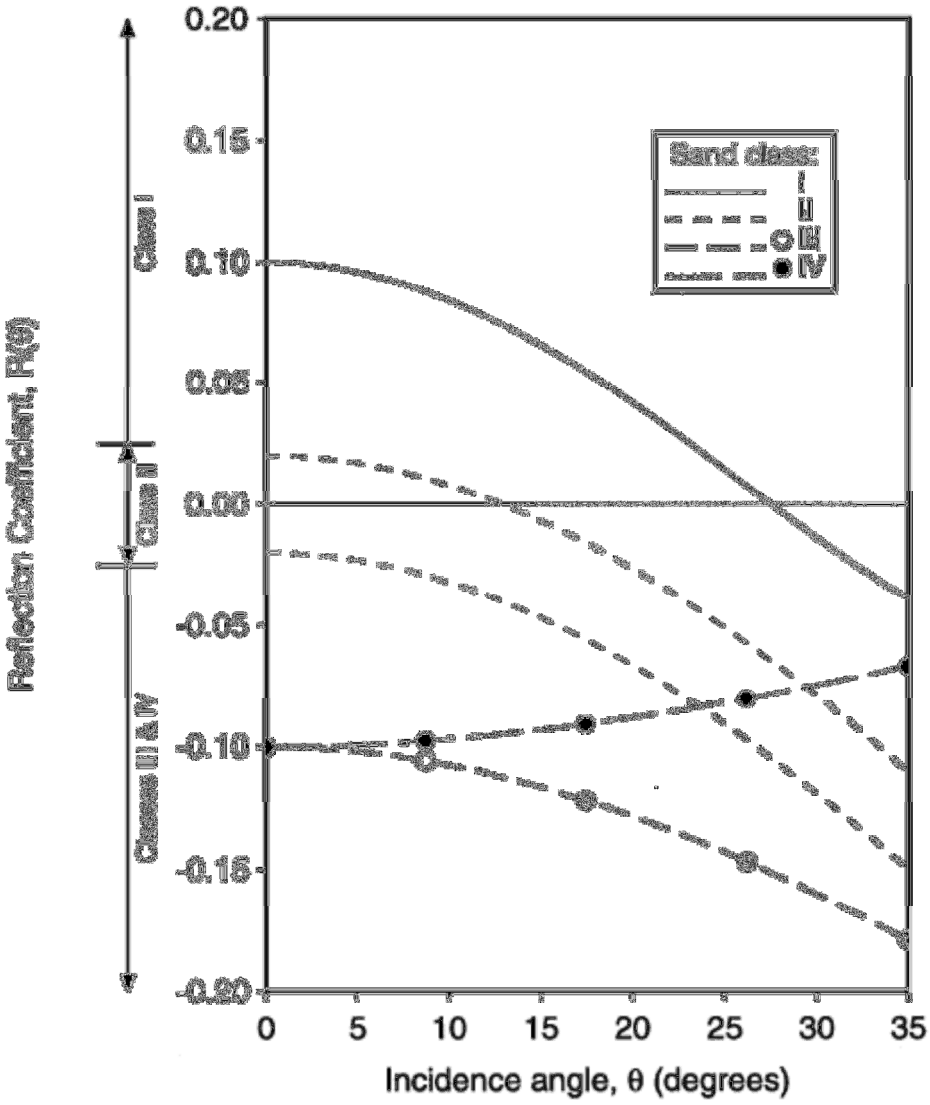

Figure 37. A classification of four main types of AVO responses (Castagna, 1998).

Chapter 3. Results

Fluid substitution analysis of the Davy Jones reservoir revealed some invaluable information to indicate what the study areas of the Vermillion area would represent in terms of their bright spots and fluid substitution responses. In this sense, individual gas- and brine-saturation effects on the reservoir frame of Davy Jones were characterized by considering its reservoir conditions. This made it possible to monitor responses of the reservoir frame caused by each saturating fluid. In other words, these interplays of Davy Jones reservoir and the fluids are reflected by their brine- and gas-saturated P-wave moduli, velocities, impedances, reflection coefficients, and related elastic parameters; these were shown in Table 4. Each of these factors can be considered as an indicator of what the reservoir physically underwent through fluid substitution processes.

The Davy Jones reservoir parameters set a range of physical criteria which are responsible for the fluid substitution results of the study areas from Vermilion area. Therefore, the results of the Davy Jones fluid substitution task are not only important to interpret its reservoir conditions but also are critical to judge the validity of the bright spot responses of each study area in the Vermilion. The fluid substitution results suggest that the Davy Jones reservoir is identified with a reflectivity of 0.045 at water-gas contact. Correspondingly, brine and gas sand velocities are about 4379 and 4234 m/s, whereas brine- and gas-saturated densities are approximately 2.31 and 2.19 g/cc, respectively. These velocities are the products of brine- and gas-saturated P-wave moduli of the reservoir at around 44.3 and 39 Gpa. From another point of view, calculated brine- and gas-saturated Reuss bounds of the reservoir also confirm the validity of these results.

Brine- and gas-saturated P wave moduli of the reservoir are estimated to be 45.9 and 41.4 Gpa respectively from the Reuss bounds at original porosity of 20 % and intercept porosity of 35%. This led to the difference of 4.5 Gpa among the P-wave moduli of the brine- and gas-saturated reservoir shown in Figure 38. These combined results of the Davy Jones reservoir were used to interpret the feasibility of fluid substitution and Reuss bound responses caused by each study area of the Vermilion.

In this study, the study regions N1, N2, and N3 demonstrated acceptable brine- and gas-saturated velocities, densities, reflection coefficients, P-wave moduli and elastic parameters . However the study regions N4 and N5 did not; they are based on their fluid substitution and Reuss bound examinations in comparison to those of Davy Jones. The area N1 has brine- and gas-saturated velocities of 3512 and 2995m/s, while its saturated densities are estimated to be the same as those of Davy Jones as was shown in Table 4. This unity of densities among two different regions is a result of the preserved pressure and temperature values of the Davy Jones reservoir within the area N1. Velocity discrepancies of two regions seem to be caused by the specific compositional environment of N1 rather than its environmental conditions.

The computed brine and gas saturated velocities of N1 correspond to brine- and gas-saturated P-wave moduli at 28.5 and 19.6 Gpa respectively shown in Table 5. This caused the reflectivity of 0.1 at imaginary water-gas contact for N1. This relative reflectivity value is far above what Davy Jones causes. Therefore, this implies a stronger bright spot effect of N1. Coherently, the area N2 resulted in brine- and gas-saturated velocities of 3462 and 3000 m/s, respectively, under varying saturated densities, and P-

wave moduli in comparison to those of Davy Jones shown in Table 6. Brine- and gas-saturated densities of N2 are around 2.31 and 2.18 g/cc, while their saturated P-wave moduli are about 27.7 and 19.7 Gpa in turn. What slightly changed the saturated densities of N2 are varying pore pressure and formation temperature values which were valid under the numbers of Davy Jones. However, anomalous saturated P-wave moduli differences between N2 and Davy Jones might primarily be attributed to the particular geologic and compositional environment of N2.

In spite of such high differences of P-wave moduli among these regions, saturated velocities of N2 seem reasonable, considering the compositional discrepancies of the areas. The last successful bright spot indicator among the study areas is N3. The area N3 demonstrates a more distinct reflectivity, which is slightly over 0.1 at water-gas contact and exceeds the reflectivity of N1 and N2. Inherently, its brine- and gas-saturated P-wave moduli were estimated to be 41.5 and 20.4 Gpa, respectively, whereas brine- and gas-saturated densities remained nearly same as the other regions shown in Table 7.

Presumably, the high P-wave moduli difference of N3 caused the very distinctive brine- and gas-saturated velocities which were verified at 4237 m/s for brine and 3047 m/s in the gas case. This explains the high reflectivity of N3 compared to the other study areas. As can be seen from Table 7, brine, water, and gas velocities with their bulk moduli were also augmented as a result of increasing pore pressure and formation temperature effects in comparison to those of the other study regions. Most of the changes were undergone by the brine properties of N3 rather than its gas components.

From a different perspective, the Reuss bounds of the areas N1, N2, and N3 concluded in similar responses thereby supporting fluid substitution results for the areas. In this manner, brine- and gas-saturated P-wave moduli responses of these regions corresponded to acceptable ranges of saturated P-wave moduli changes on the combined Reuss representations of the areas and Davy Jones. Being a more appropriate benchmark, dry frame and mineral P-wave moduli of Davy Jones with known P-wave moduli of each fluid were used to form these bounds and then related responses of other study areas were adapted to these boundaries of the Davy Jones reservoir.

Brine- and gas-saturated P-wave moduli of the areas N1, N2, and N3 were represented above these bounds by implying their suitability with the saturated P-wave moduli ranges of the Davy Jones reservoir, as was shown in Figure 39. Furthermore, these areas were interpreted to be fairly convenient to accommodate related effective pressure changes on their pore frames based on those of Davy Jones. On the other hand, the areas N4 and N5 failed to show amenable bright spot responses in agreement with their results of fluid substitution analysis and Reuss bound examinations. The fluid substitution analysis of the area N4 illustrates that brine- and gas-saturated velocities, impedances, reflection coefficients, P-wave moduli and elastic parameters are physically inacceptable to form amplitude bright spot anomalies. Brine- and gas-saturated P wave moduli of N4 are around 15.1 and 1.84 Gpa, respectively, while its brine- and gas-saturated densities are close to those of Davy Jones under varying pore pressure and formation temperatures given in Table 9.

Correspondingly, N4 had brine- and gas-saturated velocities of 2554 and 919 m/s. The brine- and gas-saturated velocities of N4 did not really reflect the impact of pore frame during fluid substitutions. This implies that pore frames of N4 cannot efficiently tolerate implemented overburden pressure along its pore spaces. Likewise, the negative valued dry frame P-wave and other elastic moduli of N4 support this inference from the fact that the dry frame P-wave, bulk and shear moduli cannot physically have values under zero. In addition, the adjusted stiffness parameters of N4 were notably high around 5.5. This is another reason why the fluid substitution analysis of N4 generates unrealistic results associated with its elastic parameters.

The fluid substitution analysis of the area N5 indicates the ineffectiveness of its bright spot anomaly, almost identical to N4. In this sense, the brine- and gas-saturated P-wave moduli of N5 are about 22 and 1.85 Gpa, respectively, whereas its saturated densities remain unchanged, as shown in Table 10. Together they yielded a brine-saturated velocity of 3078 m/s, while its gas-saturated velocity was found to be around 907 m/s. Another point regarding the velocities is that brine and water velocities dramatically increased during brine substitution, unlike the velocities of other study areas. This might be attributed to increasing the pore pressure and formation temperature of N5. Even though N5 demonstrated high reflectivity which was around 0.55 at the imaginary water-gas contact, this is a false bright spot indication, as it can be anticipated from the negative dry frame P-wave and other elastic moduli, given in Table 10. Furthermore, the modified stiffness parameters of N5 are impractically high, at about 5.5 by pointing out the inadequateness of N5 as a bright spot indicator.

Table 4. Reservoir parameters of Davy Jones before and after fluid substitution.

Davy Jones Reservoir Parameters During Fluid Substitutions		**Davy Jones Reservoir Parameters After Fluid Substitutions**		
Pore Pressure (Mpa)	**186.2 (27000 psi)**	**V_b and V_g Brine water and gas velocities respectively (m/s)**	**918**	**368**
Formation Temperature (C^o)	**226.7 (440 F^o)**	**V_{bsat} and V_{gsat} Brine and gas saturated P wave velocities (m/s)**	**4379**	**4234**
Porosity (%)	**20**	**I_{bsat} and I_{gsat} Brine and gas saturated impedances**	**10122**	**9259**
Salinity (ppm)	**50000**	**R_{gsat} /R_{bsat} Ratios of Brine and gas saturated reflection coefficients**	**1.34**	
Depth (m)	**8573 (28125 feet)**	**M_{bsat} and M_{gsat}Brine and gas saturated P wave moduli (Gpa)**	**44.3**	**39**
K_o quartz mineral bulk Modulus (Gpa)	**38**	**M_d and M_o Dry and mineral P wave moduli (Gpa)**	**38.3**	**97**
G_o quartz mineral shear Modulus (Gpa)	**44.3**	**K_d and G_d Dry bulk and shear moduli (Gpa)**	**17.5**	**17.2**
ρ_m quartz mineral density (g/cc)	**2.65**	**ρ_b and ρ_g Brine and gas densities (g/cc)**	**0.96**	**0.33**
R molar gas contant (joule)	**8.3144**	**ρ_{bsat} and ρ_{gsat} Brine and gas saturated densities (g/cc)**	**2.31**	**2.18**
G (gas specific gravity for methane)	**0.56**	**V_w water velocity (m/s)**	**908**	
Stiffness Parameter "A" for K_d	**3.39**	**K_b Brine bulk modulus (Gpa)**	**3.5**	
Stiffness Parameter "B" for G_d	**3.48**	**K_g Gas bulk modulus (Gpa)**	**0.48**	

Table 5. Reservoir parameters of N1 before and after fluid substitution.

Reservoir Parameters for Study Area N1 During Fluid Substitutions		**Reservoir Parameters for Study Area N1 After Fluid Substitutions**		
Pore Pressure (Mpa)	**186.2 (27000 psi)**	**V_b and V_g Brine water and gas velocities respectively (m/s)**	**918**	**368**
Formation Temperature (C^o)	**226.7 (440 F^o)**	**V_{bsat} and V_{gsat} Brine and gas saturated P wave velocities (m/s)**	**3512**	**2995**
Porosity (%)	**20**	**I_{bsat} and I_{gsat} Brine and gas saturated impedances**	**8119**	**6549**
Salinity (ppm)	**50000**	**R_{gsat} /R_{bsat} Ratios of Brine and gas saturated reflection coefficients**	**1.23**	
Two Way Travel Time (s)	**6.5**	**M_{bsat} and M_{gsat}Brine and gas saturated P wave moduli (Gpa)**	**28.5**	**19.6**
K_o quartz mineral bulk Modulus (Gpa)	**38**	**M_d and M_o Dry and mineral P wave moduli (Gpa)**	**18**	**97**
G_o quartz mineral shear Modulus (Gpa)	**44.3**	**K_d and G_d Dry bulk and shear moduli (Gpa)**	**6.84**	**8.39**
ρ_m quartz mineral density (g/cc)	**2.65**	**ρ_b and ρ_g Brine and gas densities (g/cc)**	**0.96**	**0.33**
R molar gas contant (joule)	**8.3144**	**ρ_{bsat} and ρ_{gsat} Brine and gas saturated densities (g/cc)**	**2.31**	**2.18**
G (gas specific gravity for methane)	**0.56**	**V_w water velocity (m/s)**	**908**	
Stiffness Parameter "A" for K_d	**4.49**	**K_b Brine bulk modulus (Gpa)**	**3.5**	
Stiffness Parameter "B" for G_d	**4.49**	**K_g Gas bulk modulus (Gpa)**	**0.48**	

Table 6. Reservoir parameters of N2 before and after fluid substitution.

Reservoir Parameters for Study Area N2 During Fluid Substitutions		**Reservoir Parameters for Study Area N2 After Fluid Substitutions**		
Pore Pressure (Mpa)	**179.2**	**V_b and V_g Brine water and gas velocities respectively (m/s)**	**843**	**360**
Formation Temperature (C^o)	**218.7**	**V_{bsat} and V_{gsat} Brine and gas saturated P wave velocities (m/s)**	**3462**	**3005**
Porosity (%)	**20**	**I_{bsat} and I_{gsat} Brine and gas saturated impedances**	**8005**	**6570**
Salinity (ppm)	**50000**	**R_{gsat} /R_{bsat} Ratios of Brine and gas saturated reflection coefficients**	**1.23**	
Two Way Travel Time (s)	**6.4**	**M_{bsat} and M_{gsat}Brine and gas saturated P wave moduli (Gpa)**	**27.7**	**19.7**
K_o quartz mineral bulk Modulus (Gpa)	**38**	**M_d and M_o Dry and mineral P wave moduli (Gpa)**	**18.2**	**97**
G_o quartz mineral shear Modulus (Gpa)	**44.3**	**K_d and G_d Dry bulk and shear moduli (Gpa)**	**6.9**	**8.48**
ρ_m quartz mineral density (g/cc)	**2.65**	**ρ_b and ρ_g Brine and gas densities (g/cc)**	**0.96**	**0.33**
R molar gas contant (joule)	**8.3144**	**ρ_{bsat} and ρ_{gsat} Brine and gas saturated densities (g/cc)**	**2.32**	**2.19**
G (gas specific gravity for methane)	**0.56**	**V_w water velocity (m/s)**	**835**	
Stiffness Parameter "A" for K_d	**4.48**	**K_b Brine bulk modulus (Gpa)**	**3.16**	
Stiffness Parameter "B" for G_d	**4.48**	**K_g Gas bulk modulus (Gpa)**	**0.46**	

Table 7. Reservoir parameters of N3 before and after fluid substitution.

Reservoir Parameters for Study Area N3 During Fluid Substitutions		**Reservoir Parameters for Study Area N3 After Fluid Substitutions**		
Pore Pressure (Mpa)	**235.3**	**V_b and V_g Brine water and gas velocities respectively (m/s)**	**1599**	**419**
Formation Temperature (C^o)	**235.7**	**V_{bsat} and V_{gsat} Brine and gas saturated P wave velocities (m/s)**	**4237**	**3047**
Porosity (%)	**20**	**I_{bsat} and I_{gsat} Brine and gas saturated impedances**	**8119**	**6549**
Salinity (ppm)	**50000**	**R_{gsat} /R_{bsat} Ratios of Brine and gas saturated reflection coefficients**	**1.31**	
Two Way Travel Time (s)	**7**	**M_{bsat} and M_{gsat}Brine and gas saturated P wave moduli (Gpa)**	**41.5**	**20.4**
K_o quartz mineral bulk Modulus (Gpa)	**38**	**M_d and M_o Dry and mineral P wave moduli (Gpa)**	**18.2**	**97**
G_o quartz mineral shear Modulus (Gpa)	**44.3**	**K_d and G_d Dry bulk and shear moduli (Gpa)**	**6.84**	**8.49**
ρ_m quartz mineral density (g/cc)	**2.65**	**ρ_b and ρ_g Brine and gas densities (g/cc)**	**0.97**	**0.35**
R molar gas contant (joule)	**8.3144**	**ρ_{bsat} and ρ_{gsat} Brine and gas saturated densities (g/cc)**	**2.32**	**2.19**
G (gas specific gravity for methane)	**0.56**	**V_w water velocity (m/s)**	**1596**	
Stiffness Parameter "A" for K_d	**4.49**	**K_b Brine bulk modulus (Gpa)**	**9.1**	
Stiffness Parameter "B" for G_d	**4.48**	**K_g Gas bulk modulus (Gpa)**	**0.67**	

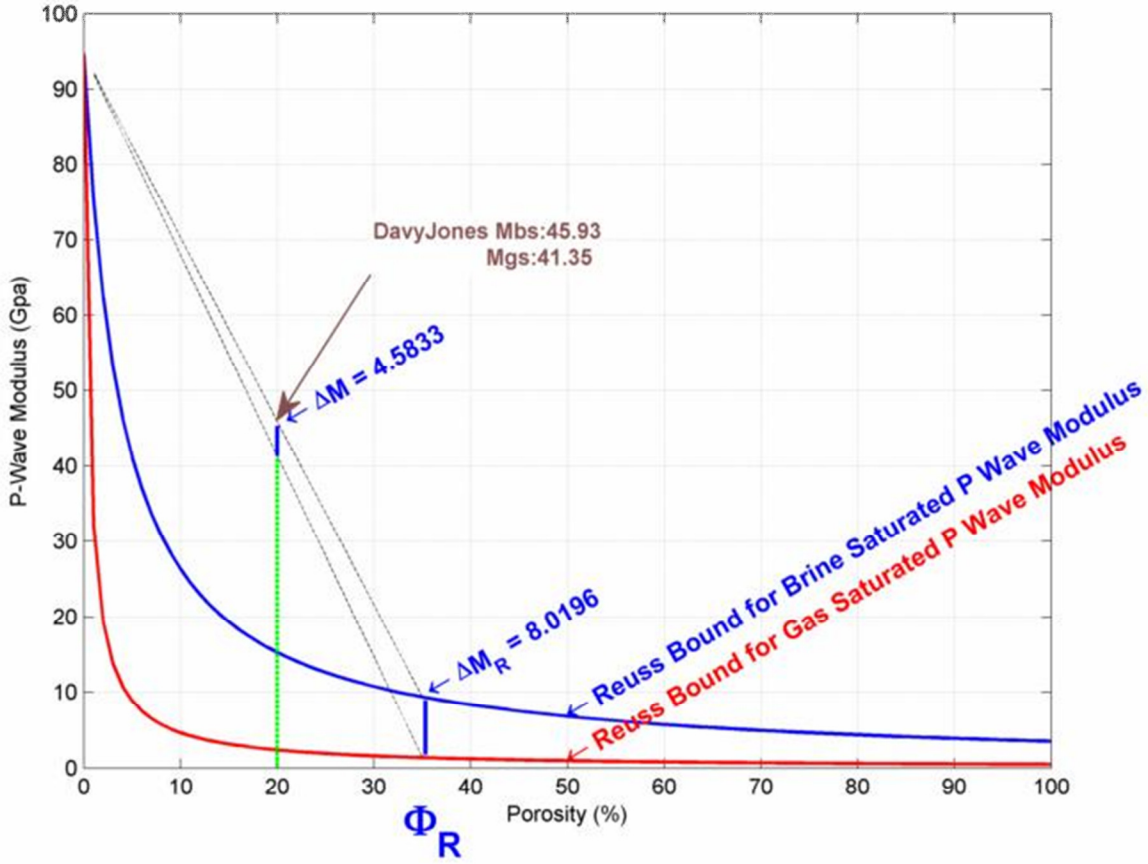

Figure 38. Brine- and gas-saturated P-wave moduli changes of Davy Jones relied on its brine- and gas-saturated Reuss bounds.

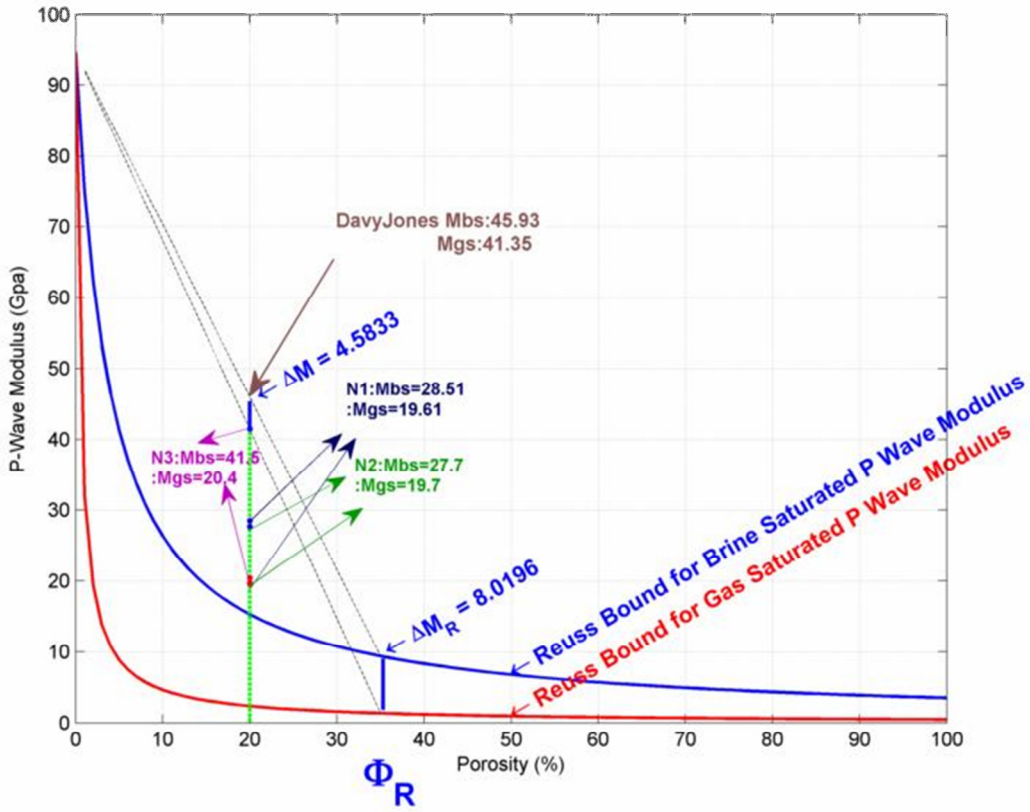

Figure 39. Brine- and gas-saturated P-wave moduli changes of N1, N2, and N3 relied on the brine- and gas-saturated Reuss bounds of Davy Jones reservoir.

On the other hand, Reuss bound representations of the areas N4 and N5 are almost in perfect agreement with the results of fluid substitution. Brine- and gas-saturated P-wave moduli of N4 cannot exceed the created brine and gas Reuss bounds of the Davy

Jones reservoir, which were shown in Figure 39. Thus, the reservoir frame of N4 can be considered to be highly weak or nearly in the form of a solution to show proper reservoir properties in both the brine and gas cases. Although, the brine-saturated P-wave modulus of N5 is located slightly above the brine Reuss bound of the Davy Jones reservoir, its gas-saturated P-wave modulus is far below the gas Reuss bound based on Davy Jones in the same figure.

In this study, the relative positions of both the brine- and gas-saturated P-wave moduli of N5 on the Reuss representations suggest that pore frames of N5 show little or no intrinsic stiffness to overcome any applied pore or lithostatic pressure under its specific environmental conditions. Consequently, the combined results of fluid substitution analysis and Reuss bound examinations support the claim that study areas N1, N2 and N3 can successfully be distinguished with their suitable bright spot responses, whereas the areas N4 and N5 generate false bright spot indications by causing unresponsive or unnatural fluid substitution effects. Based on the AVO examination results of each study area, it can be asserted that Davy Jones and three of five study areas (N1, N2, and N3) consistently demonstrate decay of amplitudes with offset, whereas study areas N4 and N5 cause physically inadequate variations of amplitudes with offset.

The AVO response of the Davy Jones reservoir based upon the gas and brine sand model suggests that normal incident reflection coefficient decreases by trending from the positive to the negative normal incident reflection coefficient region (see Figure 40). This might be attributed to the effect of low impedance gas sands compared with the higher impedance of the brine-filled background section. This type of deviation of amplitudes

and reflection coefficient are generally caused by gas-bearing lithologies (Castagna, 1997).

On the other hand, the AVO response of the Davy Jones reservoir formed by the second model (Figure 46a) corresponds to the low impedance gas sands compared with the impedance of the shale-based seal. This might be indicative of the gas bright spot effect which is termed the Class-IV (see Figure 37 and Table 3) AVO response (Castagna, 1998). Similarly, the AVO effect of Davy Jones based on the third model demonstrates that the normal incident reflection coefficient of brine-filled reservoir section decreases with offset. However, the rate of change in the reflection coefficient is not as large as it is in the gas sand case. This is also typical behavior of a Class-IV AVO response (Figure 46b). As it can be seen inFigures 41,42, and 43 , AVO responses of the areas N1, N2, and N3 based on first model are nearly identical to that of the Davy Jones reservooir. Their gas sand reflection coefficients trend toward the negative normal incidence reflection coefficient region, implying the gas effect on amplitudes. Furthermore, their AVO responses using second and third models (Figures 47, 48,and 49) might be indicative of gas bright spots. They correspond to the same Class-IV AVO effect as Davy Jones demonstrated.

The AVO responses of the areas N4 and N5 (Figures 44 and 45) based on the first model resulted in inconsistent changes of normal incident reflection coefficients. Because they do not physically correspond to any known AVO effect. Their inadequateness is caused by their low P- and S-wave velocities, as the fluid substitution results suggested.

Therefore, their AVO effects utilizing the second and third model were not included here, due to their nonsense responses.

Table 8. Calculated P and S wave velocities and densities for shale and sand formations

Areas of Interest	**N1**	**N2**	**N3**	**N4**	**N5**	**Davy Jones**
Shale Densities (g/cc)	2.48	2.48	2.50	2.48	2.49	2.48
Shale P Wave Velocities (m/s)	4420	4389	4556	4412	4504	4420
Shale S Wave Velocities (m/s)	2637	2611	2755	2631	2711	2637
Brine Saturated Sand Densities (g/cc)	2.31	2.32	2.32	2.32	2.32	2.31
Gas Saturated Sand Densities (g/cc)	2.18	2.19	2.19	2.19	2.19	2.18
Brine Saturated P Wave Sand Velocities (m/s)	3512	3462	4237	2554	3078	4379
Gas Saturated P Wave Sand Velocities (m/s)	2995	3005	3047	919	907	4234
Brine Saturated S Wave Sand Velocities (m/s)	1855	1812	2480	1029	1481	2602
Gas Saturated S Wave Sand Velocities (m/s)	1409	1418	1454	389	380	2477

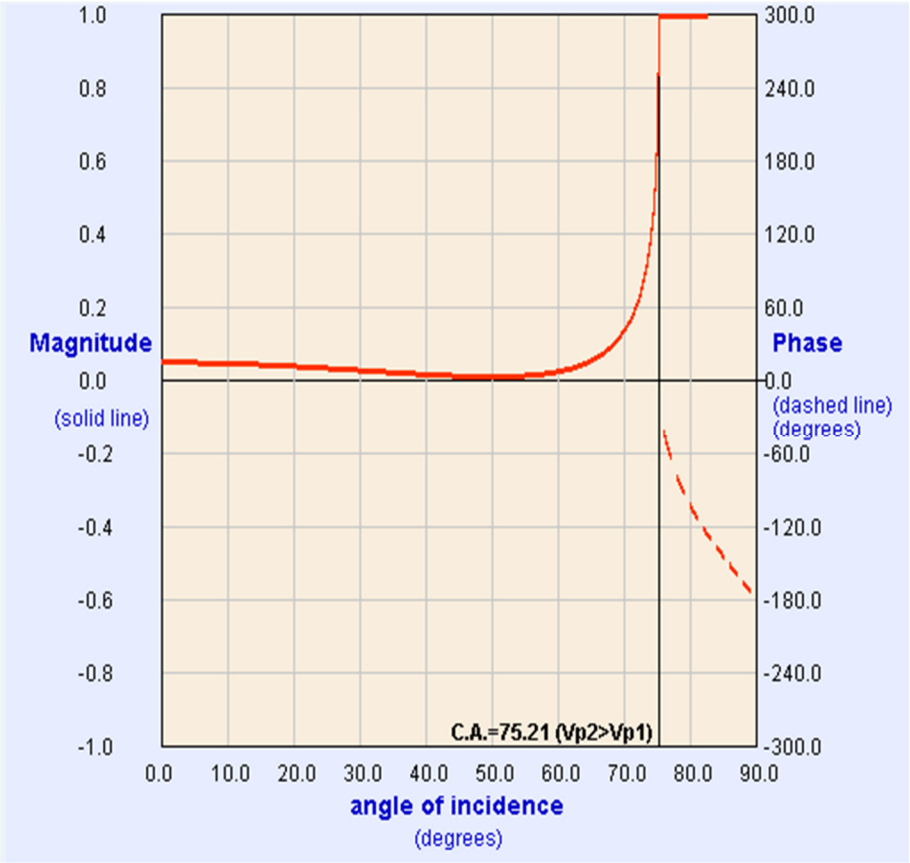

Figure 40. AVO response of the Davy Jones reservoir based on a gas and brine sand reservoir model. (Left vertical axis is normal incident reflection coefficient, horizontal axis is angle of incidence in degrees, and right vertical axis is the phase in degrees).

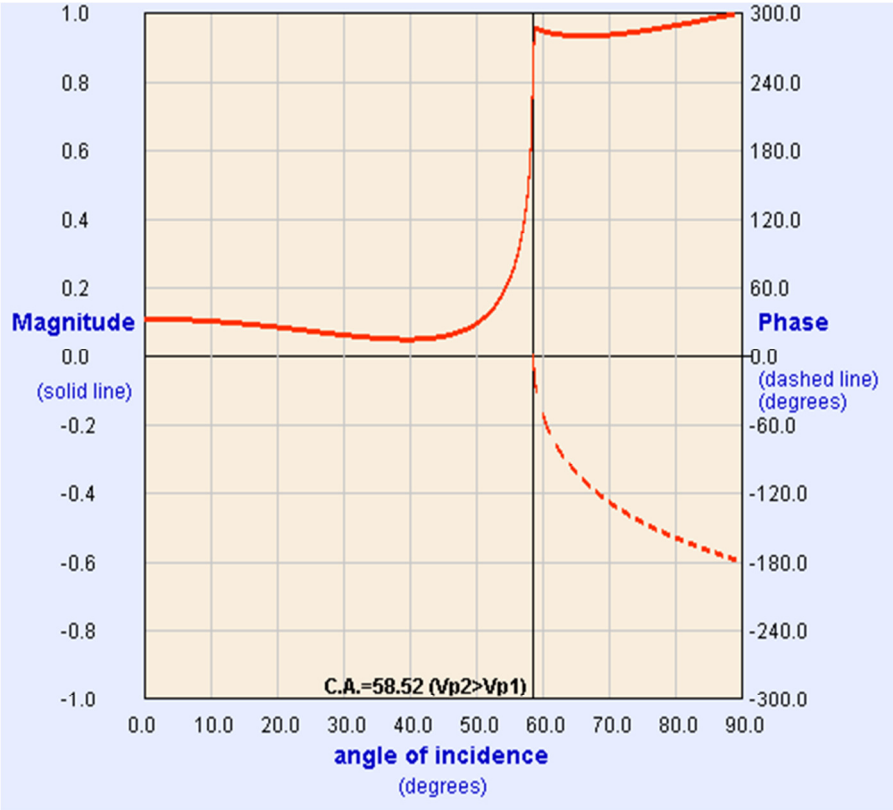

Figure 41. AVO response of N1 based on a gas and brine sand model

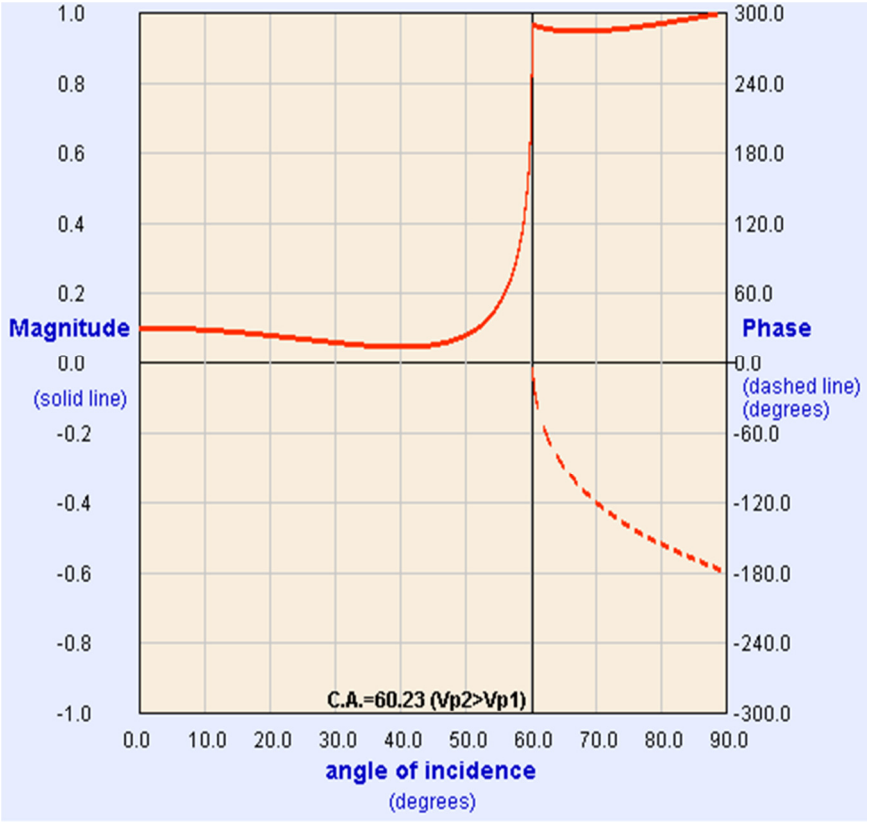

Figure 42. AVO response of N2 based on a gas and brine sand model

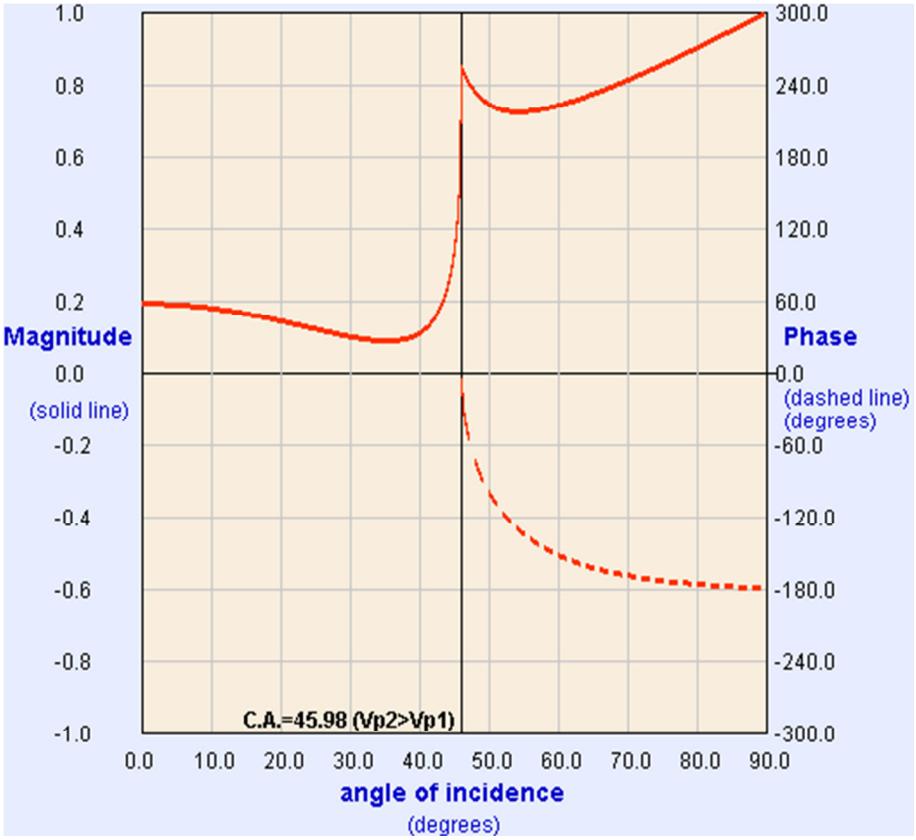

Figure 43. AVO response of N3 based on a gas and brine sand model

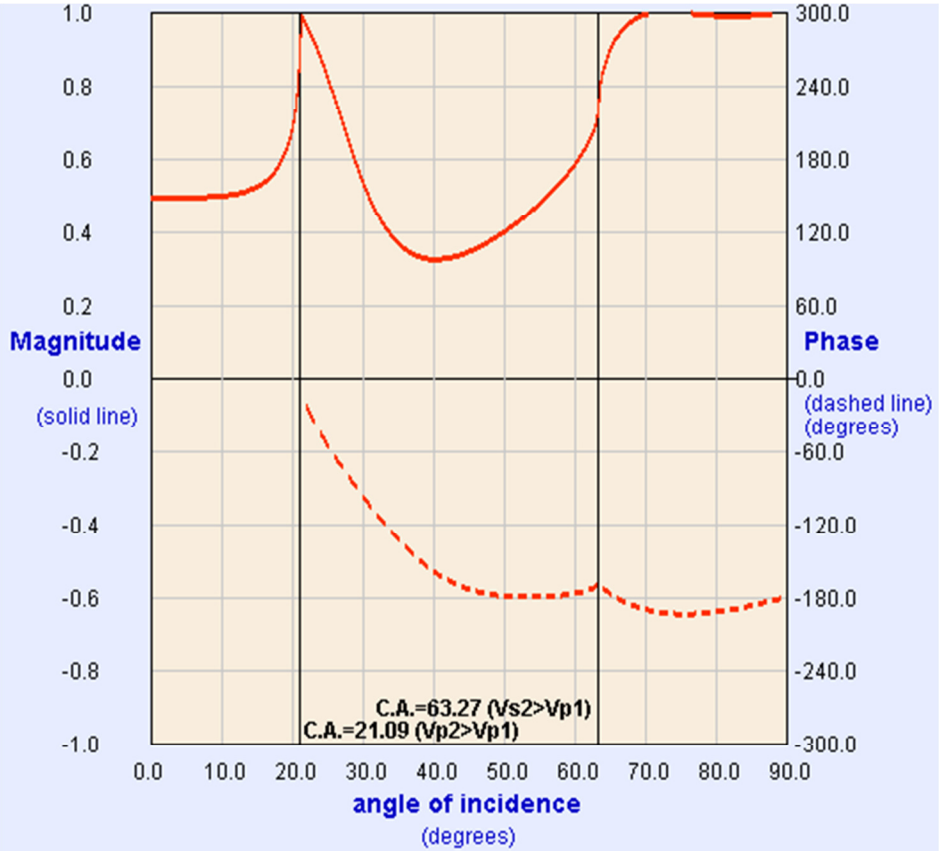

Figure 44. AVO response of N4 based on a gas and brine sand model

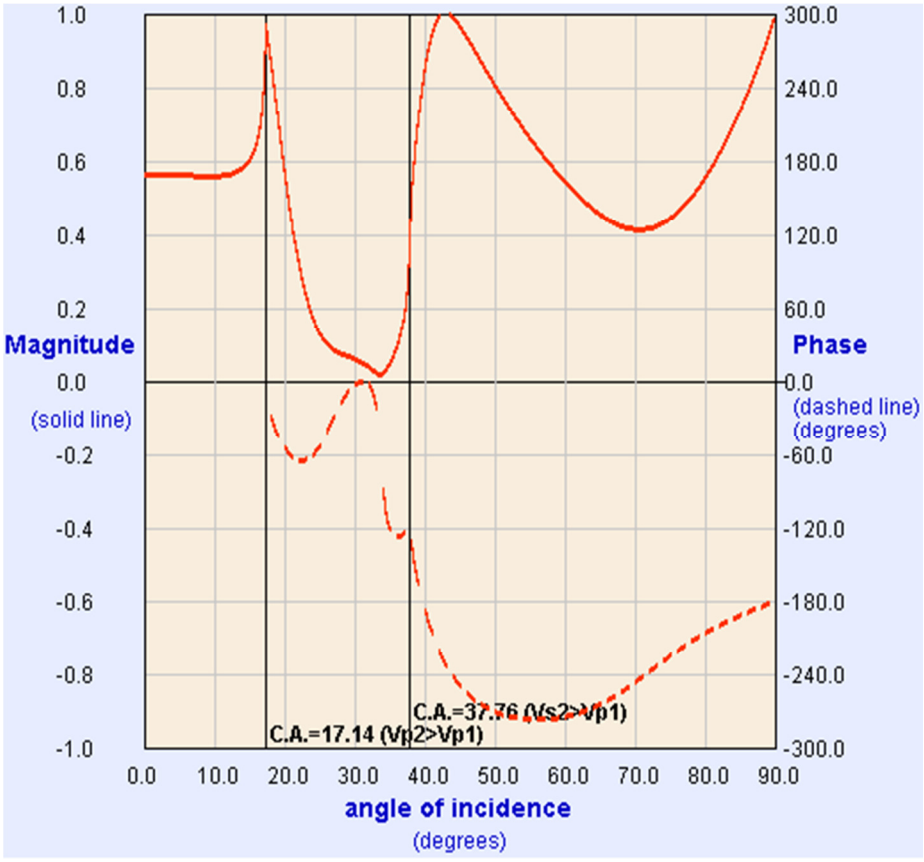

Figure 45. AVO response of N5 based on a gas and brine sand model

a)

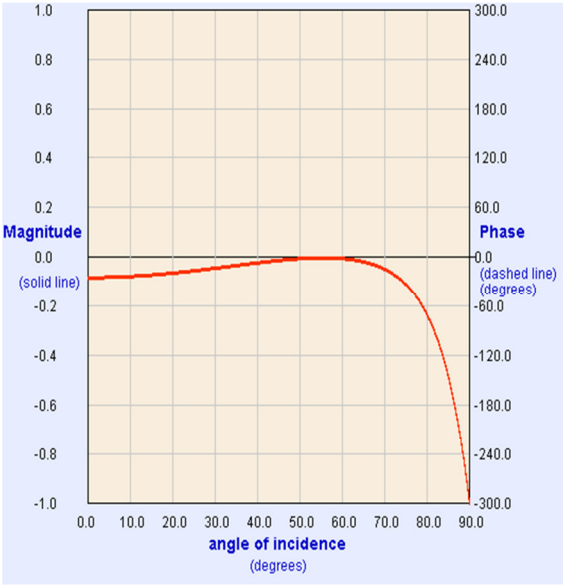

b)

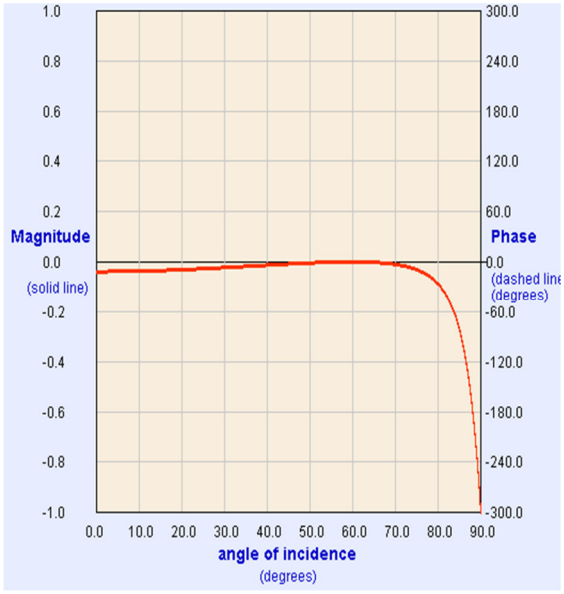

Figure 46. AVO response of Davy Jones. (a) Gas sand and shale-based seal model. (b) Brine sand and shale-based seal model.

a)

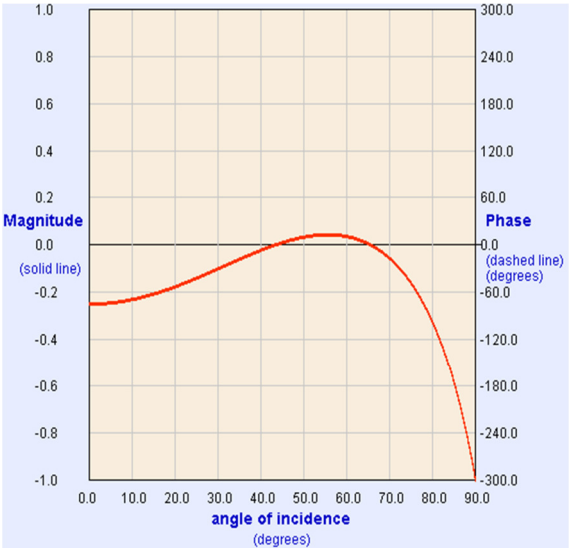

b)

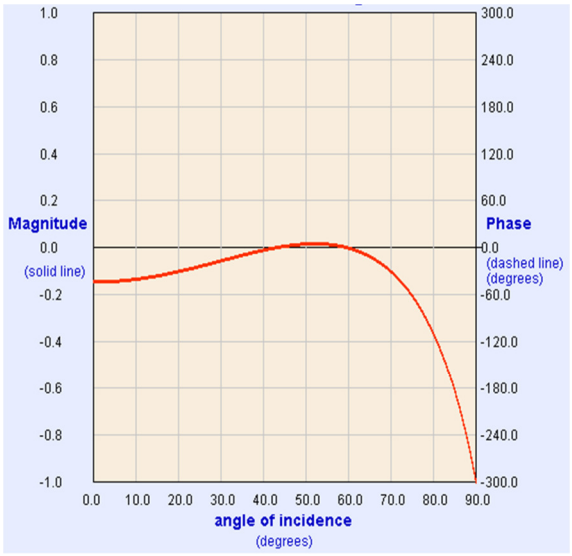

Figure 47. AVO response of N1. (a) Gas sand and shale-based seal model. (b) Brine sand and shale-based seal model.

a)

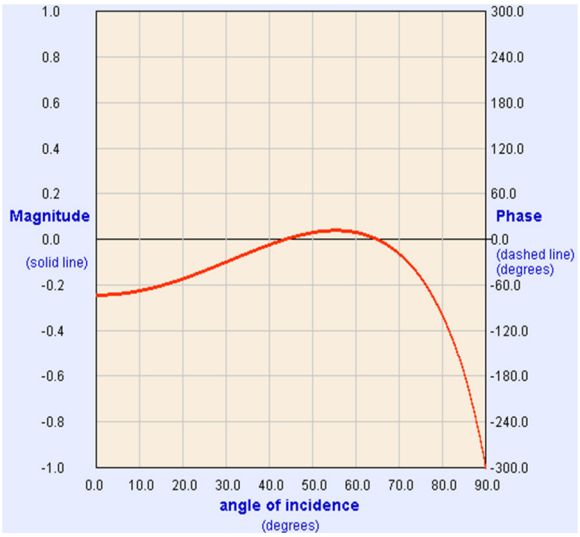

b)

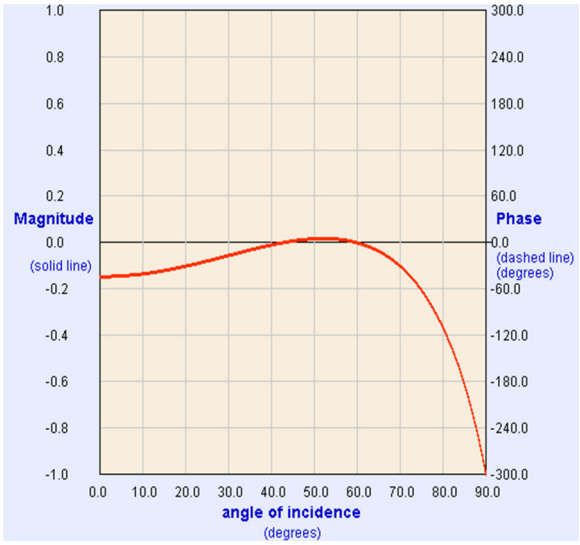

Figure 48. AVO response of N2. (a) Gas sand and shale-based seal model. (b) Brine sand and shale-based seal model.

a)

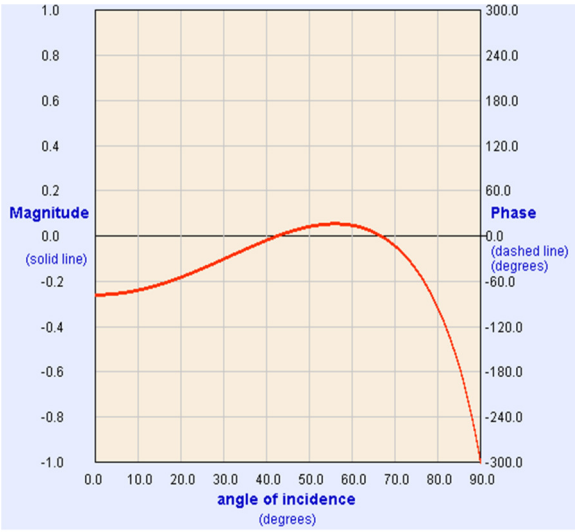

b)

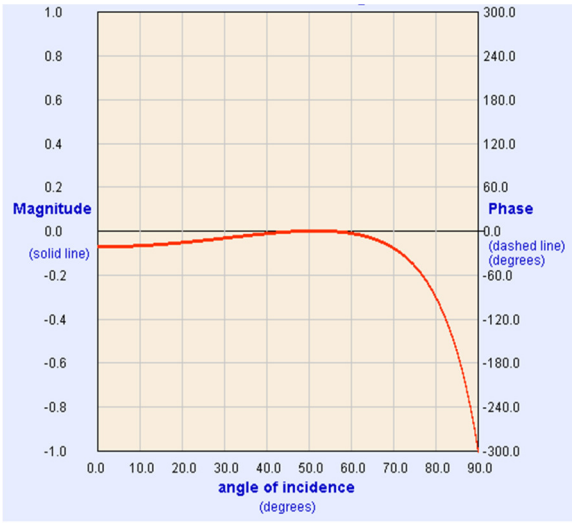

Figure 49. AVO response of N3. (a) Gas sand and shale-based seal model. (b) Brine sand and shale-based seal model.

Table 9. Reservoir parameters of N4 before and after fluid substitution.

Reservoir Parameters for Study Area N4 During Fluid Substitutions		**Reservoir Parameters for Study Area N4 After Fluid Substitutions**		
Pore Pressure (Mpa)	**186.3**	**V_b and V_g Brine water and gas velocities respectively (m/s)**	**911**	**368**
Formation Temperature (C^o)	**223**	**V_{bsat} and V_{gsat} Brine and gas saturated P wave velocities (m/s)**	**2554**	**919**
Porosity (%)	**20**	**I_{bsat} and I_{gsat} Brine and gas saturated impedances**	**5906**	**2009**
Salinity (ppm)	**50000**	**R_{gsat} /R_{bsat} Ratios of Brine and gas saturated reflection coefficients**	**1.26**	
Two Way Travel Time (s)	**6.47**	**M_{bsat} and M_{gsat}Brine and gas saturated P wave moduli (Gpa)**	**15.1**	**1.84**
K_o quartz mineral bulk Modulus (Gpa)	**38**	**M_d and M_o Dry and mineral P wave moduli (Gpa)**	**-0.57**	**97**
G_o quartz mineral shear Modulus (Gpa)	**44.3**	**K_d and G_d Dry bulk and shear moduli (Gpa)**	**-0.07**	**-0.37**
ρ_m quartz mineral density (g/cc)	**2.65**	**ρ_b and ρ_g Brine and gas densities (g/cc)**	**0.96**	**0.33**
R molar gas contant (joule)	**8.3144**	**ρ_{bsat} and ρ_{gsat} Brine and gas saturated densities (g/cc)**	**2.32**	**2.19**
G (gas specific gravity for methane)	**0.56**	**V_w water velocity (m/s)**	**904**	
Stiffness Parameter "A" for K_d	**5.40**	**K_b Brine bulk modulus (Gpa)**	**3.55**	
Stiffness Parameter "B" for G_d	**5.48**	**K_g Gas bulk modulus (Gpa)**	**0.48**	

Table 10. Reservoir parameters of N5 before and after fluid substitution.

Reservoir Parameters for Study Area N5 During Fluid Substitutions		**Reservoir Parameters for Study Area N5 After Fluid Substitutions**		
Pore Pressure (Mpa)	**210.3**	**V_b and V_g Brine water and gas velocities respectively (m/s)**	**1196**	**393**
Formation Temperature (C^o)	**231**	**V_{bsat} and V_{gsat} Brine and gas saturated P wave velocities (m/s)**	**3078**	**907**
Porosity (%)	**20**	**I_{bsat} and I_{gsat} Brine and gas saturated impedances**	**7118**	**1987**
Salinity (ppm)	**50000**	**R_{gsat} /R_{bsat} Ratios of Brine and gas saturated reflection coefficients**	**1.35**	
Two Way Travel Time (s)	**6.7**	**M_{bsat} and M_{gsat}Brine and gas saturated P wave moduli (Gpa)**	**21.91**	**1.8**
K_o quartz mineral bulk Modulus (Gpa)	**38**	**M_d and M_o Dry and mineral P wave moduli (Gpa)**	**-1.07**	**97**
G_o quartz mineral shear Modulus (Gpa)	**44.3**	**K_d and G_d Dry bulk and shear moduli (Gpa)**	**-0.45**	**-0.46**
ρ_m quartz mineral density (g/cc)	**2.65**	**ρ_b and ρ_g Brine and gas densities (g/cc)**	**0.96**	**0.34**
R molar gas contant (joule)	**8.3144**	**ρ_{bsat} and ρ_{gsat} Brine and gas saturated densities (g/cc)**	**2.32**	**2.19**
G (gas specific gravity for methane)	**0.56**	**V_w water velocity (m/s)**	**1191**	
Stiffness Parameter "A" for K_d	**5.45**	**K_b Brine bulk modulus (Gpa)**	**3.53**	
Stiffness Parameter "B" for G_d	**5.49**	**K_g Gas bulk modulus (Gpa)**	**0.57**	

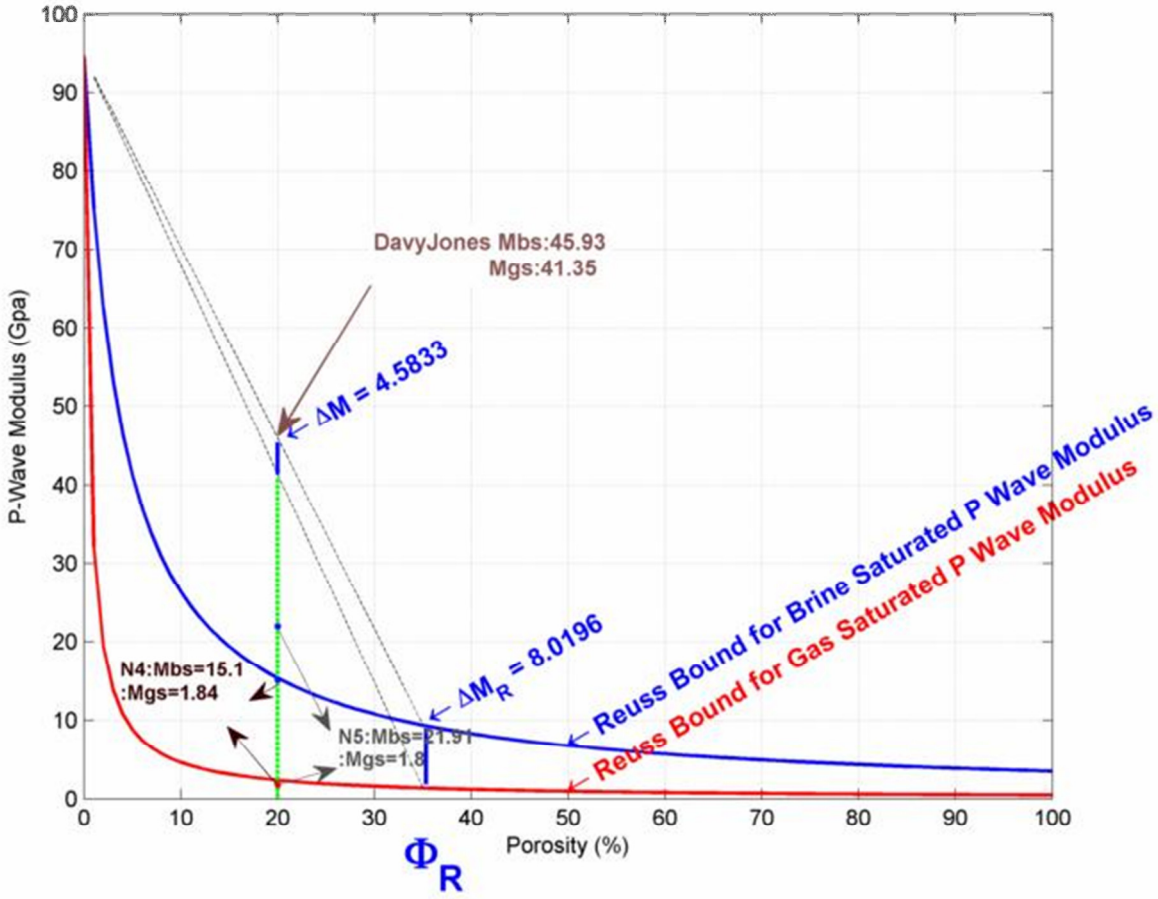

Figure 50. Brine and gas saturated P wave moduli changes of N4, and N5 relied on brine and gas saturated Reuss bounds of Davy Jones.

Chapter 4. Discussion

The combined results of fluid substitution analysis, seismic interpretation and Reuss bound examination of the study areas render it possible to draw many critical conclusions and to make some useful inferences. Mainly, it can be claimed that the areas N1, N2, and N3 were successfully characterized with their amenable amplitude bright spot responses, while study regions N4 and N5 appeared to cause unrealistic bright spot indications. There are many factors that came together during the course of this study to validate the above statement.

Initially, fluid substitution analysis of the Davy Jones reservoir provided the desired physical conditions of a successful reservoir which were utilized in the characterizations of each study area. Based on its reservoir parameters, both seismic and fluid substitution analysis were performed confidently, thereby making it possible to identify each bright spot response associated with the study areas. During these crucial processes, pore pressure, formation temperature, the original porosity of the Davy Jones reservoir and dry frame stiffness parameters were the key parameters which were responsible for the varying responses of each study area. It was assumed that the Wilcox shelf trend of South Marsh Island was preserved in the vicinity of Vermilion, and so similar Wilcox structures of the Vermilion could have porosities close to those of Davy Jones. Therefore, the original porosity of Davy Jones, which is 20% was held constant along all computations. However, real pore pressure and formation temperatures of Davy Jones were not the same for each study region. Apart from N1, all study areas demonstrated different pressure and temperature regimes compared to Davy Jones

(shown in Table 10). This is due to the fact that adjustments of reflection coefficients through both seismic and fluid substitution analysis dictated those necessary differences of formation temperature and pore pressure. Thus, adjusted pore pressure and temperature values of the targets inherently affected their individual fluid substitution responses. One immediate impact of this was felt on the brine and gas bulk moduli, as well as on the brine and gas velocities of the areas prior to fluid substitutions. Increasing pressure and temperature values resulted in expansion of both bulk moduli and fluid velocities. The areas N3 and N5 seemed to show the largest pressure and temperature values by leading the augmentation of brine and gas velocities before fluid substitution. Brine- and gas-saturated P-wave moduli and velocities exhibited similar responses for study areas N1, N2, and N3, unlike N4 and N5, after fluid substitutions.

Consequently, brine- and gas-saturated reflection coefficients were formed largely based on those affected elastic parameters and velocities. Even though, the original porosity of the Davy Jones reservoir remained unchanged during these tasks, stiffness parameters which were implemented in characterizations of dry frame properties were not the same for each study area. They were also modified during comparisons of reflection coefficients, as mentioned before. The stiffness parameters of N1, N2, and N3 slightly deviated, from 3.5 to 4.5, based upon those of Davy Jones, whereas N4 and N5 underwent more robust changes of stiffness parameters from nearly 3.5 to 5.5. Clearly, these adjusted values of stiffness parameters for N4 and N5 caused unrealistic dry frame properties by leading to a negative valued dry frame P-wave modulus, while the stiffness parameters of N1, N2, and N3 reliably represent their dry frame P-wave modulus (shown

in Table 10). Although the geology of the Vermilion targets was presumed to show characteristics similar to those of Davy Jones in South Marsh Island, they may not necessarily demonstrate identical compositional features. It can be suggested that local compositional conditions of each study area exhibit distinct consolidation and packing characteristics of pore frames. These frame properties of the rocks are largely reflected by both their porosities and stiffness parameters. Considering that the porosity of 20% was used constantly for each area, it can be claimed that the stiffness parameters could play a key role to differentiate the compositional environment of each region. In this study, the stiffness parameters of N1, N2, and N3 are nearly the same around 4.5. This might be an indication of consistent compositional characteristics in the areas. On the other hand, N4 and N5 also have roughly the same stiffness parameters, about 5.5. This consistently points out their compositional properties which make them unlikely to become adequate reservoirs.

The Reuss bound examinations correspondingly distinguished each study area with its unique P-wave moduli response which are shown in Figure 51. As stated in previous discussions of pore pressures, formation temperatures, and stiffness parameters, Reuss bound representations of the study areas also imply the suitability of N1, N2, and N3 for illustrating successful bright spot responses; they also suggest that areas N4 and N5 cause nonphysical brine- and gas-saturated P-wave moduli responses and inadequate bright spot indications. In this manner, study regions N1, N2 and N3 have brine- and gas-saturated P-wave moduli which are safely located above the brine- and gas-saturated Reuss bounds of Davy Jones, whereas the saturated P-wave moduli responses of N4 and

N5 correspond to suspension form rather than desired brine- and gas-saturated reservoirs under these Reuss bounds.

Table 11. Important reservoir parameters and related outcomes for all study areas.

Areas of Interest	N1	N2	N3	N4	N5	Davy Jones
Pore Pressure (Mpa)	186.2	179.2	235.3	186.3	210.3	182.2
Formation Temperature (C^o)	226.7	218.7	235.7	223	231	226.7
Porosity (%)	20	20	20	20	20	20
Salinity (ppm)	50000	50000	50000	50000	50000	50000
Stiffness Parameter "A" for K_d	4.49	4.48	4.49	5.4	5.45	3.39
Stiffness Parameter "B" for G_d	4.49	4.48	4.48	5.48	5.49	3.48
Brine Saturated P Wave Modulus (Gpa)	28.5	27.7	41.5	15.1	21.91	44.3
Gas Saturated P Wave Modulus (Gpa)	19.6	19.7	20.4	1.84	1.8	39
Dry Frame P Wave Modulus (Gpa)	18	18.2	18.2	-0.57	-1.07	38.3
Brine Saturated Densities (g/cc)	2.31	2.32	2.32	2.32	2.32	2.31
Gas Saturated Densities (g/cc)	2.18	2.19	2.19	2.19	2.19	2.18
P wave Velocity Ratios From Seismic Vb/Vg	1.179	1.156	1.39	2.782	3.394	-
P wave Velocity Ratios via Fluid Substitution Vb/Vg	1.172	1.152	1.384	2.78	3.391	1.03
Brine and Gas Saturated Relative Reflection Coefficient Ratios Rg/Rb	1.23	1.23	1.31	1.26	1.35	1.34

Thus, Reuss bound interpretation of the areas is also critical from many perspectives. Firstly, the individual, saturated P-wave modulus responses of N1, N2, and N3 are closely located to each other above the Reuss bounds, while N4 and N5 have saturated P-wave moduli almost identical to each other under the Reuss bounds. This implies consistent compositional characteristics of the study areas, as the stiffness parameters suggested. The regions N1, N2, and N3 show sufficiently stiffened pore frames to accommodate gas and brine fluids under their specific reservoir conditions. On the other hand, N4 and N5 demonstrate little or simply no intrinsic stiffness to bear fluid effects on their pore frames.

Secondly, Reuss bound displays of the study areas also point out that pore frames of areas N1, N2, and N3 are fairly stiffened to sustain effective pressures across their pore spaces. Thus, they allow desired saturations of the reservoir rocks, unlike areas N4 and N5, as stated previously in the pore pressures discussion (Sayers, 2010). Coherently, brine- and gas-saturated velocity ratios derived from both seismic amplitude interpretation and fluid substitution analysis of the areas illustrate that areas N1, N2, and N3 are located between1 and 1.5 in terms of their brine to gas saturated velocity ratios. These correspond well to the ratios of Davy Jones, shown in Figure 52. However, brine- to gas-saturated velocity ratios of the N4 and N5 are impractically high, at about 2.8 and 3.4 in the same figure. Thus, brine- and gas-saturated velocity ratios of the areas are in good agreement with the results of the Reuss bounds and the relevant inferences which were made through the consideration of pore pressures, formation temperatures, and stiffness parameters.

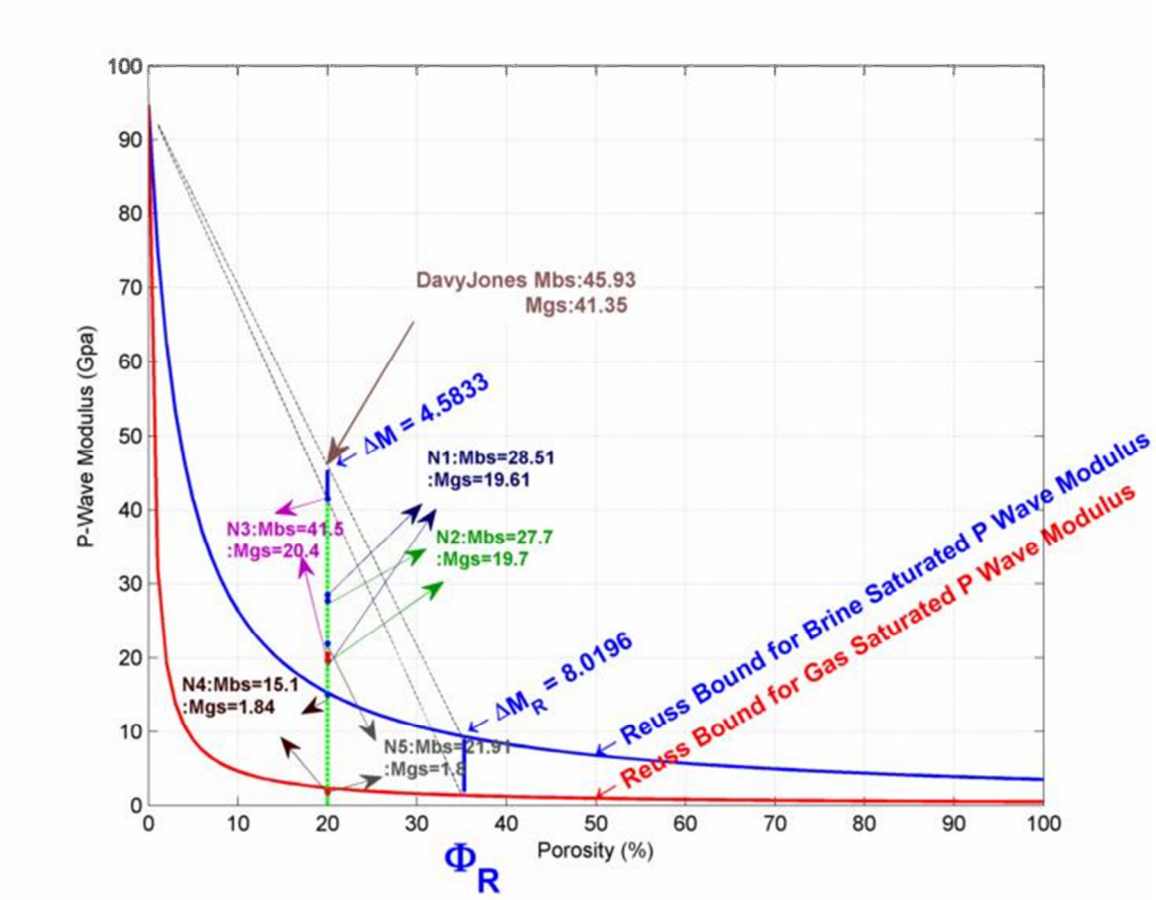

Figure 51. Brine- and gas-saturated P-wave moduli changes of all study areas based on the brine- and gas-saturated Reuss bounds of Davy Jones.

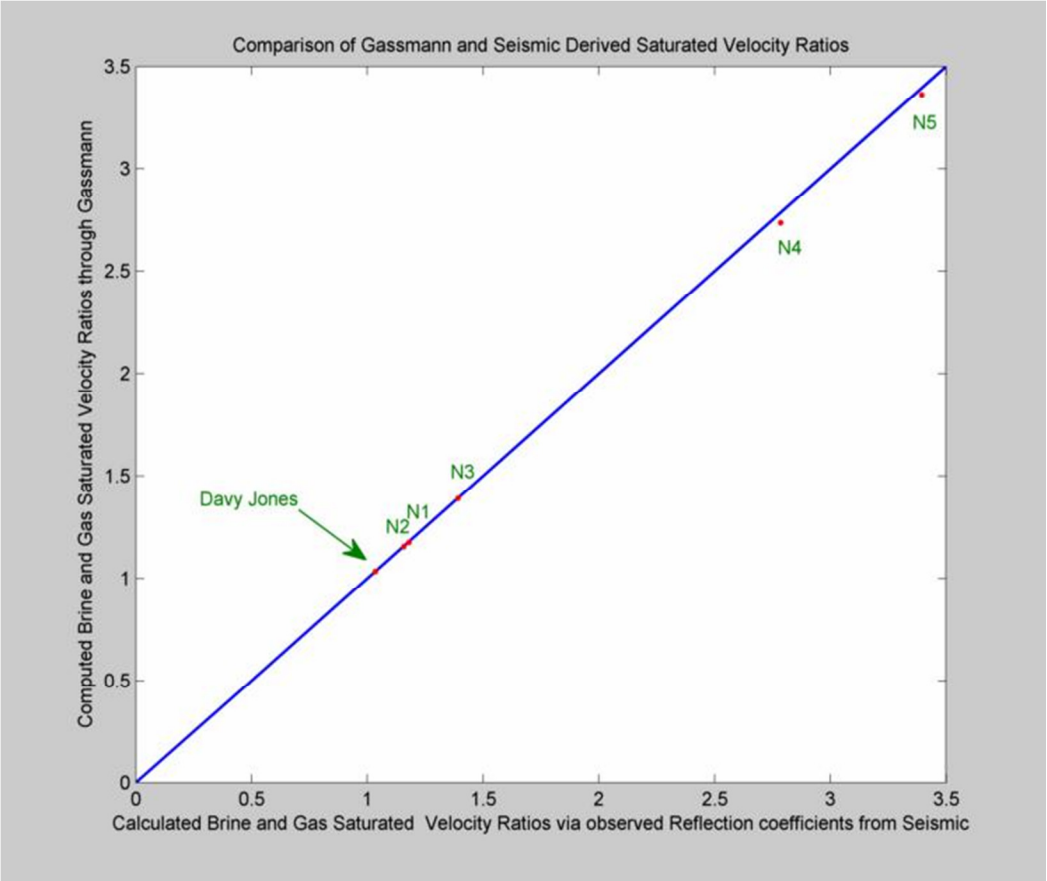

Figure 52. Comparisons of brine- and gas-saturated velocity ratios of the study areas obtained via both seismic amplitude interpretation and Gassmann fluid substitutions.

a) b)

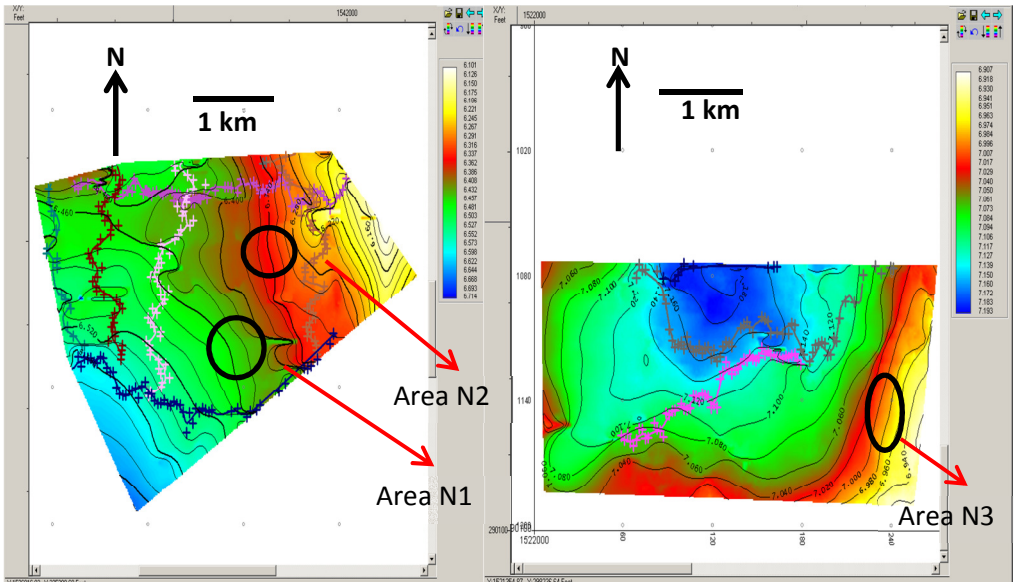

c)

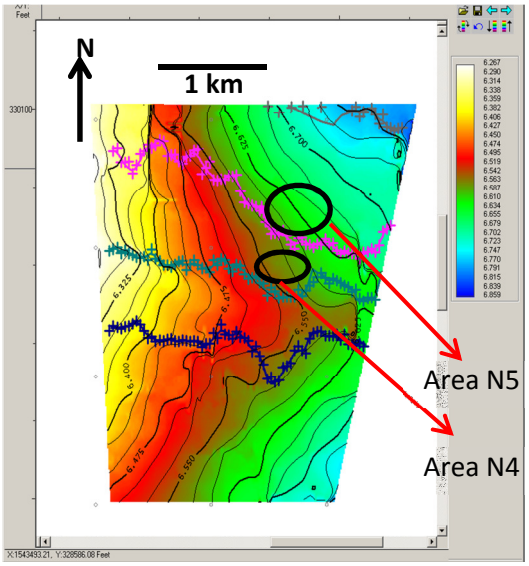

Figure 53. Fault orientations of the areas N1, N2 (a), N3 (b), N4, and N5(c).

Seismic fault interpretation results consistently support the findings of related characterizations of the areas. In this sense, fault interpretations imply that study areas N1, N2, and N3 are located sufficiently distant from their nearby faults; their reservoir frames seem to be unaffected by any destructive influences from the faults shown in Figures 53a and b, as the reservoir formations of N4 and N5 are considered to be partially or massively deformed by the closely located faults in Figure 53c. Thus, it can be claimed that possible deformations of N4 and N5 via fault disturbances caused alterations of their reservoirs by lowering the stiffness of pore frames to carry out created effective pressures along pore spaces. Therefore, they do not physically respond to any fluid effects during fluid substitutions as a result of weakened pore frames and impractically consequent dry frame P-wave moduli (Toksoz, Cheng, and Timur, 1976).

Resultant brine- and gas-saturated velocities of the areas are very close to those of fractured sandstone reservoir formations encountered in hydrocarbon explorations. Thus, their distinct brine- and gas-saturated velocities fortify feasible fault interruptions and deformations of the areas (Mavko and Mukerji, 1995). There might be some additional explanations for what is responsible for the inappropriate bright spot responses of areas N4 and N5.

One plausible explanation could be related to lower cementation rates of the reservoir frames. Disappearance of cementing materials such as from chemical activities could create more unstable and weaker pore frames, ending with unrealistic fluid substitution effects. Furthermore, shale formations have velocities in a broad range, from 2500 to 6500 m/s, depending on their frame and mineral properties as well as their

interactions with chemical activities. N4 and N5 might reflect a reservoir response of chemically altered gas shale rather than a fractured sandstone reservoir from their low velocity ranges; yet there is no clear evidence of this.

Another reservoir parameter which was implemented throughout fluid substitution analysis of the areas was brine salinity. Surprisingly, varying salinity values, from 20000 to 100000 ppm, appeared to be ineffective in creating substantial changes in brine properties and resultant brine saturated velocities and elastic parameters. Therefore, 50000 ppm of brine salinity was held constant during all computations to approximate northern Gulf of Mexico salinity values.

Chapter 5. Conclusions

By considering the results of this study, many decisive statements can be made. Primarily, it can be asserted that study regions N1, N2, and N3 consistently demonstrated suitable amplitude bright spot responses, whereas the areas N4 and N5 clearly caused inadequate bright spot anomalies based on their related characterizations. Secondly, pore pressure and formation temperature of the areas were effectively adjusted during the comparisons of the results by means of seismic amplitude interpretation and fluid substitution analysis. This led to proper estimations of pore fluid properties, brine-and-gas saturated velocities, reflection coefficients and elastic parameters. Thirdly, modified stiffness parameters of the areas based on Davy Jones played a key role in characterizations of their dry frame properties. Thus, specified dry frames of the areas

contributed largely to shape unique reservoir responses of the areas during fluid substitutions.

Resultant dry frames of the regions clearly suggest that the areas N1, N2, and N3 are sufficiently stiffened to carry out implemented pressures and fluid substitution effects throughout pore spaces, while the regions N4 and N5 impractically show little or no intrinsic stiffness to sustain any pressure and fluid saturation impacts. Similarly, Reuss bound examinations of the study areas illustrate that the brine- and gas-saturated P-wave moduli of N1, N2, and N3 are located close to each other above the Reuss bounds of Davy Jones, as saturated P-wave moduli of the N4 and N5 corresponded to responses of a suspension under the Reuss bounds.

Furthermore, fault interpretations of the areas correctly anticipated that N1, N2, and N3 are not disturbed by nearby faults, while fault interruptions of the N4 and N5 areas are apparent by implying their inadequateness to become bright spot indicators. In addition, the AVO responses of each study area are in good agreement with the results of other implemented methods. This suggests the consistency of the gas bright spot effect for areas N1, N2 and N3, while it implies the inadequateness of N4 and N5 in representing gas bright spot effect.

Lastly, the Gassmann fluid substitution method proved its effectiveness in predicting bright spot responses of deep reservoir targets with the collaborations of other implemented methods. They together safely accomplished to distinguishing appropriate bright spot responses of areas N1, N2, and N3, as well as the unrealistic bright spot anomalies of N4 and N5.

References

Batzle, M., and Z. Wang, 1992, Seismic Properties of Pore Fluids: Geophysics, **57**, no. 11, 1396-1408.

Brown, A. R., 1999, Interpretation of Three-Dimensional Seismic Data (Fourth Edition): AAPG Memoir/SEG Investigations in Geophysics, no. 9, 146.

Castagna, J.P., and H.W. Swan, 1997, Principles of AVO Crossplotting: The Leading Edge.

Castagna, J.P., H.W. Swan, and D.J. Foster, 1998, Framework for AVO Gradient and Intercept Interpretation: Geophysics, **63**, no. 3, 948-956.

Castagna, J.P., M.L. Batzle, and R.L. Eastwood, 1985, Relationships between Compressional-wave and Shear-wave Velocities in Clastic Silicate Rocks: Geophysics, **50**, no. 4, 571-581.

Diegel, F. A., D. C. Schuster, J. F. Karlo, R. C. Shoup, and P. R. Tauvers, 1995, Cenozoic Structural Evolution and Tectono-Stratigraphic Framework of the Northern Gulf Coast Continental Margin, *in* M.P.A Jackson, D.G. Roberts, and S. Snelson, eds., Salt Tectonics: a global perspective: AAPG Memoir, no. 65, 109-151.

Dutton, S. P., and R. G. Loucks, 2010, Diagenetic Controls on Evolution of Porosity and Permeability in Lower Tertiary Wilcox Sands from Shallow to Ultradeep (200-6700 m) Burial, Gulf of Mexico Basin, U.S.A., Marine and Petroleum Geology, no. 27; 69-81.

Fairfield Nodal, 2010, Prestack time migration program map: http://www.fairfieldnodal.com/Services/Data%20Licensing/PSTM/index.html, accessed July 15, 2011

Fairfield Nodal, Breakthrough in the Shallow Gulf of Mexico: Davy Jones Discovery, http://www.fairfieldnodal.com/Services/Data%20Licensing/Davy%20Jones%20Slideshow/index.html, accessed July 15, 2011

Galloway, W. E., 2000, Cenozoic Depositional History of the Gulf of Mexico Basin: AAPG Bulletin, **84**, no. 11, 1743-1774.

Galloway, W. E., 2001, Cenozoic Evolution of Sediment Accumulation in Deltaic and Shore-Zone Depositional Systems, Northern Gulf of Mexico Basin: Marine and Petroleum Geology, no. 18, 1031-1040.

Galloway, W. E., 2002, Cenozoic Deep-Water Reservoir Systems of the Northern Gulf of Mexico Basin: Gulf Coast Association of Geological Societies Transections, **52**, 301-308.

Han, D., and M. L. Batzle, 2004, Gassmann's Equation and Fluid- Saturation Effects on Seismic Velocities: Geophysics, **57**, no.11, 396-1408.

Hilterman, F.J., R.W. Verm, M. Wilson, and L. Liang, 1999, Calibration of Rock Properties for Deepwater Seismic: SEG 1999 Expanded Abstracts.

Hilterman, F.J., H. Yu, and A. Chaveste, 2011, Calibration of Effective Pressure Coefficient for Gulf of Mexico Shale from Well-log Data: SEG San Antonio 2011 Annual Meeting.

Liner, L. C., 2004, Elements of 3D Seismology Second Edition, Pennwell Corporation.

Mavko, G., and T. Mukerji, 1995, Seismic Pore Space Compressibility and Gassmann's Relation: Geophysics, **60**, no. 6, 1743-1749.
Mavko, G., C. Chan, and T. Mukerji, 1995, Fluid Substitution: Estimating Changes in Vp Without Knowing Vs: Geophysics, **60**, no. 6, 1750-1755.
Mavko, G., T. Mukerji, and J. Dvorkin, 2009, The Rock Physics Handbook Second Edition: Cambridge University Press, 339-342.
Meyer, D., L. Zarra, D. Rains, B. Meltz, and T. Hall, 2005, Emergence of the Lower Tertiary Wilcox Trend in the Deepwater Gulf of Mexico: Search and Discovery Article, #10084.
Peel, F. J., J. R. Hossack, and C. J. Travis, 1995, Genetic Structural Provinces and Salt Tectonics of the Cenozoic Offshore U.S. Gulf of Mexico: A Preliminary Analysis, *in* M.P.A. Jackson, D.G. Roberts, and S. Snelson, eds., Salt Tectonics: A Global Perspective, AAPG Memoir, no. 65, 153-175.
Radovich, B., M. Alexander, and C. Prieto, 2003, Basement Structural Analysis Key in Deep Shelf Play: The American Oil and Gas Reporter.
Radovich, B. J., Moon, J., Connors, C. D., and Bird, D., 2007, Insights into Structure and Stratigraphy of the Northern Gulf of Mexico from 2D Pre-Stack Depth Migration Imaging of Mega-Regional Onshore to Deep Water, Long-Offset Seismic Data: Gulf Coast Association of Geological Societies Transactions, **57**, 633-637.
Rowan, M. G., M. P. A. Jackson, and B. D. Trudgill, 1999, Salt Related Fault Families and Fault Welds in the Northern Gulf of Mexico: AAPG Bulletin, **83**, no. 9, 1454-1484.
Sayers, C. M., 2010, Geophysics Under Stress: Geomechanical Applications of Seismic and Borehole Acoustic Waves, Eage Distinguished Instructor Series, no. 13, 1-23.
Snyder, F., N. Biles, L.D. Boer, P.Hooyman, G. Jamieson, and C. Sayers, 2010, High Velocity Zones in Deep Mini-Basin Miocene Sediments, Eugene Island, Northern Gulf of Mexico: Search and Discovery Article, #40063.
The American Oil and Gas Reporter, 2010, Davy Jones Discovery Opening New Shelf Frontier In Ultradeep Geology Below Salt: http://www.aogr.com/index.php/magazine/cover-story/davy-jones-discovery-opening-new-shelf-frontier-in-ultradeep-geology-below/, accessed March 22, 2011
Toksoz, M. N., C. H. Cheng, and A. Timur, 1976, Velocities of Seismic Waves in Porous Rocks: Geophysics, **41**, no. 4, 621-645.
Wang, Z., 2001, Fundamentals of Seismic Rock Physics, Geophysics: **66**, no. 2, 398-412.